

AD\_\_\_\_\_

Award Number: DAMD17-02-1-0307

TITLE: Electroacoustic Tissue Imaging

PRINCIPAL INVESTIGATOR: Gerald J. Diebold, Ph.D.

CONTRACTING ORGANIZATION: Brown University  
Providence, RI 02912

REPORT DATE: March 2007

TYPE OF REPORT: Final Addendum

PREPARED FOR: U.S. Army Medical Research and Materiel Command  
Fort Detrick, Maryland 21702-5012

DISTRIBUTION STATEMENT: Approved for Public Release;  
Distribution Unlimited

The views, opinions and/or findings contained in this report are those of the author(s) and should not be construed as an official Department of the Army position, policy or decision unless so designated by other documentation.

REPORT DOCUMENTATION PAGE				Form Approved OMB No. 0704-0188	
Public reporting burden for this collection of information is estimated to average 1 hour per response, including the time for reviewing instructions, searching existing data sources, gathering and maintaining the data needed, and completing and reviewing this collection of information. Send comments regarding this burden estimate or any other aspect of this collection of information, including suggestions for reducing this burden to Department of Defense, Washington Headquarters Services, Directorate for Information Operations and Reports (0704-0188), 1215 Jefferson Davis Highway, Suite 1204, Arlington, VA 22202-4302. Respondents should be aware that notwithstanding any other provision of law, no person shall be subject to any penalty for failing to comply with a collection of information if it does not display a currently valid OMB control number. <b>PLEASE DO NOT RETURN YOUR FORM TO THE ABOVE ADDRESS.</b>					
1. REPORT DATE (DD-MM-YYYY) 01-03-2007		2. REPORT TYPE Final Addendum		3. DATES COVERED (From - To) 1 Apr 2006 – 28 Feb 2007	
4. TITLE AND SUBTITLE  Electroacoustic Tissue Imaging				5a. CONTRACT NUMBER	
				5b. GRANT NUMBER DAMD17-02-1-0307	
				5c. PROGRAM ELEMENT NUMBER	
6. AUTHOR(S)  Gerald J. Diebold, Ph.D.  E-Mail: <a href="mailto:Gerald_Diebold@Brown.edu">Gerald_Diebold@Brown.edu</a>				5d. PROJECT NUMBER	
				5e. TASK NUMBER	
				5f. WORK UNIT NUMBER	
7. PERFORMING ORGANIZATION NAME(S) AND ADDRESS(ES)  Brown University Providence, RI 02912				8. PERFORMING ORGANIZATION REPORT NUMBER	
9. SPONSORING / MONITORING AGENCY NAME(S) AND ADDRESS(ES) U.S. Army Medical Research and Materiel Command Fort Detrick, Maryland 21702-5012				10. SPONSOR/MONITOR'S ACRONYM(S)	
				11. SPONSOR/MONITOR'S REPORT NUMBER(S)	
12. DISTRIBUTION / AVAILABILITY STATEMENT Approved for Public Release; Distribution Unlimited					
13. SUPPLEMENTARY NOTES					
14. ABSTRACT  Research has been directed towards detection of tumors using a new imaging modality based on an electrokinetic effect known as the ultrasonic vibration potential. Major accomplishments include completion of a theory for image formation for a colloidal object, such as a pool of blood, development of instrumentation for recording images, and testing of the theory with phantoms with differing geometries. Additionally, phase contrast x-ray imaging for tumor detection has been initiated. A high resolution imaging apparatus has been assembled and tested for imaging soft tissue. Methods for calculating phase contrast images from symmetrical bodies has been developed. The phase contrast method has shown unprecedented detail for imaging microvasculature.					
15. SUBJECT TERMS Vibration potential, ultrasound, phase contrast, imaging					
16. SECURITY CLASSIFICATION OF:			17. LIMITATION OF ABSTRACT	18. NUMBER OF PAGES	19a. NAME OF RESPONSIBLE PERSON
a. REPORT	b. ABSTRACT	c. THIS PAGE			USAMRMC
U	U	U	UU	97	19b. TELEPHONE NUMBER (include area code)

## Table of Contents

Introduction .....	4
Body .....	4
Key Research Accomplishments.....	4
Reportable Outcomes .....	7
Conclusions .....	8
References .....	9
Appendices .....	9

## INTRODUCTION

The ultrasonic vibration potential refers to the generation of voltages when a colloidal or ionic solution is irradiated with ultrasound<sup>1</sup>. A colloid can be broadly described as a suspension of charged particles in solution. A countercharge resides around each particle in a spherical distribution in the surrounding medium in order that the solution have overall charge neutrality. Consider the case when the particles have a higher density than the surrounding fluid. When ultrasound passes through the solution, the acceleration in the ultrasonic wave gives rise to oscillatory motion of both the fluid and the particles. However, owing to the higher inertia of the particles, their motion is smaller in amplitude than that of the fluid resulting in the flow of fluid across the particle surfaces. This flow results in a distortion of the normally spherical charge distribution and causes a dipole to be generated at the site of each particle. When added over a macroscopic distance the ensemble of dipoles results in a time varying polarization. The polarization can be measured with two electrodes in the solution, or by measuring a current in a pair of electrodes external to the colloid. We have shown that blood is colloidal and produces large contrast relative to soft tissue. Since blood is known as a marker for invasive tumors, the method has application to detection of tumors.

We have also investigated phase contrast x-ray imaging<sup>2</sup> for tumor detection. Phase contrast imaging is based on detection of differences in the index of refraction of bodies which cause deviations in the paths of x-radiation resulting in a contrast in addition to conventional absorption contrast. The apparatus employed here consists of a microfocus x-ray tube, a high resolution CCD camera, and a phosphor screen. The method of recording phase changes is referred to as the “in line” method<sup>2</sup>. The high sensitivity of this method for detecting small density changes in soft tissue has been investigated for use in tumor detection.

## BODY

Following development of a theory of imaging, the forward problem has been investigated experimentally to verify predicted current versus frequency curves. Work on thin layers, finite thickness layers, layers inclined at an angle, multiple layers, multiple layers with different concentrations, spheres, and cylinders has been carried out. Experimental apparatus has been assembled and its operation characterized. Secondly, the theory of phase contrast imaging has been investigated. A Fresnel integral method for calculation of images for bodies with symmetrical transmission functions has been investigated and compared with experiment. Experiments with *ex vivo* murine tissue have been carried out.

## KEY RESEARCH ACCOMPLISHMENTS

The major theoretical result from the research carried out here has been development of a theory for the current generation for an object with an arbitrary distribution in space that describes vibration potential imaging. The current in the electrodes can be written as integral of the pressure gradient over the distribution of colloidal or ionic species in the body as

$$I = \frac{i\omega}{h} \int_v \alpha(\mathbf{x}, \omega) \frac{\partial}{\partial z} p(\mathbf{x}) dx dy dz. \quad (1.1)$$

where  $\alpha$  is the distribution of the colloid in space,  $\omega$  is the frequency of the ultrasound,  $h$  is the distance between the electrodes, and  $p$  is the pressure. This expression can also be written in terms of the pressure directly as

$$I = -\frac{i\omega}{h} \int_v [\nabla \alpha(\mathbf{x}, \omega)]_z p(\mathbf{x}) dx dy dz. \quad (1.2)$$

The second of these equations shows that there must be a gradient of the colloidal object in space in order for a current to be generated. The method thus can be said to be a detector of colloidal gradients. Equations 1.1 and 1.2 form the basis for vibration potential imaging permitting the current to be determined from a knowledge of the ultrasonic pressure and the distribution of colloid in space.

An experimental imaging apparatus has been assembled consisting of a pulse generator, a power amplifier, a cell for phantoms, electronic amplifiers and gating circuits, and signal processing and display electronics. Much experimentation has been carried out to optimize the detection electronics in order to provide data in as short a time as possible. Most of the experiments have been carried out in the frequency domain where the current is measured as a function of the frequency of the ultrasonic wave. This data can be fitted to or compared with functions computed from the theory.

Experiments have been reported for a number of bodies with different geometries. One paper is devoted solely to comparison of the theory to experiments with objects having symmetry in one dimension. These objects include a delta function layer, a finite thickness layer, two layers placed at different distances from the transducer, and two layers at different distances from the transducer with different concentrations.

Experiments have been conducted with cylinders with their symmetry axis aligned parallel and perpendicular to the direction of propagation of the ultrasound, and spheres of differing diameters. Preliminary experiments have been carried out with spheres using focused transducers so that the image formation is analogous to that used in conventional ultrasonic imaging.

The question of the mechanism of current generation has been investigated. There is the question of whether the current comes as a result of conduction of ionic species, or solely as a result of the production of a time varying polarization between the two electrodes. The theory gives results for two mechanisms, but does not indicate which mechanism is dominant. Our research indicates that the time varying polarization is responsible for producing the signals under the conditions in the laboratory.

Experiments have been carried out to determine the frequency dependence of the vibration potential in several colloidal suspensions. The dependence of the signal amplitude on frequency is important for selecting the optimum frequency for image formation. Identical principles govern conventional ultrasonic imaging and vibration potential imaging, in particular, there is always a tradeoff between resolution and depth penetration that gives restrictions on how high the broadcast frequency can be. There is an inherent linear frequency dependence seen in Eq. 1.1 that suggests large signals at high frequencies, however, viscous effects in the solution tend to offset this dependence giving an overall decrease in amplitude with frequency over the

frequency range explored in several experiments carried out here. A knowledge of the frequency dependence of the colloidal object is important in solving the “inverse problem”, which refers to a mathematical inversion for converting vibration potential signals for an object with arbitrary geometry into an image.

A phase contrast imaging apparatus has been constructed that includes a microfocus x-ray source with appropriate shielding, a high resolution phosphor and CCD camera, and a computer.

We have carried out preliminary experiments to show that acoustic radiation pressure can be used as a kind of “contrast agent”. The procedure is to take a phase contrast image, and then to apply radiation pressure from an acoustic transducer to move objects within the body having different acoustic impedances from the surrounding tissue, at which point a second x-ray image is taken. The images are subtracted in a computer to give an image that has highlighted phase contrast with diminution of the features from absorption contrast.

The theory of phase contrast imaging has been investigated using a Fresnel integral approach. We have succeeded in predicting phase contrast features from bodies that have symmetry in one and two dimensions for the case of a radiation source with nonvanishing

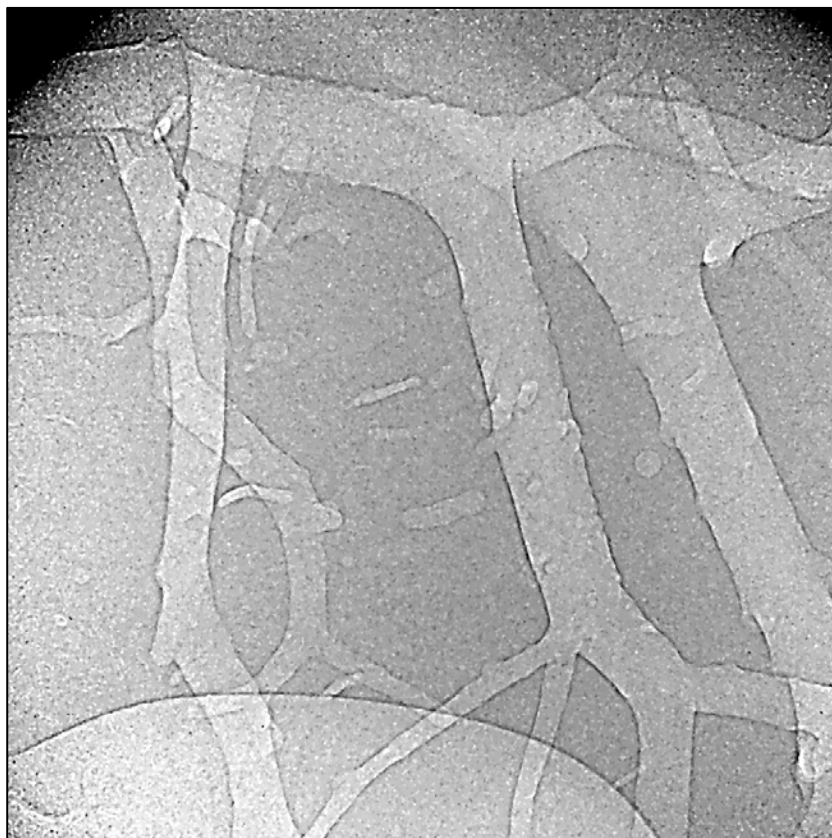


Figure 1 X-ray phase contrast image of the vasculature of a murine liver. The smallest features are on the order of 20 micrometers. No contrast agent was used. The phase contrast features are seen as bright and dark outlines of regions of differing tissue density.

dimensions. From these calculations we have shown that images from objects whose transmission functions are separable in Cartesian coordinates can be calculated. A new, rather subtle, feature of phase contrast image was predicted and found in experiments. In a separate calculation we have determined a formal mathematical method for calculation of phase contrast

images for objects with transmission functions with cylindrical symmetry for an x-ray source with finite dimensions. The method correctly predicts images from low index of refraction decrements, low absorption objects; and high index of refraction decrement, highly absorbing bodies. Experiments confirmed details of the calculations.

We have explored experimentally and theoretically the idea of using gold microparticles for use as tagging agents for x-ray imaging. The use of tagged nanoparticles has seen increasing application in biomedical applications where the idea is to tag a nanoparticle with a site or cell specific agent such as an antibody, and to use the particle as a means of detection, or, in some cases, as part of an agent that can kill unwanted cells such as tumor cells. In the investigation we have carried out, gold particles of varying sizes were imaged with the phase contrast apparatus to determine detection limits for a given x-ray source size. The theory for cylindrically symmetric particles described above was used and gave corroboration of the experimental results.

Experimental results have been obtained for imaging soft tissue. Work has focused on tissue samples available from the RI Liver Research Institute where we have collaborated with Prof. J. Wands and Dr. Philip Wintermeyer. We have demonstrated the utility of phase contrast imaging for visualizing the vasculature of livers with what appears to be unprecedented detail. We have shown that the method can detect murine skin tumors and that it has promise for detection of extremely small lesions. An example of the resolution we obtain is shown in Figure 1. .

## REPORTABLE OUTCOMES

“Vibration Potential Imaging: Theory and Preliminary Results”, with A. C. Beveridge, S. Wang, and V. Gusev, *Proc SPIE* 2004; 5320: 95-100

“Vibration Potential Imaging” with V. Gusev, A. C. Beveridge, and S. Wang, *Proc. NIST Conf. on Thermophysical Properties*, Boulder, 2004

“Imaging based on the Ultrasonic Vibration Potential” with A. C. Beveridge and S. Wang, *Appl. Phys. Lett.* **85**, 5466 (2004)

“Acoustic Radiation Pressure: a “Phase Contrast” Agent for X-ray Phase Contrast Imaging, with C. Bailat, T. Hamilton, C. Rose-Petruck *Appl. Phys. Lett.* **85** 4517 (2004)

“Acoustically Modulated X-Ray Phase Contrast Imaging” with T. Hamilton, and C. Bailat, C. Rose-Petruck, *Phys. Med. Bio.* **49**, 4985 (2004)

“Imaging with the Ultrasonic Vibration Potential: A Theory for Current Generation” with V. E. Gusev *Ultrasound in Med. and Biol.* **31**, 273 (2005)

“The Theory of Ultrasonic Vibration Potential Imaging” A. C. Beveridge, S. Wang, and V. E. Gusev, *Journal de Physique IV*, France **125**, 69 (2005)

“Acoustically Modulated X-Ray Phase Contrast and Vibration Potential Imaging” with A. C. Beveridge, C. J. Bailat, T. J. Hamilton, S. Wang, C. Rose-Petruck, and V. E. Gusev *Proceedings of the SPIE* **5697**, 90-98 (2005) Selected as the best conference paper

“Ultrasonically Modulated X-ray Phase Contrast and Vibration Potential Imaging”, with Theron J. Hamilton, Guohua Cao, Shougang Wang, Cuong K. Nguyen, Shengqiong Li, Stephan Gehring, Jack Wands, and Christoph Rose-Petruck, *Prog. in Biomed Opt. and Imag.* **7**, 608601 (2006)

“Ultrasonically Modulated X-ray Phase Contrast Imaging”, with Theron J. Hamilton, Guohua Cao, Shougang Wang, Cuong K. Nguyen, Shengqiong Li, Stephan Gehring, Jack Wands, and Cristoph Rose-Petruck, *Proc. Proc. 2006 IEEE Symp. on Biomedical Imaging: Macro to Nano* **10818**, 1108-1111 (2006)

“X-ray Phase Contrast Imaging: Transmission Functions Separable in Cartesian Coordinates”, with G. Cao, T. Hamilton, and C. Rose-Petruck *J. Opt. Soc. Am. A.*, **24**, 1201-1208 (2007)

“Frequency Domain Vibration Potential Imaging: Objects with Symmetry in One Dimension”, A. Beveridge, S. Li, and G. J. Diebold and C. Nguyen, *Appl. Phys. Lett.* **89**, 243902 (2006)

“Ultrasonic Vibration Potential Imaging: Theory and Experiments” S. Wang, C. Nguyen, and G. J. Diebold, *Progress in Biomedical Optics and Imaging, Photons Plus Ultrasound: Imaging and Sensing 2007*, **8** 64370N, (2007)

“Photothermal Modification of X-ray Phase Contrast Images” C. Laperle, G. Cao, T. J. Hamilton C. Rose-Petruck, and G. J. Diebold, *Progress in Biomedical Optics and Imaging, Photons Plus Ultrasound: Imaging and Sensing 2007*, **8** 64371N, (2007)

“X-ray Phase Contrast Imaging: transmission functions Separable in cylindrical Coordinates” Guohua Cao, Theron Hamilton, Christopher M. Laperle, Christoph Rose-Petruck, and Gerald J. Diebold, (Submitted to *J. Opt. Soc. Am.* )

## CONCLUSIONS

Progress has been made in developing a new imaging modality based on the ultrasonic vibration potential. A theory has been formulated and tested using phantoms in a number of geometries. Significant development of the apparatus has been achieved along with selection of preferred methods of signal acquisition. The theory and experiment continue to give excellent agreement.

Research with phase contrast imaging has shown an additive contrast effect with the light and dark outlines provided by phase contrast to add together with absorption contrast to delineate density changes in soft tissue. The methods developed here for calculating phase contrast images for symmetrical bodies provides a means of determining, without experimentation, x-ray images providing a sound predictive basis for finding the capabilities of the method. Experimental results have shown that small skin tumors can be detected, and that phase contrast imaging has remarkable contrast and resolution for recording extremely fine details of vasculature.



## REFERENCES

1. P. Debye, "A Method for the Determination of the Mass of Electrolytic Ions", J. Chem. Phys. 1, 13 (1933)
2. S. W. Wilkins, T. E. Gureyev, D. Gao, A. Pogany, and A. W. Stevenson, Nature 28, 384 (1996)

## APPENDIX

Published papers are attached as appendices.

# Acoustically modulated x-ray phase contrast imaging

**Theron J Hamilton, Claude J Bailat, Christoph Rose-Petruck  
and Gerald J Diebold**

Department of Chemistry, Box H, Brown University, Providence, RI 02912, USA

Received 2 June 2004, in final form 14 September 2004

Published 15 October 2004

Online at [stacks.iop.org/PMB/49/4985](http://stacks.iop.org/PMB/49/4985)

doi:10.1088/0031-9155/49/21/010

## Abstract

We report the use of ultrasonic radiation pressure with phase contrast x-ray imaging to give an image proportional to the space derivative of a conventional phase contrast image in the direction of propagation of an ultrasonic beam. Intense ultrasound is used to exert forces on objects within a body giving displacements of the order of tens to hundreds of microns. Subtraction of images made with and without the ultrasound field gives an image that removes low spatial frequency features and highlights high frequency features. The method acts as an acoustic ‘contrast agent’ for phase contrast x-ray imaging, which in soft tissue acts to highlight small density changes.

## 1. Introduction

When an x-ray beam traverses a body the spatial intensity profile of the beam is modified by the effects of absorption, scattering and phase changes, all of which depend essentially on the density of electrons. The first two of these effects form the basis of conventional radiography where a shadow is produced in the image wherever an object is of higher density than its surroundings. A second contrast mechanism, known as phase contrast, follows directly from the Huygens–Fresnel plane-wave theory of image formation, which responds to changes in index of refraction. The effect of phase contrast is subtle and is seen only when a spatially coherent source of x-rays is employed. The Fresnel–Kirchhoff integral (Born and Wolf 1980, Cowley 1984) for one dimension in the image plane  $x$ , gives the field amplitude  $f(x)$  of the x-ray beam at a distance  $z$  from the object as

$$f(x, z) = \left(\frac{i}{\lambda z}\right)^{1/2} \exp(-ikz) \int q(X) \exp\left(\frac{-ik(x - X)^2}{2z}\right) dX \quad (1)$$

where  $\lambda$  is the wavelength of the radiation,  $k$  is the wave number of the radiation and  $q(X)$  describes the transmission of the object. The transmission function,  $q(x)$ , for an object gives the effect of the object on both the phase and the amplitude of the incoming wave

and determines the intensity pattern in the image. For a thin object with a small integrated absorption,  $q(x)$  can be written as

$$q(x) = \exp(i\phi(x) - \mu(x)) \quad (2)$$

where  $\phi$  and  $\mu$  describe the change in phase and amplitude of the incoming wave, respectively, in passing through the object. The intensity of the image  $I(x) = |f(x)|^2$  for a weak phase object can be shown to be

$$I(x) = 1 - \frac{\lambda z}{2\pi} \phi''(x). \quad (3)$$

Similarly, for a weak absorber, the intensity at the image plane is given by

$$I(x) = 1 - 2\mu(x). \quad (4)$$

In a typical phase contrast image of an object embedded in a lower density medium, the usual shadowgraph from absorption is present according to equation (4), but at the edges of the object interference fringes are observed. According to equation (3), which is valid for low spatial frequencies, the intensity in the image varies as the second derivative of the phase variation in the object, which tends to be greatest for smooth objects at the interface between the object and the surrounding medium.

Several techniques have been used to record phase variations. In electron microscopy, for example, phase contrast is obtained by defocusing the electron beam and is imaged on a scintillation screen. X-ray sources with high spatial coherence, such as synchrotrons (Snigirev *et al* 1995, Fulvia Arfelli *et al* 2000, Momose 1995), microfocus x-ray tubes (Pogany *et al* 1997, Wilkins *et al* 1996) or laser plasma x-ray sources (Krol *et al* 1997a, 1997b) are commonly used for phase contrast imaging.

A detailed analysis of the relative contrast produced in an image for a fixed difference in density shows that the phase contrast is more sensitive than the absorption for detection of density differences throughout most of the spectral region commonly used for diagnostic x-ray imaging (Beckmann *et al* 1997). For instance, the thickness of water needed to produce a 1% phase contrast at 36 keV photon energy is 2500 times smaller than that required to produce the same absorption contrast (Beckmann *et al* 1997). As a consequence, x-radiation with a high photon energy, which is only weakly absorbed, can be used in phase contrast imaging to obtain the same sensitivity to density change as much more strongly absorbed, low energy x-radiation used in absorption imaging, the obvious advantage of the former being a far lower dose of absorbed radiation in the irradiated material. The size of the smallest phase object (i.e. an object where  $\mu = 0$ ) that can be detected by phase contrast can be estimated for an object, with index of refraction  $\delta_{\text{object}}$ , embedded in a surrounding medium, with index of refraction  $\delta_{\text{medium}}$ , from the relation

$$\Phi_{1\%} = \frac{2\pi t_{1\%}}{\lambda} (\delta_{\text{object}} - \delta_{\text{medium}}) \quad (5)$$

where  $t_{1\%}$  is the thickness of the object required to produce an intensity change of 1%, corresponding to a phase change of 0.14 rad. Consider application of equation (5) to tumour detection in soft tissue. Several studies (Johns and Yaffe 1987, Duck 1990) have determined that mass density differences between malignant, for instance infiltrating carcinomas, and healthy breast tissue are of the order of 10% (Duck 1990, Johns and Yaffe 1987). Since  $\delta$  is approximately  $10^{-6}$  for soft tissue, the quantity  $\delta_{\text{object}} - \delta_{\text{medium}}$  is of the order of  $10^{-7}$ . At an x-ray energy of 40 keV, corresponding to a wavelength of 31 pm, equation (5) gives  $t_{1\%}$  as 7  $\mu\text{m}$ , which implies that, ignoring specific morphological features, malignant tissue with a thickness of about 10  $\mu\text{m}$  can be distinguished from benign tissue assuming a signal-to-noise

ratio of at least 100. For the results discussed in this paper, the signal-to-noise ratio is 15, which is sufficient to distinguish object with a thickness of at least  $45 \mu\text{m}$ .

Here we report experiments where pulsed ultrasound is used to create displacements of objects within water and soft tissue. The displacement of objects with densities different from that of the surrounding body is used to modify a phase contrast x-ray giving an image with an enhanced phase contrast component. Section 2 gives calculations of the radiation pressure on spheres useful for predicting displacements of spherical objects by ultrasound. Section 3 describes the x-ray apparatus and experiments where displacements of the order of microns were produced by acoustic radiation pressure (Westervelt 1951, Chu and Apfel 1982, Beyer 1978) and measured phase contrast radiographically. Section 4 describes the x-ray acoustic method of image formation and gives examples of its use. The discussion section comments on some of the features of the method and discusses applications.

## 2. Acoustic radiation pressure

Acoustic radiation forces arise from two processes, either reflection of sound by an object as a result of an acoustic impedance change (i.e., a variation in either density or sound speed) or by absorption of sound by the object. A number of studies (Muthupillai *et al* 1995, Gao *et al* 1996, Fatemi and Greenleaf 1998, Nightingale *et al* 1999, Sarvazyan 1998, McAleavey 2003) have shown that the soft tissue can be manipulated by ultrasound pressure. Typically, a mechanical actuator or a beam of ultrasound moves an object whose position is monitored in time with conventional pulse-echo ultrasonic imaging. It has been shown that variations in Young's modulus, which, in part, determines sound speed, permit acoustic differentiation of tissue. It is known, for instance, that breast tumours have a significantly different Young's modulus from surrounding tissue, and that tumours move as rigid bodies in response to acoustic radiation pressure (Gao *et al* 1996, Nightingale *et al* 1999, 2002, Sarvazyan 1998, McAleavey 2003). It should also be noted that, at least in a mammographic application, the collective motion associated with respiration and blood pressure is minimized by immobilizing the breast.

For the purposes of the present study, where reflection of the acoustic wave is considered, it can be said that for a fixed acoustic impedance change, the force exerted by an ultrasonic wave is proportional to the time average of the energy density of the wave and the area of the object presented to the sound field. An expression for the acoustic radiation force on an arbitrary object has been given by Westervelt (1951) and evaluated for spheres small compared with the wavelength of the radiation. For spheres of any diameter, King (1934) has given an expression that agrees with the limiting expression given by Westervelt. According to King, the average acoustic radiation force exerted on a sphere of radius  $a$  is given by:

$$\bar{F}_{\text{ac}} = \frac{2\pi p^2}{(ka)^2 k^2 c^2 \rho} A(ka) \quad (6)$$

where  $\rho$  and  $c$  are the density and the speed of sound of the medium, respectively,  $p$  is the acoustic pressure,  $k$  is the wave number of the radiation, and  $A(ka)$  is given by

$$A(ka) = \frac{1}{H_0 H_1} + \frac{2}{H_1 H_2} \left\{ \frac{[(ka)^2 - 3(1 - \frac{\rho}{\rho_s})]^2}{(ka)^8} \right\} + \sum_{n=2}^{\infty} \left( \frac{(n+1)}{H_n H_{n+1}} \frac{((ka)^2 - n(n+1))^2}{(ka)^{4(n+1)}} \right) \quad (7)$$

where the functions  $H_n$  for small  $ka$  are given by

$n = 0$ :

$$H_0 = \frac{(1 + (ka)^2)}{(ka)^2}$$

$n = 1$ :

$$H_1 = \frac{4}{(ka)^6} \left( \left(1 + \frac{\rho}{2\rho_s}\right)^2 + \frac{(ka)^2}{2} \left(1 + \frac{\rho}{2\rho_s}\right)^2 \frac{\rho}{\rho_s} + \frac{(ka)^4}{4} \right)$$

$n = 2$ :

$$H_2 = \frac{81}{(ka)^{10}} \left( 1 + \frac{(ka)^2}{10} - \frac{2(ka)^2}{81} + \frac{(ka)^6}{81} \right)$$

$n > 2$ :

$$H_n = \frac{(n+1)^2 \left( \prod_{i=1}^n (2n-1) \right)^2}{(ka)^{4n+2}} \left( 1 + \frac{n-1}{(n+1)(2n-1)} (ka)^2 + \dots \right)$$

where  $\rho$  is the density of the fluid and  $\rho_s$  is the density of the sphere. For  $ka > 2$ , the functions  $H_n$  are given by

$n = 0$ :

$$H_0 = \frac{(1 + (ka)^2)}{(ka)^2}$$

$n = 1$ :

$$H_1 = \frac{\pi}{2(ka)^3} \left( \left(1 - \frac{\rho}{\rho_s}\right)^2 \left( J_{\frac{3}{2}}^2 + J_{-\frac{3}{2}}^2 \right) + 2ka \left(1 - \frac{\rho}{\rho_s}\right) \left( J_{-\frac{3}{2}} J_{-\frac{5}{2}} + J_{\frac{3}{2}} J_{\frac{5}{2}} \right) + (ka)^2 \left( J_{\frac{5}{2}}^2 + J_{-\frac{5}{2}}^2 \right) \right)$$

$n > 1$ :

$$H_n = \frac{\pi}{2(ka)^{2n+1}} \left( n^2 \left( J_{n+\frac{1}{2}}^2 + J_{-n-\frac{1}{2}}^2 \right) + 2ka \left( J_{-n-\frac{1}{2}} J_{-n-\frac{3}{2}} + J_{n+\frac{1}{2}} J_{n+\frac{3}{2}} \right) + (ka)^2 \left( J_{n+\frac{3}{2}}^2 + J_{-n-\frac{3}{2}}^2 \right) \right)$$

where  $J_n$  is a Bessel function of order  $n$ , and where the argument of each of the Bessel functions is  $ka$ .

Figure 1 is a plot of force versus  $ka$  from equation (7), with the inset showing a portion of the curve for small  $ka$ . The parameters used in equation (7) were for a Teflon bead with  $a = 1.5$  mm,  $\rho/\rho_s = 2$ ; and for water with  $c = 1500$  m s<sup>-1</sup> and  $\rho = 10^3$  kg m<sup>-3</sup>. The curves in figure 1 show, unlike optical radiation forces, a steady increase in the force with increasing  $ka$ ; the acoustic radiation pressure, of course, has a much weaker dependence on  $ka$ .

### 3. Radiation force experiments

Experiments were carried out to determine the deflection of a Teflon bead in water using an x-ray imaging apparatus to determine the deflection of the bead as a function of acoustic pressure. The x-rays, generated by a microfocus x-ray tube (Oxford Ultrabright Microfocus UB-M1), were directed onto a sample cell consisting of a 3 cm diameter PVC tube which had portions machined out and replaced with Mylar foil to reduce x-ray intensity losses. The x-ray beam, as shown in figure 2, propagated through a He filled tube to a Gd<sub>2</sub>O<sub>2</sub>S(Tb) fibre optic scintillation plate (Hamamatsu, Inc. Model J6676) the fluorescence from which was imaged onto a liquid nitrogen cooled CCD camera (Roper Scientific Model 7382-0001). The intensity

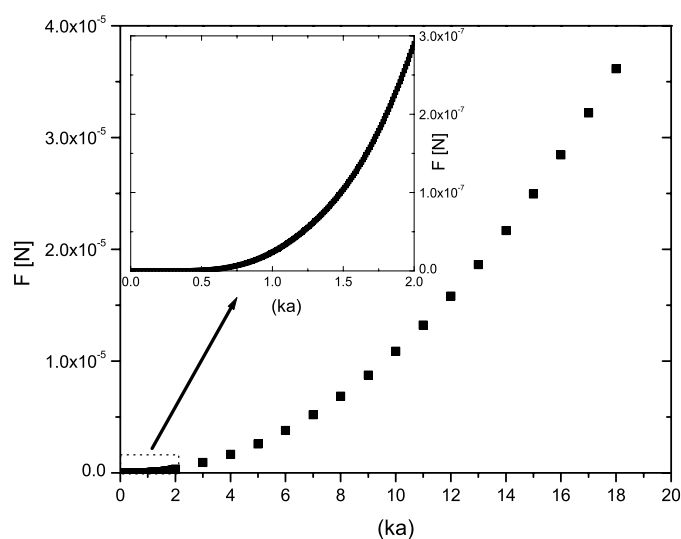


**Figure 1.** Radiation force (in N) versus  $ka$  (dimensionless) from equation (6). Inset: magnified view of the first part of the curve. The portions of the curves for  $ka < 2$  were calculated using the small  $ka$  expressions for the functions  $H_n$ .

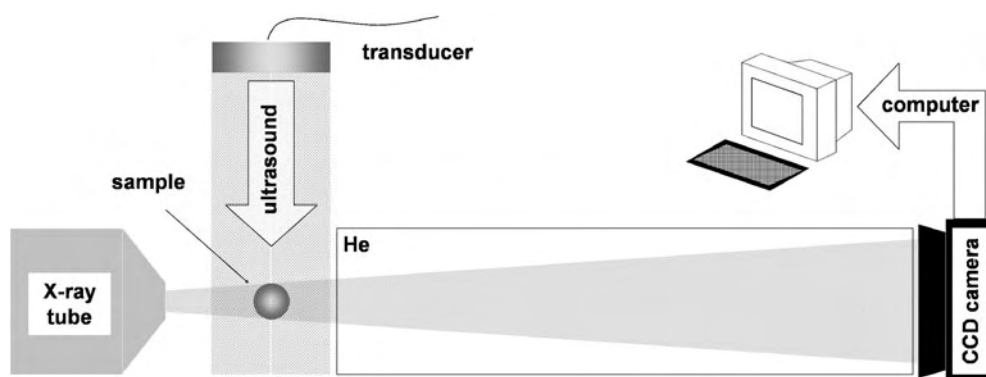


**Figure 2.** Diagram of the experimental apparatus. X-radiation generated by a microfocus tube penetrates a sample and is detected by a CCD camera that views a scintillation plate. The CCD camera is read by the computer which stores the images and performs the subtractions.

maximum of the emission x-ray spectrum was 40 keV. The source-to-detector distance was 2.6 m, while the sample-to-source distance was 0.35 m, giving a magnification of 7.5 and a maximum phase contrast (Pogany *et al* 1997) for spatial frequencies corresponding to  $4.3 \mu\text{m}$ .

The acoustic transducer used to produce radiation pressure was a 1 MHz,  $\text{LiNbO}_3$ -transducer located 3 cm from the bead. One end of the PVC sample tube was terminated by a synthetic, sound-absorbing plastic. The pulse train from the function generator (Agilent Model 33250A) used to drive the transducer consisted of  $15 \mu\text{s}$  bursts at a repetition rate of 133 Hz. The signal from the function generator was amplified by a power amplifier with a peak output power of 1.5 kW and delivered to the transducer. Although the low duty cycle of the pulse sequence, approximately 0.2%, resulted in a reduced time average acoustic power from the transducer, the resulting radiation pressure was sufficient to cause displacements that could be easily imaged with the CCD camera.

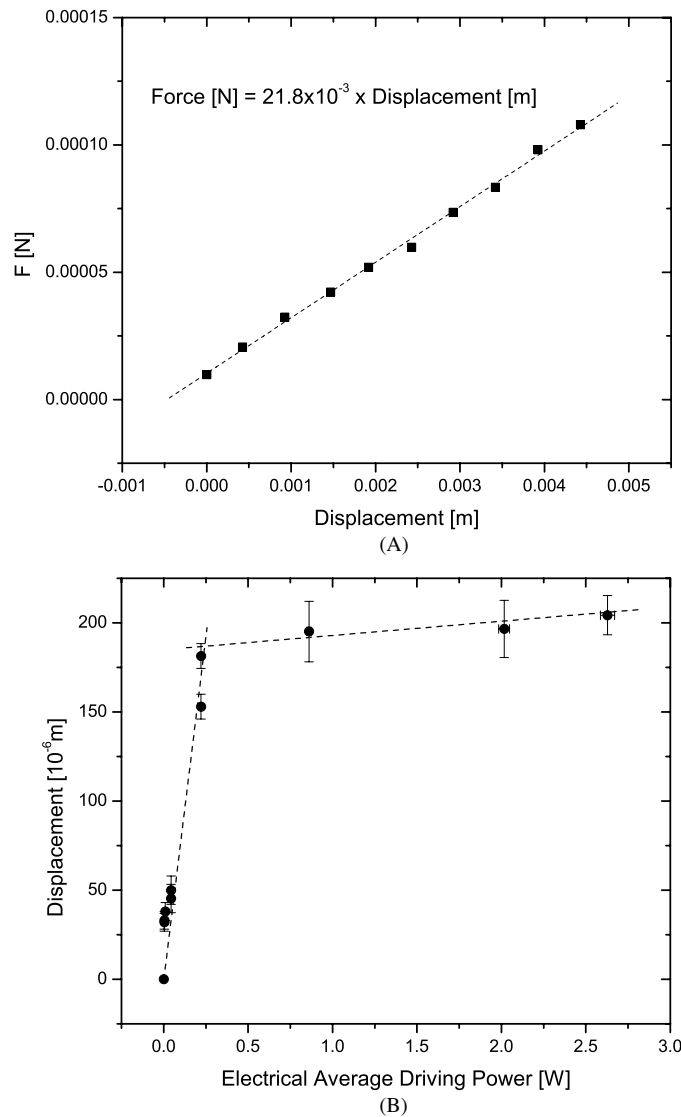


**Figure 3.** (A) Force on the glass fibre in N versus displacement in m. (B) Displacement of the Teflon bead attached to the fibre versus average electrical power delivered to the transducer.

A 3 mm diameter Teflon bead was attached to a glass fibre and suspended at the centre of the sample cell, which was filled with water. The glass fibre was calibrated by attaching it to a precision translation stage and using a laboratory balance to determine force versus fibre displacement. The data shown in figure 3(A) gave a force constant of  $2.18 \times 10^{-2} \text{ N m}^{-1}$  for the fibre. The total force on a bead suspended from the fibre is the sum of the restoring force from the fibre and the force from gravity, which can be written for small angles of deviation from the vertical as

$$F_{\text{exp}} = F_{\text{glassfibre}} + \frac{m_{\text{bead}} g d}{L} \quad (8)$$

where  $m_{\text{bead}}$  is the mass of the bead,  $g$  is the gravitational constant,  $L$  is the length of the fibre and  $d$  is its displacement. For the experiments described here, the mass of the bead was

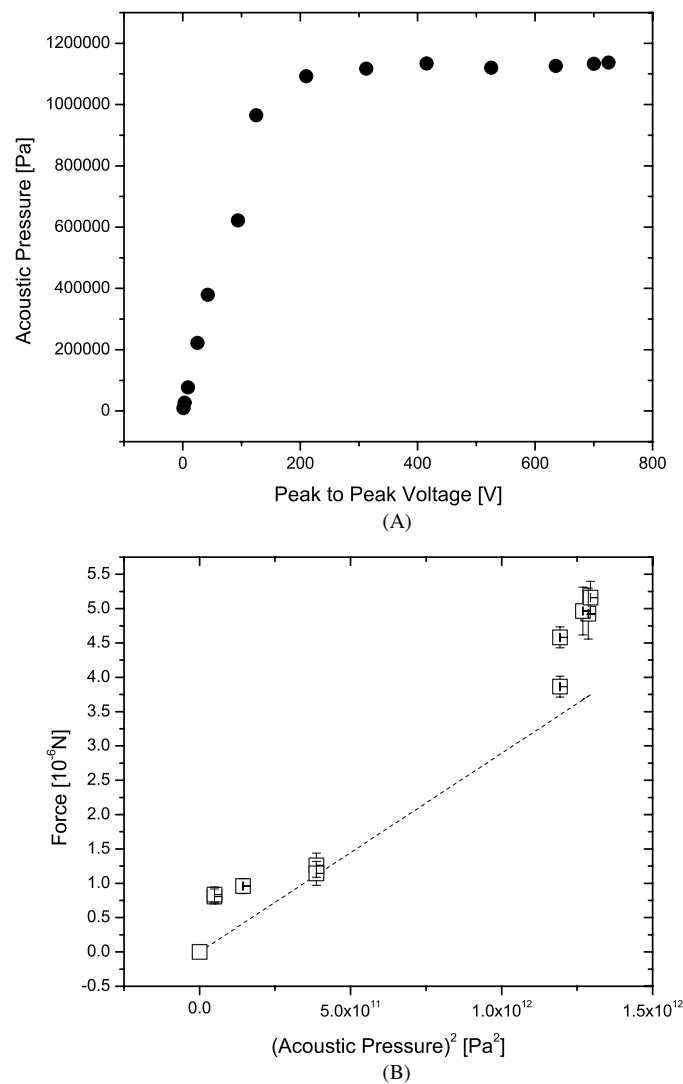


**Figure 4.** (A) Acoustic pressure in Pa from the calibrated transducer versus driving voltage from the power amplifier. (B) Force on the bead in N versus the square of the pressure from the transducer.

35 mg, and the length of the glass fibre was 10 cm. The displacement of the bead versus the time averaged electrical power delivered to the transducer is shown in figure 3(B). The break in the slope of the curve can be attributed to a departure of the efficiency of the transducer from linearity at high driving voltages. The acoustic pressure generated by the transducer at various power levels from the power amplifier was determined using a calibrated LiNiO<sub>3</sub> transducer (LaserSonics Technologies, Model WAT-04). The plot of acoustic pressure from the calibrated transducer versus average driving voltage applied to the transducer is shown in figure 4(A) which gives a curve with the same qualitative features as the curve in figure 3(B), and permits calibration of the transducer pressure in terms of the power amplifier output driving voltage. With this calibration, the plot in figure 3(B) can be converted to a plot of force versus the square of the acoustic pressure as shown in figure 4(B). The theoretical curve



from equation (6), also plotted in figure 4(B), shows reasonably good agreement with the experimental measurements. The maximum force recorded in the experiments was 5  $\mu\text{N}$ .

#### 4. Acoustically modulated x-ray phase contrast images

The method of modifying a phase contrast image using acoustic radiation pressure (Bailat *et al* 2004) consists of two steps: first, an x-ray image is made with a sound beam directed into a body to displace an object through acoustic radiation force and the image stored in a computer, second, another x-ray image of the object is taken, this time without the presence of the sound beam and the image is recorded in the computer. The two images are then subtracted pixel by pixel to give a subtracted phase contrast image, the component of the image from absorption contrast being largely eliminated, leaving a nearly pure phase contrast image, inherently background and flatfield corrected.

The principle of the method was demonstrated by taking images of two 3 mm diameter Teflon beads cast in a 6.5 cm long block of agarose. As shown in figure 5(A), the two beads were both within the field of the x-ray beam, but only one bead was irradiated with ultrasound. Figure 5(B) shows an image of the two beads where the microfocus x-ray tube was operated at high power, 80 W, to enlarge the diameter of the x-ray source to approximately 75  $\mu\text{m}$ . With this source diameter, the phase contrast component of the image disappears as a result of convolution of the phase contrast fringes over the source area of the x-ray beam. The exposure time for the image was 75 s. In figure 5(C) a conventional phase contrast image of the two beads is shown using the same total x-ray fluence as was used in figure 5(B), but with the x-ray tube operating at 10 W, where the source diameter was 25  $\mu\text{m}$ . The fringes at the perimeters of the beads, which serve to define the edges of the beads, are the result of interference from rapid phase variations in the x-ray paths, which, for a sphere, are largest at its perimeter (Wilkins *et al* 1996). The results of the image subtraction with the ultrasound directed onto only the bead closest to the x-ray tube are shown in figure 5(D). The bead that was not irradiated with ultrasound is not visible in the image, while the phase contrast component of the image of the irradiated bead shows up with the phase contrast component highlighted. The subtracted phase contrast image in figure 5(D) shows a reversal of the bright and dark regions at the perimeter of the bead in the direction of the ultrasound at the two sides of the bead (which appear at the top and bottom of figure 5(D)): the interior of the arc at the top of the figure appears bright while it is the exterior of the arc at the bottom of the figure that appears bright. The reversal of the shading is a consequence of subtraction—the opposite shading could be produced by reversal of the order of subtraction of the two images.

For our purposes, an analysis of the ultrasound-induced temperature increase in the selected tissue is important. A first approximation of the temperature change is given by

$$\Delta T = \frac{2\mu\nu}{\gamma} It \quad (9)$$

where  $\mu$  is the ultrasound attenuation coefficient in soft tissue ( $=0.05 \text{ cm}^{-1} \text{ MHz}^{-1}$ ),  $\nu$  is the ultrasound centre frequency ( $=1 \text{ MHz}$ ),  $\gamma$  is the heat capacity per unit volume of soft tissue ( $=4 \text{ W s cm}^{-3} \text{ }^\circ\text{C}^{-1}$ ),  $I$  is the ultrasound intensity in  $\text{W cm}^{-2}$  and  $t$  is the application time (15  $\mu\text{s}$ ) (Herman and Harris 2002). The maximum intensity can be calculated from the square of our maximum recorded pressure  $p_{\text{max}}^2$  using

$$I = \frac{p^2}{2\rho c} \quad (10)$$

where  $p_{\text{max}}^2 = 1.5 \times 10^{12} \text{ Pa}^2$  (Morse 1981). We obtain  $I = 5 \times 10^5 \text{ W m}^{-2} = 50 \text{ W cm}^{-2}$  and a subsequent temperature increase of approximately  $1.8 \times 10^{-5} \text{ }^\circ\text{C}$ . However in our

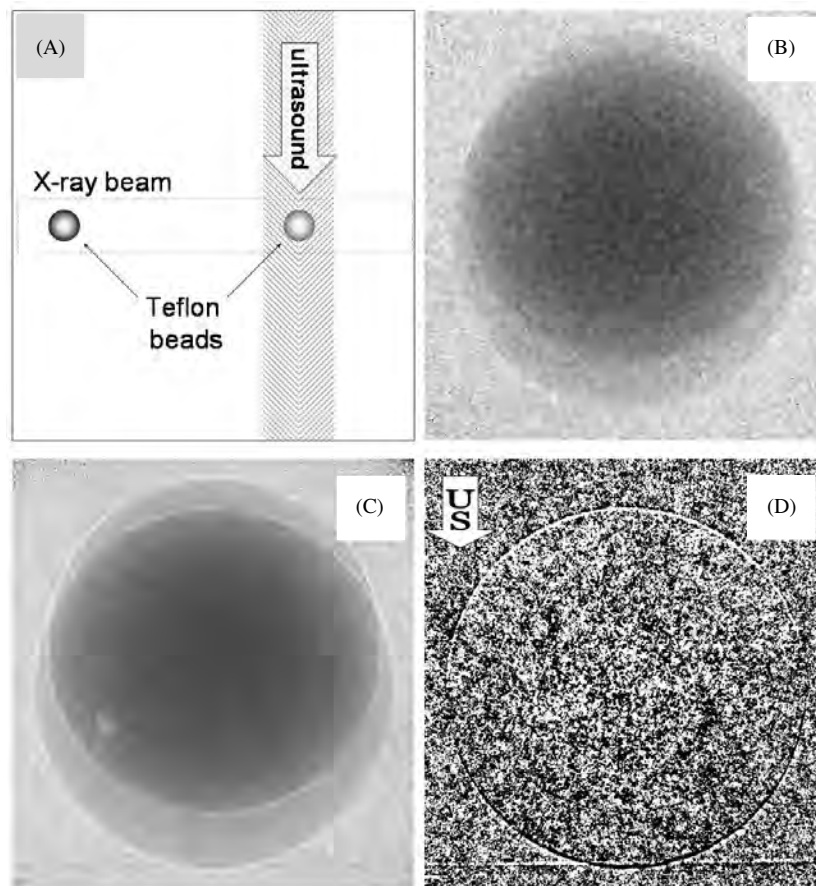


**Figure 5.** (A) Side view of the sample consisting of two Teflon beads cast in agarose. The two beads are separated by 3 cm. (B) Image of the beads with no phase contrast. (C) Image of the beads with phase contrast. (D) Subtracted image of the two beads. The bead irradiated with ultrasound is nearest the CCD camera and produces a slightly larger image than the bead located outside the sound beam. The x-ray tube voltage for the images was 90 kV. The image in (B) was taken with a 75 s exposure time with the x-ray tube operating at 80 W; the image in (C) was taken with eight times lower tube wattage and eight times longer exposure to give the same total x-ray fluence.

case, *burst* ultrasound, a more specific model which considers an ultrasound–bone interaction should be used as a worst-case scenario. The upper temperature limit for burst ultrasound is approximated by

$$\Delta T = 189.74 \times 10^{-6} I \sqrt{t} \quad (11)$$

with  $t$  in s and  $I$  in  $\text{W m}^{-2}$ . Using equation (11) with the same data given above results in an estimated temperature increase of  $0.37^\circ\text{C}$ . It should be noted that since (11) was derived specifically for the case of an ultrasound–bone interface the resulting temperature increase in the case of soft tissue would actually be smaller and would not present any dangers in biological applications.

In order to evaluate the method using tissue-like samples, a phantom of micron-sized agarose objects embedded in chicken breast was examined. The objects in the phantom consisted of pieces of a casting made by mixing carbon nanoparticles with agarose to achieve

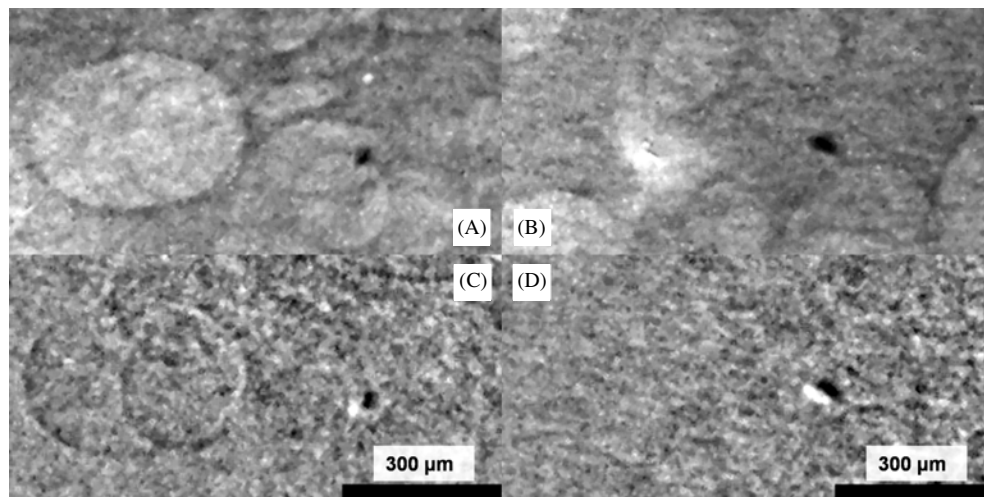


**Figure 6.** X-ray images of carbon enriched agarose objects embedded in chicken flesh: the round objects are fat bubbles in the chicken flesh. The entire sample is immersed in water. (A) and (B) conventional phase contrast images taken with a  $25\ \mu\text{m}$  diameter x-ray source, and (C) and (D) corresponding ultrasound enhanced x-ray phase contrast image.

a density approximately 14% higher than that of the chicken breast, comparable to the density difference between malignant and healthy human breast tissue as reported in Duck (1990), Johns and Yaffe (1987). The conventional phase contrast images in (A) and (B) for two different regions of the phantom show fat globules as being clearly outlined elliptical objects and the agarose objects as the dark masses, their estimated sizes being of the order of  $30 \times 30\ \mu\text{m}$  in (A) and  $30 \times 60\ \mu\text{m}$  in (B). The ultrasound contrast-enhanced x-ray images corresponding to (A) and (B) are shown in (C) and (D), respectively. Both regions of the phantom were irradiated with ultrasound. The subtracted images are seen to have increased contrast of the agarose objects, and the fat globules as well, highlighting those parts of the phantom displaced by the ultrasound. Both the fat globules and the higher density agarose objects are surrounded with identical shading, indicating motion in the same direction under the influence of the acoustic radiation pressure. Some of the objects, well defined on the images (A) and (B), are no longer visible in subtracted images and can therefore be identified as either artefacts arising from optical imperfections in the sample container or imaging optics. Note that a simple differential shift of two phase contrast images followed by their subtraction, as opposed to the present acoustically modified procedure, would leave artefacts from optical imperfections in the final image.

## 5. Discussion

The intensity profile of the subtracted image  $S(x)$  can be written as  $S(x) = I(x + h) - I(x)$  where  $h$  is the displacement caused by the application of ultrasound. For small  $h$ , it is appropriate to identify the subtracted image as approximately proportional to the space derivative of the phase contrast image in the direction of propagation of the ultrasound,  $S(x) = hI'(x)$ . As such, low spatial frequency features such as broad absorptions are suppressed in the image while the high frequency features such as those at interfaces between dissimilar materials are emphasized. When the acoustic displacement of an object is of the order of the fringe spacing of the phase contrast, the highlighting of the phase contrast

component of the image is maximal; the image of the object is then almost a pure phase contrast image responsive to changes in density. In general, the contrast in the image is determined by the combined effects of the tissue selectivity of the ultrasound based on differences in acoustic impedance, together with the response of phase contrast to density variation. The resolution, on the other hand, is governed by the parameters of conventional phase contrast imaging, which include the degree of spatial coherence of the x-ray beam and the sample-to-source and sample-to-image distances. A distinctive feature of the method described here is its vector character—the subtracted image shows only those features of the object moved along the propagation direction of the ultrasound, which is evident in figures 5 and 6. Clearly, it is possible to make multiple images where sound is directed from different angles into a body and to process the images to record displacement in more than one direction. Additionally, there are different ultrasound excitation schemes that can be employed leading to, for instance, standing acoustic waves, that can be generated within a body to give contrast dependent on eigenmodes of vibration and other elastic properties of the body, further enhancing the capability of x-rays to probe subtle physical properties of matter.

### Acknowledgment

The experiments reported here were supported by the US Army Medical Research and Materiel Command under Grant DAMD17-02-1-0307. Opinions, interpretations, conclusions and recommendations are those of the author and are not necessarily endorsed by the US Army. CRP acknowledges partial support from the US Department of Energy under contract DE-FG02-03ER15413.

### References

- Bailat C J, Hamilton T J, Rose-Petruck C and Diebold G J 2004 Acoustic radiation pressure: a 'phase contrast' agent for X-ray phase contrast imaging *Appl. Phys. Lett.* submitted
- Beckmann F, Bonse U, Busch F and Gunnewig O 1997 X-ray microtomography (microCT) using phase contrast for the investigation of organic matter *J. Comput. Assist. Tomogr.* **21** 539–53
- Beyer R T 1978 Radiation pressure—the history of a mislabeled tensor *J. Acoust. Soc. Am.* **63** 1925
- Born M and Wolf E 1980 *Principles of Optics* (Oxford: Pergamon)
- Chu B and Apfel R E 1982 Acoustic radiation pressure produced by a beam of sound *J. Acoust. Soc. Am.* **72** 1673
- Cowley J M 1984 *Diffraction Physics* (Amsterdam: North Holland)
- Duck F A 1990 *Physical Properties of Tissue* (London: Academic)
- Fatemi M and Greenleaf J F 1998 Ultrasound-stimulated vibro-acoustic spectrography *Science* **280** 82–5
- Fulvia Arfelli V B *et al* 2000 Mammography with synchrotron radiation: phase detection techniques *Radiology* **215** 286–93
- Gao L, Parker K J, Lerner R M and Levinson S F 1996 Imaging of the elastic properties of tissue—a review *Ultrasound Med. Biol.* **22** 959–77
- Herman B A and Harris G R 2002 Models and regulatory considerations for transient temperature rise during diagnostic ultrasound pulses *Ultrasound Med. Biol.* **28** 1217–24
- Johns P C and Yaffe M J 1987 X-ray characterisation of normal and neoplastic breast tissues *Phys. Med. Biol.* **32** 675–95
- King L V 1934 On the acoustic radiation pressure on spheres *Proc. R. Soc. A* **147** 212–40
- Krol A, Ikhlef A, Kieffer J C, Bassano D A, Chamberlain C C, Jiang Z, Pepin H and Prasad S C 1997a Laser-based microfocused x-ray source for mammography: feasibility study *Med. Phys.* **24** 725–32
- Krol A, Kieffer J C and Forster E 1997b Laser-driven x-ray source for diagnostic radiology *Proc. SPIE—Int. Soc. Opt. Eng.* **3157** 156–63
- McAlevey S A 2003 Estimates of echo correlation and measurement bias in acoustic radiation force impulse imaging *IEEE Trans. Ultrason. Ferroelectr. Freq. Control* **50** 631
- Momose A 1995 Demonstration of phase-contrast x-ray computed tomography using an x-ray interferometer *Nucl. Instrum. Methods Phys. Res.* **352** 622–8

- Morse P M 1981 *Vibration and Sound* (Acoustical Society of America)
- Muthupillai R, Lomas D J, Rossman P J, Greenleaf J F, Manduca A and Ehman R L 1995 Magnetic resonance elastography by direct visualization of propagating acoustic strain waves *Science* **269** 1854–7
- Nightingale K, Nightingale R, Palmeri M and Trahey G 1999 *IEEE Ultrason. Symp.* 1319
- Nightingale K, Stutz D, Bentley R and Trahey G 2002 *IEEE Symp.* 525
- Pogany A, Gao D and Wilkins S W 1997 Contrast and resolution in imaging with microfocus x-ray source *Rev. Sci. Instrum.* **68** 2774
- Sarvazyan A P 1998 Shear wave elasticity imaging: a new ultrasonic technology of medical diagnostics *Ultrasound Med. Biol.* **24** 1419
- Snigirev A, Snigireva I, Kohn V, Kuznetsov S and Schelokov I 1995 On the possibility of x-ray phase contrast microimaging by coherent high-energy synchrotron radiation *Rev. Sci. Instrum.* **66** 5486
- Westervelt P 1951 The theory of steady forces caused by sound waves *J. Acoust. Soc. Am.* **23** 312
- Wilkins S W, Gureyev T E, Gao D, Pogany A and Stevenson A W 1996 Phase-contrast imaging using polychromatic hard x-rays *Nature* **384** 335–8



## Acoustic radiation pressure: A “phase contrast” agent for x-ray phase contrast imaging

Claude J. Bailat,<sup>a)</sup> Theron J. Hamilton, Christoph Rose-Petruck, and Gerald J. Diebold  
*Department of Chemistry, Brown University Providence, Rhode Island 02912*

(Received 7 June 2004; accepted 10 September 2004)

We show that the radiation pressure exerted by a beam of ultrasound can be used for contrast enhancement in high-resolution x-ray imaging of tissue and soft materials. Interfacial features of objects are highlighted as a result of both the displacement introduced by the ultrasound and the inherent sensitivity of x-ray phase contrast imaging to density variations. The potential of the method is demonstrated by imaging microscopic tumor phantoms embedded into tissue with a thickness typically presented in mammography. The detection limit of micrometer size masses exceeds the resolution of currently available mammography imaging systems. The directionality of the acoustic radiation force and its localization in space permits the imaging of ultrasound-selected tissue volumes. The results presented here suggest that the method may permit the detection of tumors in soft tissue in their early stage of development. © 2004 American Institute of Physics. [DOI: 10.1063/1.1818337]

Phase contrast imaging differs from conventional x-ray shadowgraphy in the mechanism of contrast generation: while conventional shadowgraphy depends on absorption of x rays, phase contrast imaging is based on phase changes as x rays traverse a body giving rise to wave interference that results in intensity changes in the image. Fresnel–Huygens theory,<sup>1,2</sup> which governs image formation in general, describes contrast in an image as dependent on both absorption and phase contrast. However, only when sources with high spatial coherence, such as synchrotrons,<sup>3–5</sup> microfocus x-ray tubes,<sup>6,7</sup> or laser plasma x-ray sources<sup>8,9</sup> are employed is the phase contrast component of the image visible. Coherent sources give an image of a dense object embedded in lower density, soft tissue as a shadow of the object, caused by absorption, surrounded at its perimeter by light and dark interference fringes arising from rapid phase variations in the radiation at the interface between the two media. A detailed analysis of the relative contrast produced in an image for a fixed difference in density shows that phase contrast is more sensitive than absorption throughout most of the spectral region commonly used for diagnostic x-ray imaging.<sup>10</sup> For instance, the thickness of water needed to produce a 1% phase-contrast at 36 keV photon energy is 2500 times smaller than that required to produce the same contrast through absorption.<sup>10</sup>

Phase contrast in an image can be markedly enhanced by recording two images of an object, one where the object is displaced slightly through acoustic radiation pressure,<sup>11–13</sup> and a second where the object is unmoved, followed by subtraction of the two images. Acoustic radiation forces<sup>14–16</sup> can arise from either reflection of sound by an object or as a result of acoustic impedance changes (i.e., a variation in either density or sound speed) or by dissipative processes within the object resulting in absorption of the ultrasound energy. A number of “elastographic” studies, where tissue movement is monitored in response to radiation or mechanical pressure,<sup>11–13</sup> have shown that variations in Young’s modulus, which, in part, determines sound speed, permits acoustic differentiation of tissue. It is known, for instance,

that breast tumors have a significantly different Young’s modulus from surrounding tissue, and that tumors move as rigid bodies in response to acoustic radiation pressure.<sup>11–13,17,18</sup>

The subtractive phase contrast imaging method described here is based on acoustic radiation pressure to generate differential movement of components of a body having variations in acoustic impedance. First, a reference x-ray phase-contrast image is taken with a CCD camera and stored in a computer; next, a second x-ray image is recorded while the body is irradiated with a directed beam of ultrasound, under the same imaging conditions as the reference image. By subtracting the two images, a difference image of the temporally averaged displacement induced by the ultrasound is obtained.

As shown in Fig. 1, x rays were generated by a microfocus x-ray tube (Oxford Instruments, model UB-M1), operated at 90 kV, which has a minimum source diameter of 25  $\mu\text{m}$  as measured using a knife edge imaging procedure. The x rays were detected by a  $\text{Gd}_2\text{O}_2\text{S}(\text{Tb})$  fiber optic scintillation plate (Hamamatsu, Inc., model J6676) the fluorescence from which was imaged onto a liquid nitrogen cooled CCD camera (Roper Scientific model 7382-0001) interfaced to a computer. The source to detector distance was 2.6 m, while the sample to source distance was 35 cm, providing a magnification of 7.5. The x-ray beam exiting the sample propagated in a helium atmosphere in order to reduce x-ray

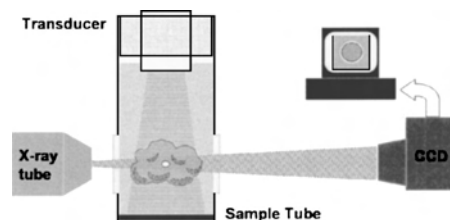


FIG. 1. Diagram of the experimental apparatus. X radiation generated by a microfocus tube penetrates a sample and is detected by a CCD camera that views a scintillator plate. The sample is located in a 3-cm-diam tube filled with water coupled to an ultrasound transducer. The intensity maximum in the x-ray spectrum detected at the scintillation screen was at 40 keV owing to x-ray spectrum hardening in the sample.

<sup>a)</sup>Electronic mail: bailat@brown.edu

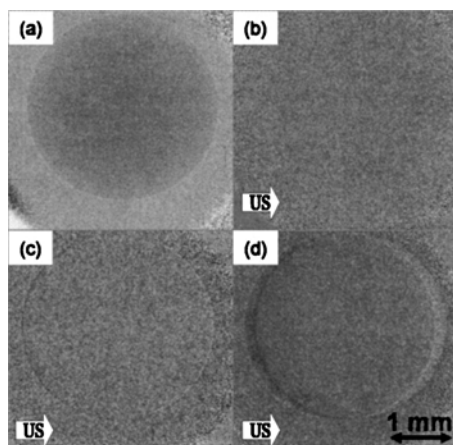


FIG. 2. (a) Conventional phase contrast image of a 3.05-mm-diam Teflon sphere suspended by a glass fiber in water showing both absorption and phase contrast. (b)–(d) Subtracted x-ray-acoustic phase contrast images taken with 10 kPa, 0.6 MPa, and 1.1 MPa average acoustic power applied to the transducer.

scatter. The sample was situated in the middle of a 3-cm-diam PVC tube which had portions machined out and replaced with Mylar. One end of the sample tube was terminated by a synthetic, sound-absorbing material while the other was sealed to a 2-cm-diam, 1 MHz, LiNb transducer, located 3 cm from the part of the sample traversed by the x-ray beam. The transducer was driven by a pulse train at a repetition rate of 133 Hz consisting of 15- $\mu$ s-long 1 MHz bursts amplified by a power amplifier with a peak power of 1 kW.

The principle of the method was demonstrated by taking images of a 3 mm diameter Teflon<sup>TM</sup> bead attached to a glass fiber, suspended in water, and irradiated with pulsed ultrasound. A conventional phase contrast image showing both absorption and phase contrast at the perimeter of the bead is shown in Fig. 2(a). Figures 2(b)–2(d) show subtracted images taken over a range of successively higher acoustic powers. The absence of features in Fig. 2(b) shows that at the lowest acoustic intensity, the displacement of the bead is smaller than the resolution of the x-ray imaging apparatus. In Fig. 2(d) the displacement of the bead<sup>19</sup> with an acoustic pressure of 1.1 MPa was determined from the x-ray image to be 200  $\mu$ m. Two effects from the subtraction of the image of the displaced bead from one of a stationary bead can be seen from examination of Fig. 2(c) and 2(d): first, the absorptive component of the contrast has been removed by the subtraction leaving only phase contrast in the image, and, second, the vector character of the image is evident in that interference fringes that lie parallel to the direction of the ultrasound induced motion are eliminated while those perpendicular to the direction of motion are highlighted.

The capability of the method for distinguishing only those objects irradiated with ultrasound was tested by imbedding two Teflon beads in agarose and directing a focused beam of ultrasound to irradiate only the bead nearest the x-ray source. Figures 3(a) and 3(b) show a conventional phase contrast image and an acoustically modulated phase contrast image, respectively. The ultrasound irradiated bead is easily identified with virtually no trace of the bead located outside the ultrasound field.

In order to evaluate the efficacy of applying the imaging method to tissue-like samples, the displacements of micron-sized pieces of agarose embedded in chicken breast were

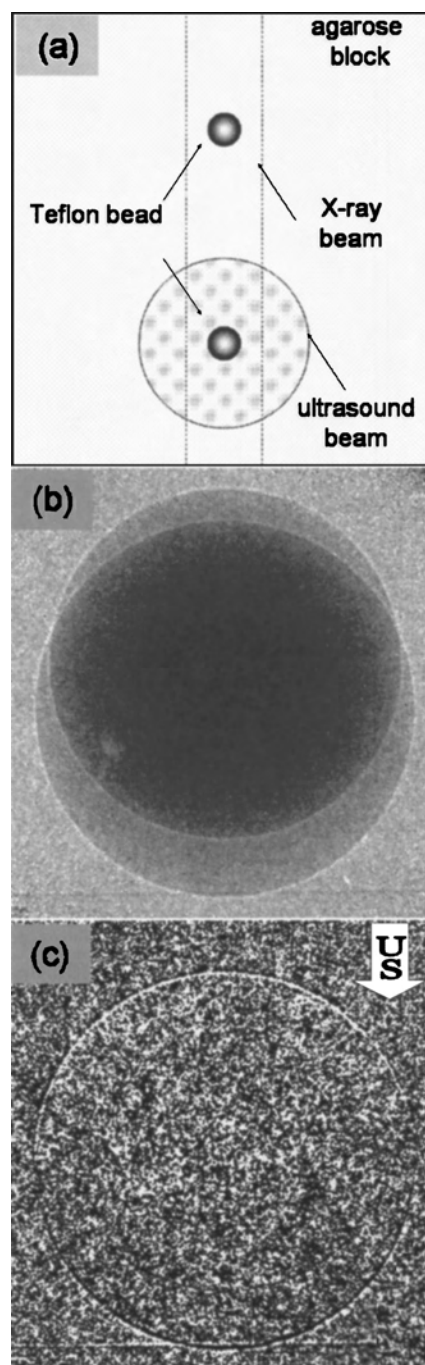


FIG. 3. (a) Top view of the sample consisting of two Teflon beads cast in agarose. The two beads are separated by 3 cm. (b) Conventional phase contrast image of two Teflon beads in agarose and (c) an acoustically modulated phase contrast image showing only the bead irradiated with ultrasound. The beads were located 2.5 cm apart.

measured. The agarose was enriched with carbon nanoparticles to achieve a density approximately 14% higher than that of the chicken breast in order to simulate the density difference between malignant and healthy human breast tissue.<sup>20,21</sup> Figure 4 shows a series of images of the chicken breast with the embedded objects. The flesh included fat globules which were deflected by the ultrasound field along with the agarose objects. All images contain identical detected x-ray doses and are reproduced with identical grey scale ranges of  $\pm 5\%$  of the average image intensity. The images and inserts display the same sample regions around three selected agarose objects, labeled 1–3 with estimated sizes of  $40 \times 53 \mu$ m (1),  $30 \times 46 \mu$ m (2), and  $20 \times 26 \mu$ m

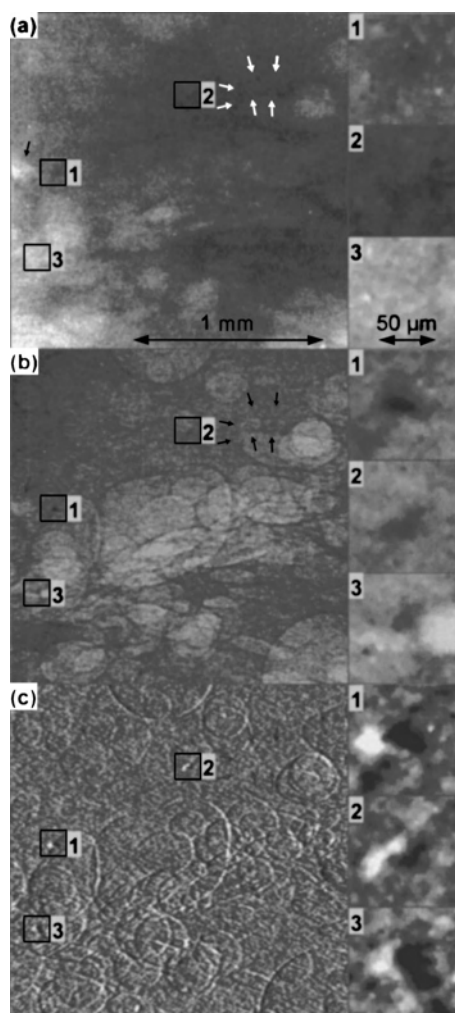


FIG. 4. X-ray images of carbon-enriched agarose objects embedded in chicken flesh: The round objects are fat globules in the chicken flesh. The entire sample is immersed in water. (a) X-ray image taken with an enlarged, 75- $\mu\text{m}$ -diam x-ray source; (b) conventional phase contrast image taken with a 25- $\mu\text{m}$ -diam x-ray source, and (c) x-ray ultrasound enhanced x-ray phase contrast image taken with 25- $\mu\text{m}$ -diam x-ray source. Tissue regions that are not shifted by the ultrasound field are indicated by arrows. Inset: magnified images of objects 1–3. The background noise remaining after subtraction in image (c) is the shot noise.

(3). Figure 4(a) shows an image of the chicken breast where the x-ray spot size in the microfocus tube was deliberately enlarged to 75  $\mu\text{m}$ . The phase contrast features of the image are almost entirely eliminated by convolution of the fringes over the spot size of the x-ray source—only the absorption component of the contrast remains in the image. Fatty material, which appears as nearly circular objects in the image, is visible but not well defined. Three different agarose pieces, referred to here as “objects,” are in the field of view of the imaging system. While object 1 is visible, object 2 is poorly defined, and object 3 is essentially indistinguishable from the background. The overall visibility of the objects in the tissue is low. Figure 4(b) shows a conventional phase contrast image with the x-ray tube operating with its minimum source diameter, 25  $\mu\text{m}$ . The image shows the fatty masses as being clearly outlined, permitting visual identification. Both objects 1 and 2 are visible, but object 3, again, is not easily distinguished from the background. The ultrasound contrast-enhanced x-ray image is shown in Fig. 4(c). The ultrasound displacement intensity was adjusted to give a tissue displacement of ap-

proximately one x-ray diffraction fringe. Objects 1, 2, and 3 are clearly visible and are marked with identical shading, indicating motion in the same direction under the influence of the acoustic radiation pressure. The objects identified by arrows in Figs. 4(a)–4(c) are no longer visible in the image and can therefore be identified as either artifacts arising from optical imperfections in the sample container or imaging optics, or, as objects lying outside the ultrasonic field.

The salient feature of the acoustic contrast x-ray imaging described here is its ability to highlight density variations: both the x-ray phase contrast and the movement of the selected object respond to density variations. Inherent in the method is the rejection of all features, whether absorptive or refractive, from any object that does not respond to ultrasonic radiation pressure, or any object within a body that is not within the ultrasonic field. This feature gives the diagnostician the ability to address a specific region within a body with directed ultrasound and to obtain an x-ray image of that region only. Without a significant reduction in the resolution of the present imaging system of 2.5  $\mu\text{m}/\text{pixel}$  at the object plane, a field of view of 10–15 cm in diameter is possible with current technology by using a larger imaging screen. The present results suggest application of the method to detection of small-sized tumors and other lesions distinguished from surrounding tissue by their elastic properties and density differences as small as a few percent.

These experiments were supported by the US Army Medical Research and Materiel Command under Grant No. DAMD17-02-1-0307. Opinions, interpretations, conclusions and recommendations are those of the author and are not necessarily endorsed by the US Army. C.R.P. acknowledges partial support for the experiment from the US Department of Energy under Contract No. DE-FG02-03ER15413.

- <sup>1</sup>M. Born and E. Wolf, *Principles of Optics* (Pergamon, Oxford, 1980).
- <sup>2</sup>J. M. Cowley, *Diffraction Physics* (North-Holland, Amsterdam, 1984).
- <sup>3</sup>A. Snigirev, I. Snigireva, V. Kohn, S. Kuznetsov, and I. Schelokov, *Rev. Sci. Instrum.* **66**, 5486 (1995).
- <sup>4</sup>F. Arfelli, V. Bonvicini, A. Bravin, G. Cantatore, E. Castelli et al., *Phys. Med. Biol.* **43**, 2845 (1998).
- <sup>5</sup>A. Momose, *Nucl. Instrum. Methods Phys. Res. A* **352**, 622 (1995).
- <sup>6</sup>A. Pogany, D. Gao, and S. W. Wilkins, *Rev. Sci. Instrum.* **68**, 2774 (1997).
- <sup>7</sup>S. W. Wilkins, T. E. Gureyev, D. Gao, A. Pogany, and A. W. Stevenson, *Nature (London)* **384**, 335 (1996).
- <sup>8</sup>A. Krol, A. Ikhjef, J. C. Kieffer, D. A. Bassano, C. C. Chamberlain, Z. Jiang, H. Pepin, and S. C. Prasad, *Med. Phys.* **24**, 725 (1997).
- <sup>9</sup>A. Krol, J. C. Kieffer, and E. Forster, *Proc. SPIE* **3157**, 156 (1997).
- <sup>10</sup>F. Beckmann, U. Bonse, F. Busch, and O. Gunnewig, *J. Comput. Assist. Tomogr.* **21**, 539 (1997).
- <sup>11</sup>L. Gao, K. J. Parker, R. M. Lerner, and S. F. Levinson, *Ultrasound Med. Biol.* **22**, 959 (1996).
- <sup>12</sup>K. Nightingale, R. Nightingale, M. Palmeri, and G. Trahey, *IEEE Ultrasonics Symposium*, 1999, p. 1319.
- <sup>13</sup>K. Nightingale, D. Stutz, R. Bentley, and G. Trahey, *IEEE Symposium*, 2002, p. 525.
- <sup>14</sup>P. Westervelt, *J. Acoust. Soc. Am.* **23**, 312 (1951).
- <sup>15</sup>B. Chu and R. E. Apfel, *J. Acoust. Soc. Am.* **72**, 1673 (1982).
- <sup>16</sup>R. T. Beyer, *J. Acoust. Soc. Am.* **63**, 1025 (1978).
- <sup>17</sup>A. P. Sarvazyan, *Ultrasound Med. Biol.* **24**, 1419 (1998).
- <sup>18</sup>S. A. McAleavey, *IEEE Trans. Ultrason. Ferroelectr. Freq. Control* **50**, 631 (2003).
- <sup>19</sup>In separate experiments, it was determined that the movement of the bead was caused by acoustic radiation forces, and not streaming.
- <sup>20</sup>F. A. Duck, *Physical Properties of Tissue* (Academic, London, 1990).
- <sup>21</sup>P. C. Johns and M. J. Yaffe, *Phys. Med. Biol.* **32**, 675 (1987).



## Imaging based on the ultrasonic vibration potential

Andrew C. Beveridge, Shougang Wang, and Gerald J. Diebold<sup>a)</sup>

Department of Chemistry, Brown University, Providence, Rhode Island 02912

(Received 16 June 2004; accepted 27 September 2004)

An ultrasonic wave traversing a colloidal suspension causes distortion of the charge distributions at the sites of individual colloidal particles producing a voltage known as the ultrasonic vibration potential. We show how imaging of colloidal regions within a body can be carried out using a beam of ultrasound to produce a radio frequency vibration potential. A theory for image formation shows that Fourier transformation of vibration potential signals processed by a mixer and low pass filter gives the spatial distribution of colloid. The salient feature of the method, insofar as medical imaging is concerned, is its contrast mechanism. © 2004 American Institute of Physics.

[DOI: 10.1063/1.1827350]

Colloids are suspensions of charged particles in a liquid with a counter-charge distributed in the fluid around each particle. The counter-charge, which is normally a spherical distribution around the particles, gives the solution overall charge neutrality and, together with the charge on the particle surface, stabilizes the suspension against particle agglomeration. When sound propagates through a suspension where the particles have either a higher or lower density than that of the surrounding fluid, the amplitude and phase of the particle motion, owing to the difference in inertia between the particle and the volume of fluid it displaces, differs from that of the fluid so that fluid flows back and forth relative to the particle on alternating phases of the acoustic cycle. Since the counter-charge is carried by the fluid, the oscillatory motion of the fluid relative to the particle distorts the normally spherical counter-charge distribution creating an oscillating dipole at the site of each particle, which, when added over a half wavelength of the sound wave, results in a macroscopic voltage that can be recorded by a pair of electrodes placed in the solution. Similar considerations of particle inertia show that vibration potentials are generated in ionic solutions as well. The theory of the colloidal vibration potential<sup>1-3</sup> gives the electric field  $\mathbf{E}$  generated by an acoustic pressure  $p$  as  $\mathbf{E} = -(\varphi \Delta \rho \mu_E / \rho K^*) \nabla p$ , where  $\varphi$  is the volume fraction of particles,  $\Delta \rho$  is the density difference between the particles and the solvent,  $\mu_E$  is the electrophoretic mobility of the particles,  $\rho$  is the solution density, and  $K^*$  is the conductivity of the suspension.<sup>4</sup> According to linear acoustics of an inviscid medium, the gradient of the pressure is related to the fluid acceleration  $\ddot{\mathbf{u}}(\mathbf{r}, t)$  through  $\ddot{\mathbf{u}} = -\nabla p / \rho$ , which, for a plane wave propagating along the  $z$  axis, can be written in terms of the displacement  $\mathbf{u}(z, t)$  at a time  $t$  as  $\ddot{\mathbf{u}}(z, t) = -\omega^2 \mathbf{u}(z, t)$ , where  $\omega$  is the radial frequency of the wave. Since the potential across the region of integration  $\Delta \Psi$  is given by  $\Delta \Psi(t) = \int \mathbf{E} \cdot d\mathbf{z}$ , it follows for a one-dimensional geometry<sup>5,6</sup> that

$$\Delta \Psi(t) = \Gamma \int \hat{u}(\hat{z}, t) c(\hat{z}) d\hat{z}, \quad (1)$$

where the quantities in the integral marked with a hacek are dimensionless, i.e.,  $\hat{z} = z/L$  and  $\hat{u} = u/u_0$ ,  $u_0$  is the magnitude of the acoustic displacement in the plane wave,  $L$  is the

length of the colloidal region, and  $\Gamma$  is a proportionality constant given by  $\Gamma = -\omega^2 \varphi \Delta \mu_E u_0 L / \rho K^*$ , with the integration extending over the spatial extent of the sound wave.

The apparatus used for vibration potential imaging, as shown in Fig. 1, consisted of a cell containing the object of interest, equipped with acoustic delay lines on the top and bottom of the cell, with two electrodes at opposite ends of the cell, mounted directly on the faces of the delay lines. One electrode was attached to an aluminum housing surrounding the cell, which forms a ground, and the other electrode was connected to a feedthrough and cable leading to a rf amplifier (Analog Devices, Inc. Model AD 8021) with a voltage amplification of 100. Ultrasound was generated by a

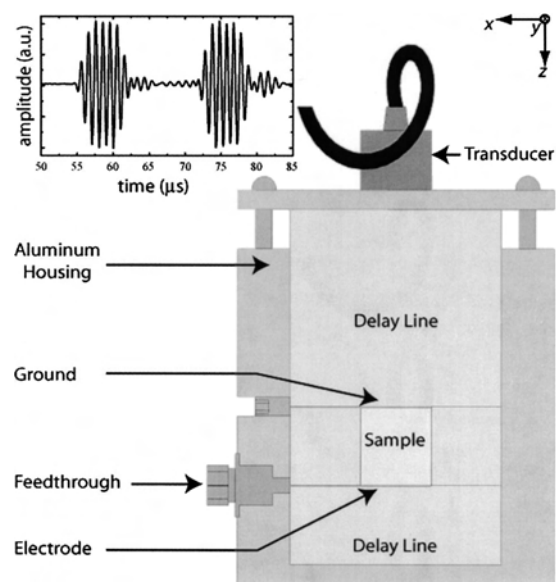


FIG. 1. Diagram of the apparatus. Ultrasound from the transducer enters and exits the colloidal region of the cell through a variable length (approximately 50 mm long) acoustic delay lines. An aluminum housing, which serves as the electrical ground, supports the cell and the delay lines. The delay lines were either acrylic blocks with copper tape electrodes mounted on the faces of the delay lines or water columns with 90  $\mu\text{m}$  wires used as electrodes and plastic membranes used to separate the colloid from the water. For experiments where an image is generated, the transducer is scanned in the  $XY$  plane and the vibration potential signal after processing is stored in a computer as a function of position. Inset: Oscilloscope trace of vibration potential (in arbitrary units) vs time generated by approximately six pulses of 1 MHz ultrasound traversing a water delay line into a 2.538-cm-thick layer of colloidal silica.

<sup>a)</sup>Electronic mail: gerald\_diebold@brown.edu

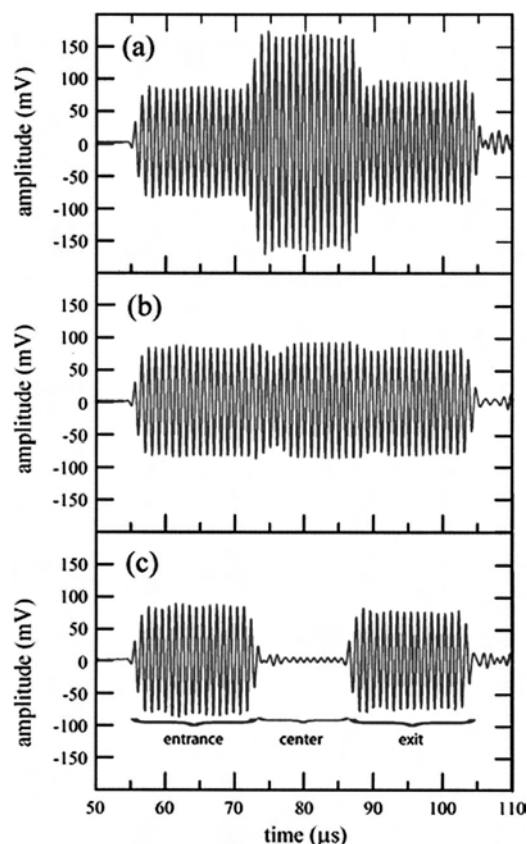


FIG. 2. Oscilloscope traces of the vibration potential generated by 32 pulses of (a) 1.0165 MHz, (b) 1.0069 MHz, and (c) 0.9865 MHz ultrasound traversing a saline solution delay line into 2.5-cm-thick layer of colloidal silica. Signals were averaged over 64 repetitions of the pulse burst. The oscilloscope voltage is referred to the electrodes after amplification. The initial (55–75  $\mu$ s) and final (85–105  $\mu$ s) parts of the wave forms correspond to entrance of the ultrasound into the colloidal layer and exit from the layer, respectively. The central portions of the wave forms show the effects of integration of the wave over the entire length of the colloidal layer. For the 0.9865 MHz trace, the colloidal layer thickness is an integral number of sound wavelengths giving complete cancellation of the voltage in the center of the wave form.

2.54-cm-diameter LiNbO<sub>3</sub> transducer driven by a programmable pulse generator, or by a function generator that drove a power amplifier.

An experiment was carried out where a short burst of ultrasound consisting of six cycles of a 1 MHz sine wave, generated at a repetition rate of 60 Hz, was applied to the cell which contained a 2.538-cm-thick colloidal layer. The spatial extent of the pulse burst was smaller than the length of the colloid layer in the cell. The signal from a colloidal silica sample<sup>7</sup> recorded by the oscilloscope is shown in the inset of Fig. 1. As the ultrasound burst either enters or leaves the colloid, an alternating vibration potential is produced. However, when the entire six cycles of the burst of ultrasound are totally confined within the colloidal region, the positive and negative contributions to the potential, in agreement with Eq. (1), integrate to zero giving a null voltage.

For bursts of ultrasound whose extent in space is larger than the thickness of the colloidal layer, the voltages from individual half-cycles of the sound wave, according to Eq. (1), can be nonzero or add to zero depending on thickness of the layer and the wavelength of sound. Figure 2 shows vibration potential signals at three different frequencies produced by a 32 cycle burst of ultrasound whose spatial extent

is large compared with the 2.538 cm layer thickness, showing the effect of voltage integration over the length of the cell. Evaluation of Eq. (1) for a wave that fills the colloidal region shows that the zeroes in the signal occur when  $n\lambda = L$ , where  $n$  is an integer,  $\lambda$  is the wavelength of the sound, and  $L$  is the length of the layer. It follows for two frequencies  $f_2$  and  $f_1$ , which have zeroes for integer values of the wavelength  $n_2$  and  $n_1$ , that  $(n_2 - n_1)c = L(f_2 - f_1)$  where  $c$  is the sound speed which permits determination of the layer thickness. Data taken over a more extensive range than shown in Fig. 2, from 0.8984 to 1.0765 MHz, gave the length of colloid as  $2.553 \pm 0.025$  cm.

There are three kinds of imaging that follow from Eq. (1) for determining the  $Z$  dependence (as defined in Fig. 1) of colloidal distributions in space for a focused transducer scanned in the  $XY$  plane. The first method uses the amplitude of the vibration potential recorded with a lock-in amplifier as the transducer is rastered in the  $XY$  plane to form an image. The second method, analogous to conventional pulse-echo imaging, is based on recording the delay time between the appearance of the vibration potential signal and the time of launching of the acoustic burst. The delay time, together with the sound speed, gives the distance between the colloidal object and the transducer. For the third method, consider an arbitrary distribution of colloid in space  $c(z)$  traversed by a plane wave propagating in the  $Z$  direction. It is straightforward to show that accumulation of in-phase and quadrature voltages from a mixer and low pass filter, recorded over a range of  $k$ , or, equivalently, over a range of frequencies, gives the distribution of colloid in space,  $c(z)$ , through Fourier transformation as

$$c(z) = \frac{4}{\Gamma} \left[ \int L_I(k) \cos(kz) dk + \int L_Q(k) \sin(kz) dk \right], \quad (2)$$

where  $L_I(k)$  and  $L_Q(k)$  are the in-phase and quadrature components of the signal following low pass filtering. Equation (2) shows that the vibration potential can be inverted to determine any arbitrary colloid distribution in space  $c(z)$ . It is noteworthy that a layer of uniform thickness extending along the  $z$  axis a distance  $L$  from the origin gives  $L_I(k) = (\Gamma/2k) \sin(kL)$  and  $L_Q(k) = (\Gamma/2k)[1 - \cos(kL)]$ , the first of which can be written in terms of the familiar sinc function as  $L_I(k) = (\Gamma L/2) \text{sinc}(kL)$ . The amplitudes of the central portions of the traces in Fig. 2 give three points on the sinc curve  $L_I(k)$ .

Experiments were carried out with objects to give a demonstration of vibration potential imaging. An agarose block containing colloidal discs was placed at the bottom of the cell with the agarose making contact with the electrode leading to the preamplifier. The apparatus shown in Fig. 1 was modified so that a saline solution in a cylindrical enclosure replaced the acrylic delay line at the top of the cell. The salt solution, which formed one of the electrodes for the cell, made contact with the metal housing of the cell providing both a ground for the rf signal and a delay line for a beam of ultrasound<sup>8</sup> from a 5.1-cm-diam, 15.2 cm focal length LiNbO<sub>3</sub> transducer (Valpey Fisher Model E1129). The ultrasound beam was approximately 3 mm in diameter beam over the length of the sample. The transducer was driven by a pulse generator that produced 900 kHz voltage bursts 28  $\mu$ s long with a repetition rate of 50 Hz, amplified by a gated power amplifier. The position of the transducer relative to the

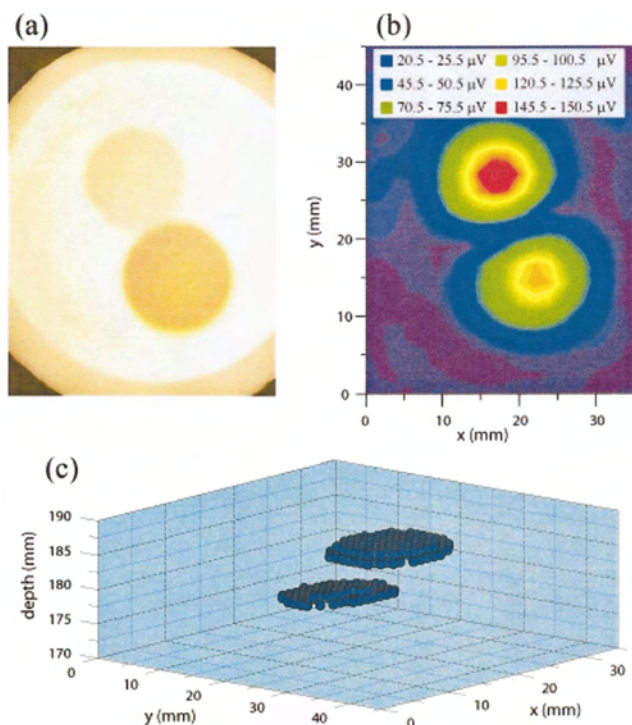


FIG. 3. (Color) (a) Photograph, (b) two-dimensional amplitude, and (c) three-dimensional surface vibration potential images of thin layer colloidal phantoms cast in agarose. In (c), plotted with the ultrasound beam propagating upwards, the depth was determined from the delay time of the vibration potential signal relative to the launching of the acoustic burst; only the upper surfaces of the colloidal objects are recorded. The  $XY$  scan data were recorded at intervals of 1 mm with an integration time at each pixel of 1 s. The driving voltage on the focused  $\text{LiNbO}_3$  transducer was 250 V peak-to-peak.

phantoms in the cell was scanned by precision translation stages controlled by a computer. Signals from the preamplifier were fed to both a digitizer and a lock-in amplifier as transducer was rastered in the  $X$  and  $Y$  directions across the sample.

Figure 3 shows a photograph, an amplitude image, and a time of arrival image of a 25-mm-thick agarose block, which contained two 2-mm-thick silica colloid discs, 13 mm in diameter, made by mixing silica colloid with agarose, with one disc located 11 mm above the other and displaced in the  $Y$  direction. The time of arrival image was made by setting a threshold signal to yield a unit amplitude output, and discarding all signals with smaller amplitudes than the threshold. Note that the signal-to-noise ratio in the images could be improved significantly by employing an ultrasonic wave train with a higher duty cycle than the 0.2% duty cycle used here.

Experiments were also carried out to determine the magnitudes of vibration potentials from colloidal and ionic solutions, and biological samples. The apparatus shown in Fig. 1 was equipped with acrylic delay lines, and a 2.54-cm-diameter, planar pzt transducer driven by a single, negative voltage spike from a pulse generator (Panametrics, Inc. Model 5058PR). A number of common colloidal and ionic solutions<sup>9</sup> were shown to produce sizeable vibration potentials (given in parentheses), including colloidal gold (15  $\mu\text{V}$ ), India ink (44  $\mu\text{V}$ ), colloidal silver (13  $\mu\text{V}$ ),  $\text{LiCl}$  (6.9  $\mu\text{V}$ ),  $\text{NaCl}$  (23  $\mu\text{V}$ ),  $\text{KCl}$  (39  $\mu\text{V}$ ),  $\text{RbCl}$  (85  $\mu\text{V}$ ), and  $\text{CsCl}$  (132  $\mu\text{V}$ ). Insofar as tissue imaging is concerned,

muscle tissue from chicken breast, beef, and pork all produced vibration potentials smaller than 0.02  $\mu\text{V}$  while whole blood,<sup>10</sup> which is both colloidal, as a result of the presence of red blood cells, and ionic, from dissolved electrolytes, gave comparatively large signals, on the order of 10  $\mu\text{V}$  at 500 kHz. Further experiments with colloids placed between 4-mm-thick layers of chicken breast, with the breast tissue placed in contact with the electrodes, showed that vibration potential generated by the colloid within the weakly conducting muscle tissue is transmitted to the surface electrodes and can be recorded.

While the resolution in both vibration potential and conventional ultrasonic pulse-echo imaging are governed by the same principles of linear acoustics, the contrast mechanisms through which the images are formed in the two imaging methods are altogether different. In vibration potential imaging, contrast is determined by differences in electroacoustic properties within the irradiated body, i.e., by differences in the colloidal or ionic concentration or even the presence of such solutions, whereas in conventional ultrasonic pulse-echo imaging, contrast is determined by relative differences in acoustic impedance. In comparing vibration potential imaging with established methods such as optical or x-ray imaging, it is important to note that resolution is ultimately limited by the wavelength of the radiation employed.<sup>11</sup> An additional factor in considering the resolution of vibration potential imaging is that reflections of the acoustic waves at interfaces can cause changes in the vibration potential signal, complicating the analysis of data. Insofar as tissue imaging is concerned, the large difference in signal amplitudes between blood and muscle tissue found here, which is greater than a factor of 500, points up its contrast mechanism, which differs fundamentally from that for radiographic, photoacoustic, optical, or ultrasonic imaging, and which suggests its use, among other things, for detection of tumors, which are known to be highly vascularized.

The experiments reported here were supported by the US Army Medical Research and Materiel Command under Grant DAMD17-02-1-0307. Opinions, interpretations, conclusions and recommendations are those of the author and are not necessarily endorsed by the US Army. The authors are grateful for the assistance of S. Woythayler for design of the rf amplifier and electronics.

<sup>1</sup>R. Zana and E. Yeager, in *Modern Aspects of Electrochemistry*, edited by J. O. Bockris, B. E. Conway, and R. E. White (Plenum, New York, 1982).

<sup>2</sup>R. J. Hunter, *Colloids Surf.*, A **141**, 37 (1998).

<sup>3</sup>A. S. Dukhin and P. J. Goetz, *Colloids Surf.*, A **192**, 267 (2001).

<sup>4</sup>We use Eq. (4.2) from R. W. O'Brien, *J. Fluid Mech.* **190**, 71 (1988).

<sup>5</sup>For a more complete description of vibration potential imaging in three dimensions see V. E. Gusev and G. J. Diebold (unpublished).

<sup>6</sup>The analysis here has ignored the effects of reflection of ultrasound at boundaries within the irradiated body.

<sup>7</sup>The colloidal silica Snow Tex (Nissan, Inc., Houston, TX) was an aqueous suspension of 20–30 nm silica with a particle concentration of  $10^{15}/\text{cm}^3$ .

<sup>8</sup>The wave front in a focused sound beam has curvature which must be taken into account in a precise formulation of the problem.

<sup>9</sup>The colloidal gold (Ted Pella, Inc., Redding, CA) was an aqueous suspension of 100-nm-diam particles, at a concentration of  $5 \times 10^9/\text{cm}^3$ . India ink (Higgins, Inc., Levenburgh, TN) is an aqueous suspension of carbon with a surfactant added for stability. The colloidal silver was an aqueous suspension of 80-nm-diam particles, at a concentration of  $1.1 \times 10^{10}/\text{cm}^3$ . The salt concentrations were 4 M. Production of a vibration potential by these solutions is well known from previous reports in the literature.

<sup>10</sup>Whole canine blood preserved with EDTA.

<sup>11</sup>The resolution of nuclear magnetic resonance imaging is not determined by the wavelength of the radiation employed.



# Acoustically Modulated X-ray Phase Contrast and Vibration Potential Imaging

A. C. Beveridge<sup>1</sup>, C. J. Bailat<sup>1</sup>, T. J. Hamilton<sup>1</sup>, S. Wang<sup>1</sup>,

C. Rose-Petruck<sup>1</sup>, V. E. Gusev<sup>2</sup>, and G. J. Diebold<sup>1</sup>

<sup>1</sup>Department of Chemistry Brown University, Providence, RI, USA, 02912.

<sup>2</sup>Université du Maine, av. Messiaen, 72085 LeMans, Cedex 09 France.

## ABSTRACT

Recording of an ultrasonic vibration potential when a burst of ultrasound traverses a body containing a colloidal object can be used as the basis for an imaging method. The fundamentals of the theory of signal production and experimental demonstration of the imaging method are given. In a second imaging method, the use of ultrasound to modify x-ray phase contrast images where the ultrasound acts as a kind of "phase contrast" agent used to translate objects in space is demonstrated.

**Keywords:** phase contrast, x-ray, vibration potential, imaging

## 1. INTRODUCTION

A voltage, known as the ultrasonic vibration potential, produced by the passage of ultrasound through a colloidal or ionic suspension arises from charge separation induced by the sound wave. In the case of a colloid, particles suspended in solution are charged as a result of chemical groups attached to the particles. In order to give the solution overall charge neutrality, there must therefore be a counter charge in the fluid. The spatial distribution of counter charge around a spherical particle, by symmetry, must be spherical. Except in cases where the density of the particle and the fluid are identical, when a sound wave passes through a colloidal suspension, the motions of the particles and fluid differ owing to their different inertias, the result of which is fluid flow around the surface of the particle. A dense particle in a low density fluid, for example, will execute a smaller amplitude motion than the fluid, and will have a phase lag in its motion relative to that of the fluid. When fluid flows over a suspended particle, it carries the counter charge in the fluid resulting in a distortion of the normally spherical distribution of charge around the particle. The result is the production of a dipole at the site of each colloidal particle, which, in a suspension of particles, can be detected as a macroscopic voltage by placing electrodes in the solution a distance smaller than one half wavelength of the acoustic wave. For ionic solutions, the different mass of the anion and cation can result in a corresponding charge separation in solution that gives rise to a macroscopic voltage. The vibration potential was originally predicted by Debye<sup>1</sup> for ionic solutions and was subsequently found in colloidal suspensions, which generally give larger amplitude vibration potentials than ionic solutions. The theory of the effect has been reviewed by several authors.<sup>2-4</sup>

A second method of imaging discussed here uses phase contrast x-ray imaging. Phase contrast imaging refers to the use of a spatially coherent source of x-radiation to form an image. Sources for the radiation are typically microfocus x-ray tubes that approximate a point giving a nearly spherical x-ray wave front, or a synchrotron which gives a beam that approximates a plane wave. The salient feature of phase contrast imaging is that the contrast in the image is based on variations in the real part of the index of refraction rather than absorption. In the method presented here, one image is taken in the presence of ultrasound and a second image is taken without the ultrasound. The effect of the ultrasound is to move objects within a body so that when the two images are subtracted, the resulting image retains only features of objects that have been translated in space by the ultrasonic radiation pressure. The inherently high resolution of x-ray imaging is preserved in the image, while the contrast depends, in part, on the response to the acoustic radiation pressure.

---

Further author information: (Send correspondence to GJD.)  
E-mail: Gerald\_Diebold@Brown.edu, Telephone: 1 401 863 3586

For the description of vibration potential imaging, we outline the problem of determining the current in a pair of electrodes kept at ground potential generated by a colloidal object with an arbitrary shape imbedded in a medium that is a dielectric or a weak conductor. Experimental results are given for objects with simple geometries. For x-ray phase contrast imaging, we give the principles of image generation and show how density changes in a body give an image qualitatively different from the usual shadowgraph recorded in an x-ray image where contrast is based on absorption. The modification of an image using ultrasonic radiation pressure is demonstrated for an object imbedded in muscle tissue.

## 2. THE ULTRASONIC VIBRATION POTENTIAL

### 2.1. Mathematics of Image Formation

The electric field  $\mathbf{E}$  produced across a region of colloid by a pressure  $p$ , has been given by O'Brien<sup>6</sup> as

$$\mathbf{E} = \frac{f \Delta \rho_m \mu_E}{\rho_m \sigma^*} \nabla p, \quad (1)$$

where  $f$  is the volume fraction of colloidal particles in the fluid,  $\mu_E$  is the electrophoretic mobility of the particles,  $\rho_m$  is the mass density of the suspension, and  $\Delta \rho_m$  is the difference in density between the particles and the surrounding fluid, and  $\sigma^*$  is the complex conductivity.

Consider a body that is either a dielectric or a weak conductor, or which has both properties. It is assumed that there is an object within the body that is colloidal or ionic and which generates a vibration potential when it is irradiated with ultrasound. The effect of the ultrasound is to produce a polarization  $\mathbf{P}_a$  within the object, so that the electric displacement becomes  $\mathbf{D} = \varepsilon \mathbf{E} + \mathbf{P}_a$ , where  $\varepsilon$  is the dielectric constant of the object and the surrounding medium, assumed to be identical. The polarization produced by the sound can be written as

$$\mathbf{P}_a = \alpha(\mathbf{x}, \omega) \nabla p$$

where the parameter  $\alpha(\mathbf{x}, \omega)$  is given by

$$\alpha(\mathbf{x}, \omega) = \varepsilon f \Delta \rho_m \mu_E / \rho_m \sigma^*. \quad (2)$$

The function  $\alpha(\mathbf{x}, \omega)$  is taken to contain the space dependence of the concentration of the colloidal or the ionic solution, that is, the geometry of the object is defined by  $\alpha(\mathbf{x}, \omega)$ . For the present problem biological tissue is considered. Owing to the high absorption of ultrasound by water at frequencies above 10 MHz, the frequency range of typical experiments will be limited; it is thus reasonable to employ the quasi-electrostatic approximation  $\nabla \times \mathbf{E} \simeq 0$ , so that the electric field generated by the colloid can be written in terms of a potential  $\phi$  as  $\mathbf{E} = -\nabla \phi$ . Through the use of Maxwell's equations it can be shown<sup>7</sup> that the potential obeys

$$\sigma \nabla^2 \phi + \varepsilon \frac{\partial}{\partial t} \nabla^2 \phi = \frac{\partial}{\partial t} (\nabla \cdot \mathbf{P}_a), \quad (3)$$

which is the fundamental equation for production of the potential distribution in space arising from the vibration potential generated by the object. Note that Eq. 3 points to two mechanisms for production of the potential, one dependent on the conductivity of the body, and the other on its dielectric constant. A considerable simplification of the mathematics can be found by converting Eq. 3, a time domain expression, into the frequency domain which gives

$$\nabla^2 \tilde{\phi} = \nabla \cdot (\alpha^\dagger \nabla \tilde{p}), \quad (4)$$

where  $\alpha^\dagger$  is given by  $\alpha^\dagger(\mathbf{x}, \omega) = \frac{i\omega}{\sigma + i\omega\varepsilon} \alpha(\mathbf{x}, \omega)$ , and where frequency domain quantities are denoted with a tilde. Equation 4 is of the form of Poisson's equation for  $\tilde{\phi}$ , with the source being the divergence of the product of  $\alpha^\dagger$  with the pressure gradient. It is clear that the source term in Eq. 4 is nonzero only when spatial derivatives of  $\alpha^\dagger$  or  $p$  are present.

In the problem discussed here, the experimental arrangement is considered to be a pair of parallel plates separated a distance  $h$  with the ultrasound propagating perpendicularly to planes of the electrodes. The

mathematical problem of determination of the potential distribution in the body is simplified if both electrodes are at zero potential, or if the plates are floating and acquire a potential as a result of the time varying polarization generated by the object. The former case is considered as a first approach, as the potential between the plates can be made small by connecting them to the input of a low input impedance amplifier, which permits detection of a current. The potential  $\tilde{\phi}$  for all points within the body can then be determined using the Green's function solution to Poisson's equation. The result of the calculation<sup>7</sup> gives the frequency domain potential as

$$\tilde{\phi}(\mathbf{x}) = \int_{V'} G_D(\mathbf{x}, \mathbf{x}') \nabla' \cdot [\alpha^\dagger(\mathbf{x}', \omega) \nabla' \tilde{p}(\mathbf{x}')] dV', \quad (5)$$

where  $G_D(\mathbf{x}, \mathbf{x}')$  is the Green's function.

A current can be generated in the external circuit as a result of two different mechanisms—a time varying polarization induced by the ultrasound in the dielectric, or by conduction of an electric current induced by the polarization. For the former mechanism, variation in the displacement vector  $\mathbf{D}$  gives a current given by  $\mathbf{J}_P = \partial \mathbf{D} / \partial t$ . Since the potential is known throughout the body from Eq. 5, the electric field can be found from the space gradient of  $\tilde{\phi}(\mathbf{x})$  which, together with the relation for a linear dielectric  $\mathbf{D} = \epsilon \mathbf{E}$ , gives the polarization current as  $\mathbf{J}_P(\mathbf{x}) = -\epsilon \frac{\partial}{\partial t} \nabla \tilde{\phi}(\mathbf{x})$ .

For the mechanism of current generation through ordinary conduction, free charge carriers follow the electric field lines to give a current  $\mathbf{J}_F$ , determined by the conductivity of the body through the relation  $\mathbf{J}_F = \sigma \mathbf{E}$ . Thus the current density at any point in space within the body can be written  $\mathbf{J}_F(\mathbf{x}) = -\sigma \nabla \tilde{\phi}(\mathbf{x})$ . The total current  $I$  must be the sum of the components of the two current densities flowing in a direction perpendicular to the electrodes, integrated over the surface of one of the electrodes  $S$ . Hence the current in the external circuit is

$$I = \frac{(\sigma + i\omega\epsilon)}{2\pi^2 h} \iint_{S'} dx dy \int_{V'} \frac{\partial}{\partial z} G_D(\mathbf{x}, \mathbf{x}')|_{z=0} \nabla' \cdot [\alpha^\dagger(\mathbf{x}', \omega) \nabla' \tilde{p}(\mathbf{x}')] dV', \quad (6)$$

evaluation of which<sup>7</sup> gives

$$I = \frac{i\omega}{h} \int_V \alpha(\mathbf{x}, \omega) \frac{\partial}{\partial z} p(\mathbf{x}) dx dy dz, \quad (7)$$

Equation 7 can be put in a simple form by using the equations of linear acoustics for an inviscid fluid to give

$$I = -\frac{i\rho\omega^3}{h} \int_V \alpha(\mathbf{x}, \omega) u(\mathbf{x}) dx dy dz. \quad (8)$$

The recorded voltage signal from an arbitrary body is thus seen to be an integral of the displacement of the ultrasonic wave  $u(\mathbf{x})$  integrated over  $\alpha(\mathbf{x}, \omega)$ , the function describing the active region of the body containing the colloidal object. The interpretation of the signal generation from Eq. 8 is exactly as described qualitatively above in the Introduction: the periodic displacement of the fluid with respect to the particles generates a signal proportional to the integral of the amplitude of the acoustic displacement over the active colloidal region. It is noteworthy that depending on the dimensions of the  $\alpha(\mathbf{x}, \omega)$  relative to the acoustic wavelength, the signal can integrate to zero.

Consider a hypothetical single cycle of an acoustic wave as shown in Fig. 1 where the propagation direction is in the direction of the arrow at the top of the wave, and the displacements within the wave are indicated by the two smaller arrows. The wave travels from an inert region to a colloidal layer that is equipped with a grounded electrode on the left, and a second, output electrode on the right. For a negatively charged colloid dense compared with the surrounding fluid with a positive counter charge, the first encounter with the wave with the colloid is, as shown in the top of Fig 1, only with the left-going part of the wave. Thus, the dipole is formed as shown in the ellipse and the potential at the output electrode is negative relative to ground. When the wave is wholly within the colloidal region, oppositely directed dipoles are formed for each half cycle of the wave that add to zero so that no voltage appears at the output electrode. Finally, as shown at the bottom of Fig. 1, as the wave exits the colloidal region, the only part of the wave lying within the colloidal region is right-going so that the fluid is displaced to the right relative to the particles hence generating a positive voltage

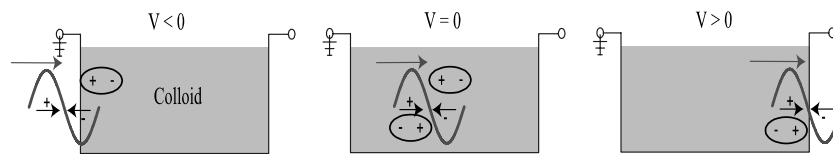


**Figure 1.** Diagram of a single cycle of a sine wave entering a colloidal layer. The layer is equipped with electrodes, the left one being kept at ground potential.

at the electrode. It thus follows that for any burst of ultrasound short compared with the dimensions of the layer that two bursts of voltage will be produced, and that a recording of the arrival time of the first voltage burst, and time difference between the pulses, together with a knowledge of the sound speed in the layer can be used to determine the thickness and the location of the layer

It is not difficult to imagine continuous radiation directed at the layer, or at least a burst of ultrasound long compared with the dimensions of the colloidal layer, where an even number of half cycles of the wave lies within the layer giving zero for the output voltage. With a small change in the frequency of the sound wave, an odd number of half cycles would extend over the length of the layer giving a maximum signal value. By measuring the differences in the frequencies at the maxima and minima in the vibration potential signal, the thickness of the layer can be deduced.

## 2.2. Experiments

Experiments were carried out using the apparatus shown in Fig. 2 which consisted of two acoustic delay lines at either end of the object, a translation stage for rastering the transducer across the object, and a pair of electrodes. A saline solution in contact with the walls of the cell formed one of the electrodes. The saline solution permitted translation of the transducer in a plane across the top of the cell and provided a delay line for the ultrasound as well. The second electrode was made of thin copper tape placed below an agarose delay line at the bottom of the cell. The output from the electrodes was fed to a preamplifier and then to a high frequency lock-in amplifier which permitted determination of either the in-phase or quadrature components of the vibration potential signal. Typically, a 1 MHz transducer driven by a power amplifier was used to generate the ultrasound.

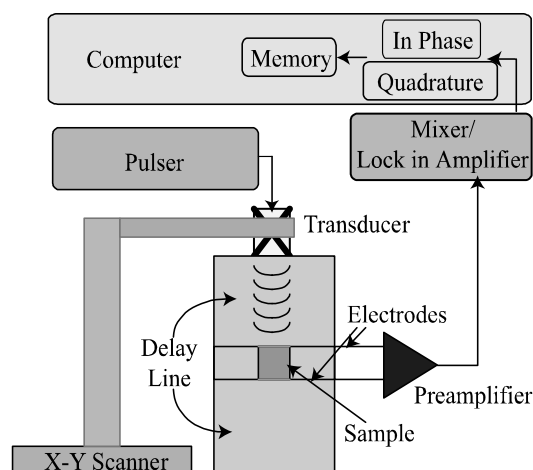


**Figure 2.** Diagram of the apparatus

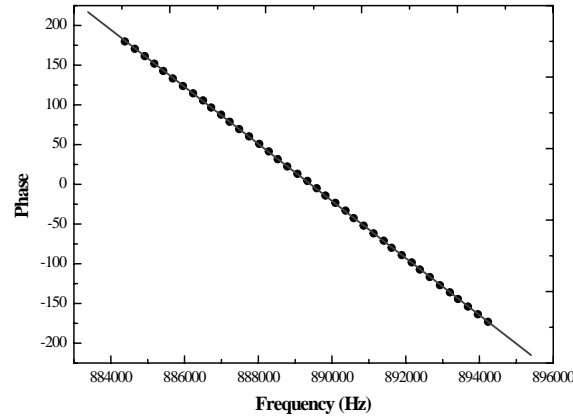


**Figure 3.** Phase versus frequency for a single thin layer of colloid that approximates a delta function in space.

Figure 3 shows the results of an experiment with a thin layer of colloidal silica 0.05 mm thick, where the frequency of the transducer was swept. With the disk modelled as a delta function in space, Eq. 8 gives the current asproportional to  $i\rho\omega^3\alpha_0 u(z-z_0)/h$ , where  $\alpha_0$  is the space independent part of  $\alpha(\mathbf{x},\omega)$  from Eq. 2. The phase of the detected signal recorded by the lock-in amplifier is thus given by  $\omega z_0/c$ , from which it is possible to determine the distance between the layer and the transducer. The vibration potential measurements give  $z_0 = 149\text{ mm}$  in excellent agreement with the measured value of  $150\text{ mm}$ .

An example of the use of Eq. 8 to calculate vibration potentials from simple objects, but with arbitrary incident ultrasonic waveforms is shown in Fig. 4. The incident wave on the layer is an amplitude, modulated sinusoidal function, formed from a radio frequency sine wave with a frequency of 986.5 kHz multiplied by a low frequency sine wave to give an amplitude modulated driving signal to the transducer. The form of the voltage burst from a single layer of colloidal silica of thickness 25.4 mm shown in Fig. 4, gives excellent agreement with the predictions of Eq. 8

An example of the use of rastering the transducer across the sample while at the same time recording the

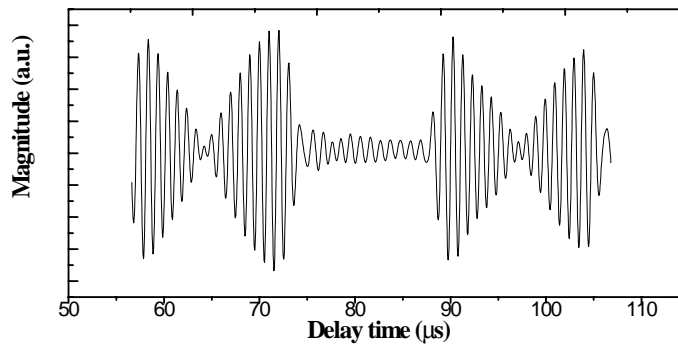


**Figure 4.** Vibration potential waveform produced from an amplituded modulated radio frequency wave.



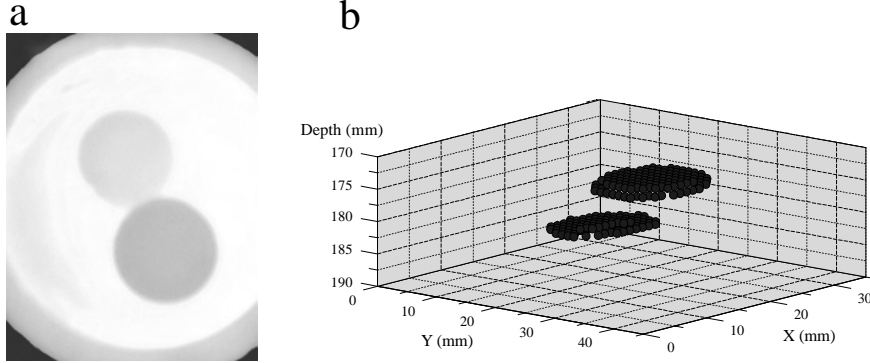


**Figure 5.** (a) Photograph and (b) vibration potential image of a pair of silica colloid disks cast in a block of agarose.

time of arrival of the vibration potential signal is shown in Fig. 5. A phantom of thin silica colloid disks was cast in agarose with the two disks at different elevations in the  $z$  direction, but displaced in the  $xy$  plane as shown in Fig. 5(a). The time of arrival of the vibration potential signal was recorded at each pixel in the  $xy$  plane as a focused transducer was scanned across the phantom. By setting a level for discriminating against noise, a baseline of zero was created in the image as shown in Fig. 5(b).

### 3. ACOUSTICALLY MODULATED X-RAY PHASE CONTRAST IMAGING

#### 3.1. Phase contrast imaging

The wave amplitude  $f(x)$  (in one dimension) from an x-ray plane wave source passing through an object whose phase and absorption are described by a transmission function  $q(x)$  is found from classical optics as

$$f(x) = \left( \frac{i}{z\lambda} \right)^{\frac{1}{2}} e^{-ikz} \int q(X) e^{i\frac{k(x-X)^2}{2z}} dX \quad (9)$$

where  $\lambda$  is the wavelength of the x-radiation,  $k$  is the wave number, and  $z$  is the object to image distance. The intensity of wave at the image plane is given by

$$I(x) = |f(x)|^2.$$

The transmission function can be written for an arbitrary object as

$$q(x) = \exp[i\phi(x) - \mu(x)]$$

which takes into account phase changes through the function  $\phi(x)$  and absorption through another function  $\mu(x)$ . By considering a weak phase object with no absorption, it is possible to determine the intensity for small values of  $(\lambda z)^{1/2} u$  where  $u$  is the spatial frequency in the object to be<sup>8</sup>

$$I(x) = 1 + \frac{\lambda z}{2\pi} \phi''(x), \quad (10)$$

where  $\phi''(x)$  is the second space derivative of the phase given to the x-radiation as it passes through the object. It can also be shown that where there are only density changes the intensity is given by

$$I(x) = 1 + \frac{\lambda^2}{2\pi} r_e \rho''(x), \quad (11)$$

where  $r_e$  is the classical electron radius and  $\rho''(x)$  is the second derivative of the projected charge density.<sup>10</sup> A similar expression follows for the intensity at the image plane for a point source of x-radiation.<sup>10</sup>

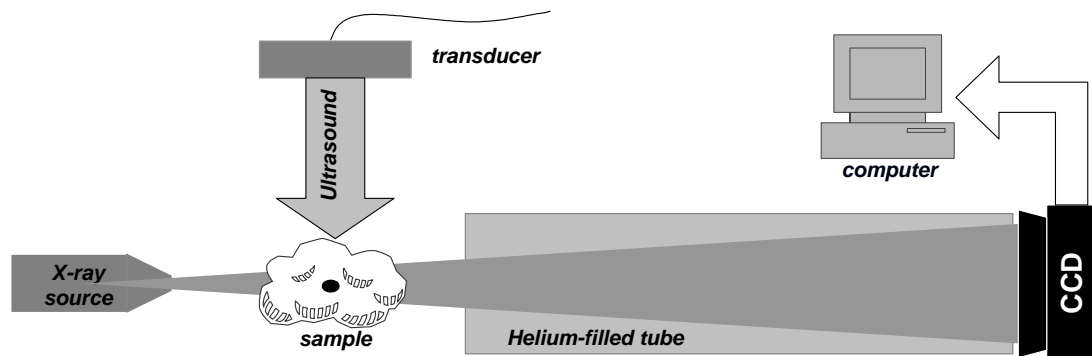


**Figure 6.** Diagram of the experimental apparatus for recording acoustically modulated x-ray phase contrast images.

The interpretation of Eq. 10 is that the contrast seen in the image is proportional to the second derivative of the phase function that describes the object, and that the contrast in the image increases with the wavelength of the x-radiation and the distance from the object to the image plane. It is to be noted that the result given by Eq. 10 is valid only for spatially coherent beams of x-radiation. In a typical medical x-ray apparatus, the beam emerging from the x-ray source does not have the spatial coherence to reveal the features given by Eq. 10; the phase contrast part of the image is essentially averaged out by the large source diameter typical of contemporary x-ray tubes. Generally, a synchrotron or a microfocus x-ray tube must be used to produce phase contrast images.<sup>12</sup> For objects having densities different from that of the surrounding material in the body, the phase contrast component of the x-ray image appears as a sharp fringe at the edge of the object.

### 3.2. Experiments

The method employed here is to use the radiation pressure from a beam of ultrasound to move objects within the body of interest and to record the motion by taking two x-ray images, one with the ultrasound present and one without the ultrasound. The motion recorded in the image is quite small, and cannot be discerned by looking at the two images, however, if the images are subtracted, then the motion becomes apparent for movements that

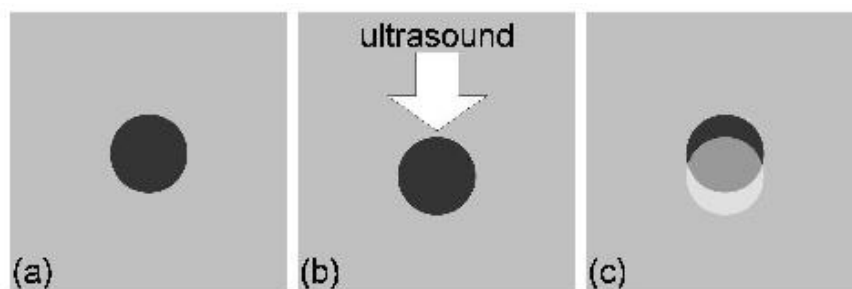


**Figure 7.** Schematic diagram of the subtraction process. The image in (a) is taken without ultrasound. The image in (b) is taken with the ultrasound beam on producing a displacement of the object. The subtracted image shown in (c) has much of the absorption component of the image is eliminated leaving primarily the phase contrast component.

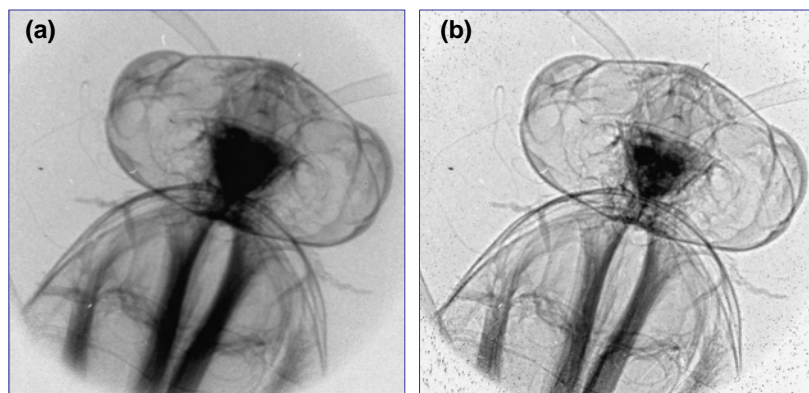


**Figure 8.** Conventional phase contrast image of an insect taken with (a) a source diameter of  $63\ \mu\text{m}$ , and (b) with a source diameter of  $25\ \mu\text{m}$ .

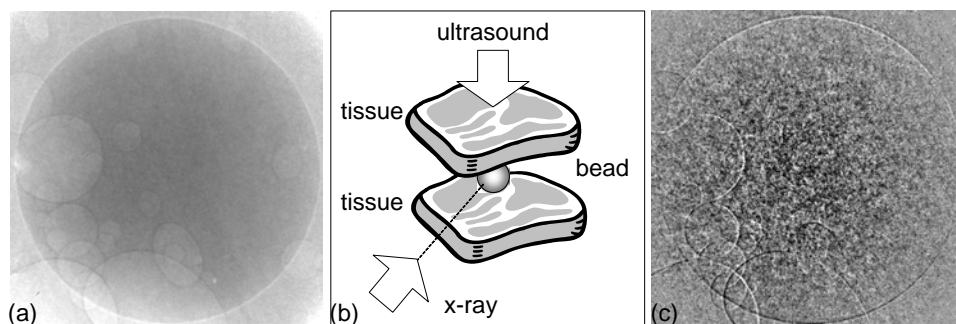


**Figure 9.** (a) Conventional phase contrast image of a teflon sphere in chicken muscle tissue. (b) Schematic diagram of the geometry for irradiation of the phantom with ultrasound and x-radiation. (c) Subtracted image.

are large enough to be resolved in the x-ray image. The method is related to what is sometimes referred to as "remote palpation",<sup>11</sup> which refers to the use of ultrasound to move objects within a body and to probe the movement with conventional ultrasound.

The apparatus for the experiments, shown in Fig. 6, consists of a microfocus x-ray tube, a CCD camera equipped with a phosphor screen, a computer for recording the images, and a conventional pulsed ultrasound source operating at 1 MHz. A *He* filled tube is used to reduce the scattering of the x-rays after passing through the sample. The subtraction process is shown schematically in Fig. 7. It is apparent that image subtraction gives the first space derivative of the phase contrast image for small values of the acoustic displacement.

A conventional phase contrast image of an insect (in air) is shown in Fig. 8. The two images were taken with different tube currents, which has the primary effect of changing the source diameter of the microfocus tube. The image with the most pronounced phase contrast, (b) in Fig. 8, was taken with the smallest source size.

The effect of ultrasonic position modulation is shown in Fig. 9 for a Teflon sphere imbedded in poultry muscle tissue. The effect of the ultrasonic position modulation is to act as a contrast agent for the phase contrast component of the x-ray image. Most of the absorption component of the image is removed while the boundary of the sphere is highlighted. It is also of note that the subtraction process has a vector character—the top and bottom of the sphere are strongly outlined while the left and right hand sides of the sphere are barely visible.

#### 4. SUMMARY

For vibration potential imaging, Eqs. 7 and 8 give the fundamental expressions for the current in a circuit generated by a colloidal or ionic object. The vibration potential signal for an object of any geometry can be determined using either of these two equations. It, of course, is possible to carry out tomography using the vibration potential by rotating the object and acquiring images. Inversion of vibration potential data is far simpler than x-ray tomographic data since the expression in Eq. 7 for a plane travelling wave is just the Fourier transform of  $\alpha(\mathbf{x}, \omega)$ —its inversion is trivial.

The effect of ultrasonic radiation pressure on phase contrast imaging is to highlight the phase contrast in the image and to subtract out the absorptive contrast. The radiation pressure can be said to act as a kind of contrast agent for the x-ray image. The utility of the method is believed to be in its ability to simplify x-ray images and to enhance the features of tumors which can be expected to move as a unit in response to acoustic radiation pressure.

#### Acknowledgment

ACB, CJC, TJH, SW, VG, and GJD were supported by the US Army Medical Research and Materiel Command under Grant DAMD17-02-1-0307; CRP was supported under Grant W81XWH-04-1-0481. Opinions, interpretations, conclusions, and recommendations are those of the authors and are not necessarily endorsed by the US Army.

#### REFERENCES

1. P. J. Debye, "A Method for Determination of the Mass of Electrolytic Ions", *Journal of Chem. Phys.*, **1**, 13 (1956)
2. R. J. Hunter, "Recent Developments in the Electroacoustic Characterization of Colloidal Suspensions and Emulsions", *Colloids and Surfaces* 1998, 141, 37
3. R. Zana and E. Yeager. In *Modern Aspects of Electrochemistry*; J. O. Bockris, B. E. Conway, and R. E. White, eds. (Plenum, New York, 1982)
4. A. S. Dukhin and P. J. Goetz, *Colloids and Surfaces A*, 192, 267 (2001).
5. A. C. Beveridge, S. Wang, and G. J. Diebold, "Imaging based on the Ultrasonic Vibration Potential" *Appl. Phys. Lett.* 85, 5466 (2004)
6. R. W. J. O'Brien, "Electro-acoustic Effects in a Dilute Suspension of Spherical Particles", *Fluid Mech.* 190, 71 (1988)
7. V. Gusev and G. Diebold, "Imaging with the Ultrasonic Vibration Potential: A Theory for Current Generation", (*Ultrasound. in Med. and Biol.*, in press)
8. J. M. Cowley, *Diffraction Physics* (North Holland, Amsterdam, 1995)
9. A. Pogany, D. Gao, and S. W. Wilkins, "Contrast and Resolution in Imaging with a Microfocus X-ray Source", *Rev. Sci. Instrum.* 68, 2774 (1997)
10. A. Pogany, D. Gao, and S. Wilkins, "Contrast and Resolution in Imaging with a Microfocus X-ray Source", *Rev. Sci. Instrum.* 86, 2774 (1997)
11. K. Nightingale, M. Soo, R. Nightingale, R. Bentley, D. Stutz, M. Palmeri, J. Dahl, and G. Trahey, "Acoustic Radiation Force Impulse Imaging: Remote Palpation of the Mechanical Properties of Tissue" *Proc. IEEE Ultrasonics Symp.* 2002, 1821
12. S. W. Wilkins, T. E. Gureyev, D. Gao, A. Pogany, and A. W. Stevenson, "Phase-contrast Imaging using Polychromatic Hard X-rays" *Nature* 384, 335 (1996)

# Photothermal Modulation of X-ray Phase Contrast Images

Christopher M. Laperle<sup>a</sup>, Guohua Cao<sup>a</sup>, Stephan Gehring<sup>b</sup>, Jack Wands<sup>b</sup>, Cristoph Rose-Petruck<sup>a</sup>, and Gerald J. Diebold<sup>a</sup>

<sup>a</sup> Brown University, Chemistry Department, Providence, RI, 02912

<sup>b</sup>Brown University Medical School, Liver Research Center , Providence, RI, 02912

## ABSTRACT

The in-line x-ray phase-contrast method relies on changes in index of refraction within a body to produce image contrast.. In soft tissue, index of refraction variations arise from density changes so that phase contrast imaging provides a map of density gradients within a body. In principle, the use of an intense, short pulse laser beam that is differentially absorbed by an object within body relative to its surroundings will produce a thermal wave with an associated density change. Experiments are described where a pulsed Nd:YAG laser is synchronized to an image intensifier to record the effects of the energy deposited by the laser.

**Keywords:** X-ray phase contrast, laser

## 1. PHOTOTHERMAL MODULATION OF X-RAY PHASE CONTRAST IMAGES

Although contrast in an x-ray phase contrast image has components of both absorption and refraction, the salient feature of the method, insofar as tissue imaging is concerned, is the highlighting of the perimeters of objects which have densities that differ from their surroundings. A typical soft tissue image produced using the in-line geometry<sup>1,2,3</sup> shows the absorption contrast seen in a conventional x-ray image, but with an enhancement of the boundaries of objects of varying densities with dark and light fringes. In both a conventional x-ray imaging instrument and an in-line phase contrast apparatus the body of interest is interposed between the x-ray source and a detector located at the image plane, which may be film or a more contemporary recording device such as a CCD camera or thin film transistor array. The important difference between the two imaging modalities is that a spatially coherent source of x-radiation is employed in phase contrast imaging. To date, synchrotron x-ray sources and microfocus x-ray tubes have provided the x-ray beams with spatial coherence sufficient to give phase contrast features in the image. It is of note that phase contrast effects are produced in conventional absorption radiography, but owing to the comparatively large size and the resulting low degree of spatial coherence provided by a conventional x-ray tube, an averaging of the phase contrast features in the image takes place that renders them essentially invisible.

The qualitative features of in-line, phase contrast imaging image can be found in Ref.<sup>3</sup> which gives the x-ray intensity  $I(x)$  from a weak phase object in one dimension produced from a parallel radiation beam as

$$I(x) = 1 + \frac{\lambda z}{2\pi} \frac{d^2}{dx^2} \phi(x), \quad (1)$$

where  $z$  is the object to image distance  $\lambda$  is the wavelength of the radiation, and  $\phi(x)$  is the phase change undergone by the radiation in traversing the contrast in the image. The most surprising feature of the method is that it is insensitive to the radiation wavelength, which appears only as a multiplicative factor in Eq. 1. The appearance of the second space derivative of the phase as the determinant of contrast gives the images a sensitivity to phase variations, which, in soft tissue, amounts to production of outlines of objects having differing densities from their surroundings. A phase contrast image of is proportional both to  $z$ , and to the second space derivative of the phase function,  $\phi''(x)$ . Another important feature of the phase contrast method,<sup>1</sup> which is evidenced by the form of Eq. 1, is the weak dependence of image contrast on wavelength. This implies images

---

Further author information: (Send correspondence to G.J.D.)  
G.J.D.: E-mail:gerald\_diebold@brown.edu, Telephone: 1 401 863 3169

**Figure 1.** Schematic diagram for x-ray phase contrast imaging. The source is taken to be a perfect point source in the calculation of the one-dimensional image.

can be made using polychromatic x-rays. It can also be shown that where there are only density changes, the intensity at the image plane is given by

$$I(x) = 1 + \frac{\lambda^2}{2\pi} r_e \rho''(x), \quad (2)$$

where  $r_e$  is the classical electron radius and  $\rho''(x)$  is the second derivative of the projected charge density.<sup>?</sup>

With the method we present here, maximum phase contrast effects in the subtracted image are found when the displacement of the object of interest is approximately equal to the width of a single x-ray fringe in the image. The rudiments of the theory and a sampling of experimental results are presented.

### 1.1. Theory of phase contrast imaging

The transverse coherence length  $d_\perp$  of radiation with a wavelength  $\lambda$  generated by a near point source of radiation with a source diameter  $\sigma$  recorded at a distance  $l$  from the source is given by

$$d_\perp = \frac{\lambda l}{\sigma}.$$

For a microfocus x-ray source it is essential to design the x-ray tube with a small spot diameter in order to maximize the degree of lateral coherence. Also, the resolution in the CCD camera must be commensurate with the dimensions of the interference fringes, which constitutes a second requirement for observation of phase contrast in the image, but which can be overcome using high resolution image recording devices.

For x-rays, the complex index of refraction  $n$  can be written

$$n = 1 - \delta + i\beta,$$

where  $\delta$  is the real part of the index of refraction that accounts for phase contrast in the image, and  $\beta$  is the imaginary component of the index of refraction that governs absorption. It can be shown that both  $\delta$  and  $\beta$  are proportional to the material density. The theory of phase contrast imaging is based on the Fresnell-Kirchhoff integral formulation of wave propagation.<sup>4</sup> In one dimension, the intensity  $I(x)$  recorded at the image plane is given by the square of the absolute value of the electric field  $f(x)$ , that is,

$$I(x) = |f(x)|^2. \quad (3)$$

The electric field for a point source placed at the origin is given by

$$f(x) = \left( \frac{i}{\lambda R_1 R_2} \right)^{1/2} e^{-ikR_2} \int e^{-ik\frac{X}{2R_1}} q(X) e^{-ik\frac{(x-X)^2}{2R_2}} dX$$

**Figure 2.** X-ray phase contrast image of a nylon wire

where, as shown in Fig. 1,  $R_1$  is the source to object distance,  $R_2$  is the object to image distance,  $k$  is the wavenumber of the radiation, and  $q(X)$  is the phase function at the plane of the object. The phase function includes the effects of both phase changes as well as absorption, and can be expressed as

$$q(\xi) = e^{i\phi(\xi) - \mu(\xi)}$$

where  $\phi$  is the phase change undergone by the x-radiation as it passes through the body, and  $\mu$  is the absorption. The phase, in turn, is related to the real part of the refractive index through

$$\phi(z) = -k \int_z \delta(z') dz',$$

where the integration is along the path of the x-ray beam which is arbitrarily taken as the  $z$  direction. By manipulation of Eq. 3, the intensity, written without factors common to both the modulated and constant terms  $\hat{I}(x)$ , can be written

$$\hat{I}(x) = |1 + A(x)|^2 \quad (4)$$

where

$$A(x) = \sqrt{\frac{i(R_1 + R_2)}{\lambda R_1 R_2}} e^{\frac{ikx^2}{2(R_1 + R_2)}} \int_{-a}^a e^{-ik \left[ \frac{x^2}{2R_1} + \frac{(x-X)^2}{2R_2} \right]} [q(X) - 1] dX.$$

The integration of  $A(x)$  in Eq. 4 is carried out over the object of interest so that the phase function  $q$  is taken to be unity outside the body of interest. In two dimensions, where the phase function  $q(X, Y)$  is taken to be separable as the product of two functions,  $q_x$  and  $q_y$ , the Fresnel integral can be expressed as

$$f(x, y) = \frac{i}{\lambda} \frac{e^{-ik(R_1 + R_2)}}{R_1 R_2} \int e^{-ik \frac{x^2}{2R_1}} e^{-ik \frac{(x-X)^2}{2R_2}} q_x(X) dX \int e^{-ik \frac{y^2}{2R_1}} e^{-ik \frac{(y-Y)^2}{2R_2}} q_y(Y) dY$$

## 1.2. X-ray experiments

The apparatus used in these experiments consists of a microfocus x-ray tube (Oxford, Inc. Model UM-M1), and a liquid nitrogen cooled CCD camera (Roper Scientific, Model 7382-0001) with a pixel size of 19  $\mu\text{m}$ . The CCD viewed a *CsI* fiber optic plate (Hamamatsu Model J6676). The image of a nylon wire shown in Fig. 2, is taken without the application of ultrasound and clearly shows a highlighted interface; the effect of phase interference. The geometrical parameters were  $R_1 = 0.35$  m and  $R_2 = 2.25$  m, so that there is a magnification of 7.4 in the



**Figure 3.** Typical phase contrast intensity pattern for a nylon line calculated from Eq. 4. Absorption was not included in the calculation so the effects of phase contrast alone are shown.

**Figure 4.** X-ray source acceleration versus x-ray spot size.

image. The x-ray source was operated at a voltage 90 kV, and a current of 100  $\mu$ A. The exposure time for the image was 15 s.

A calculation of the phase contrast in the image was carried out using Eq. 4 using a value for  $\delta$  of  $3.276 \times 10^{-8}$  and  $\lambda$  of  $0.138 \times 10^{-10}$  m using the expression

$$\phi(\xi) = -2k\delta\sqrt{a^2 - \xi^2},$$

for the phase function, which describes a cylinder. No account is taken of the polychromaticity of the radiation, which would, to some degree, be expected in an experiment. The results of the calculation are shown in Fig. 3.

With a microfocus x-ray tube, phase contrast becomes more pronounced as the source size is reduced. The data for our source, as approximated with a typical knife-edge procedure is shown in the Figure 4; the source size is clearly a function of tube acceleration voltage. The minimum source diameter, as reported by the manufacturer is  $13\mu m$ .

The effect of source size on the visibility of the interference effects is clear from the following comparison of two images in Figure 5 of a rat liver. Interfacial features, which vary in density, are sharply outlined in the image on the right, which was taken with a source size of  $15\mu m$ ; the same features in the image on the left, taken with a source size of  $63\mu m$ , are less visible.

### 1.2.1. Combination of ultrasonic modulation and x-ray phase contrast imaging

To produce an ultrasonically modulated x-ray phase contrast image, as shown in Fig 6, the ultrasonic radiation is directed perpendicularly to the direction of travel of the x-ray beam. The acoustic radiation was generated

**Figure 5.** Images of a section of a rat liver with large and small x-ray source sizes. The image on the left was taken with an x-ray source size of  $63\ \mu\text{m}$ ; the image on the right was taken with an x-ray source size of  $15\ \mu\text{m}$ .

**Figure 6.** Experimental diagram for the described x-ray experiments. An He atmosphere reduces scatter.

by amplifying a 1.14 MHz sinusoidal wave in a power amplifier (Ritec, Inc. Model GA2500) whose output was fed to a  $\text{LiNbO}_3$  ultrasonic transducer. Experiments were performed to demonstrate ultrasonic modulation of phase contrast images with a tumor phantom.

The images in Fig. 7 show the effect of applying ultrasonic radiation pressure to a Teflon sphere sandwiched between two pieces of poultry muscle tissue. The acoustic radiation consisted of  $15\ \mu\text{s}$  long bursts of radiation applied at a repetition frequency of 133 kHz. The subtracted image on the right shows the highlighted boundary

**Figure 7.** The x-ray phase contrast image on the left was taken prior to the application of ultrasound. The image on the right is the result of subtracting the image with ultrasonic application from the one without.

**Figure 8.** Ultrasonically modulated x-ray phase contrast image of a mouse skin tumor.

of the sphere and elimination of absorption features.

An acoustically modulated phase contrast image of a mouse skin tumor is shown in Fig. 8. The tissue sample is held in place by a thin plastic tube which also serves as a conduit for the ultrasound. The fine features in the subtracted image show how tissue with different elastic moduli move differentially in response to ultrasonic radiation pressure and highlight phase contrast in the image; at the same time, the absorption contrast seen in a conventional phase contrast image almost totally eliminated.

### 1.3. Apparatus and Experiments

## 2. DISCUSSION

### 2.1. X-ray phase contrast imaging with ultrasound

The critical feature of x-ray phase contrast imaging, as applied to soft tissue, is its response to changes in density. Although the sample calculations show characteristic high frequency oscillations at the perimeter of an object whose density differs from that of its surroundings, the experimental images presented here do not appear with such high resolution. The increased intensity at the edges of the nylon wire in the experimental image is a consequence of averaging of the intensity oscillations predicted by theory for a perfect point source over the finite source diameter of the x-ray tube. Despite the averaging, distinct features on a short length scale are clearly evident in the x-ray images.

An important feature of the ultrasonic method discussed here is that the acoustic radiation pressure is directional, that is, it has a vector character. Thus, the subtracted image has a response only in the direction of the ultrasonic radiation force. The combined features of the method described here including high resolution, response to changes in elasticity parameters, and response to rapid variations in density at the edges of objects give acoustically modulated phase contrast imaging some possibility of tumor detection over conventional x-ray mammography.

## 3. ACKNOWLEDGEMENT

The authors, GJD, TJH, GC, SW, CN, and SL, are grateful for the support of this research by the US Army Medical Research and Materiel Command under grant DAMD17-02-1-0307; and GJD and CRP under grant W81XWH-04-1-0481.

## REFERENCES

1. S. W. Wilkins, T. Gureyev, D. Gao, A. Pogany, and A. W. Stevenson, "Phase-contrast imaging using polychromatic hard x-rays," *Nature* **384**, pp. 335–338, 1996.
2. A. Momose, "Demonstration of phase-contrast x-ray computed tomography using an x-ray interferometer," *Instruments & Methods in Physics Research, Section A* **352**, p. 622, 1995.
3. A. Pogany, D. Gao, and S. Wilkins, "Contrast and resolution in imaging with a microfocus x-ray source," *Rev. Sci. Instr.* **68**, pp. 2774–2782, 1997.
4. M. V. Klein, *Optics*, John Wiley & Sons, Inc., 1970.

# Photothermal Modulation of X-ray Phase Contrast Images

Christopher M. Laperle, Guohua Cao, Theron J. Hamilton, Christoph Rose-Petruck, and  
Gerald J. Diebold

Brown University, Chemistry Department, Providence, RI, 02912

## ABSTRACT

The in-line x-ray phase-contrast imaging method relies on changes in index of refraction within a body to produce image contrast. In soft tissue, index of refraction variations arise from density changes so that phase contrast imaging provides a map of density gradients within a body. An intense, short pulse laser beam that is differentially absorbed by an object within a body will produce a thermal wave with an associated density change that propagates outwardly from the interface between the object and the body. Experiments are described where a pulsed Nd:YLF laser is synchronized to an image intensifier to record the effects of the energy deposited by a pulsed laser.

**Keywords:** X-ray phase contrast, laser

## 1. INTRODUCTION

The salient feature of the x-ray phase contrast imaging, insofar as tissue imaging is concerned, is the highlighting of the perimeters of objects which have densities that differ from their surroundings. A typical soft tissue image produced using the in-line geometry<sup>1,2,3</sup> shows the absorption contrast seen in a conventional x-ray image, but with an enhancement of the boundaries of objects of varying densities with dark and light fringes. In both a conventional x-ray imaging instrument and an in-line, phase contrast apparatus the body of interest is interposed between the x-ray source and a detector located at the image plane, which may be film or a more contemporary recording device such as a CCD camera or thin film transistor array. A schematic diagram of the in-line x-ray imaging apparatus is shown in Fig. 1. Note that this arrangement gives a magnification of  $(R_1 + R_2)/R_1$ .

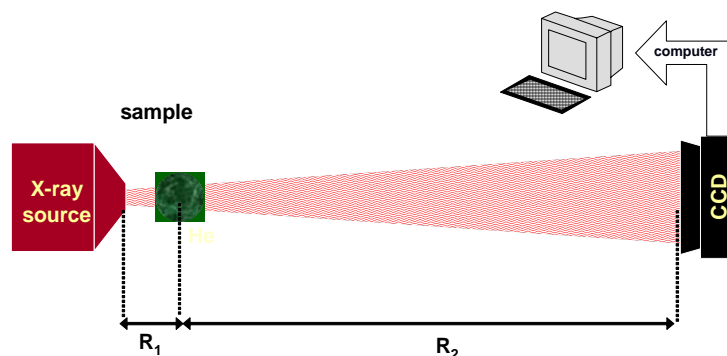


**Figure 1.** Schematic diagram of an in-line, x-ray imaging apparatus. The source-to-object distance is denoted as  $R_1$ ; the object-to-image plane distance is denoted  $R_2$ .

The important difference between the two imaging modalities is that a spatially coherent source of x-radiation is employed in phase contrast imaging. To date, synchrotron x-ray sources and microfocus x-ray tubes have provided x-ray beams with spatial coherence sufficient to give phase contrast features in the image. It is of note that phase contrast effects are produced in conventional absorption radiography, but owing to the comparatively large size and the resulting low degree of spatial coherence provided by a conventional x-ray tube, an averaging of the phase contrast features in the image takes place that renders them essentially invisible.

---

For further information, send correspondence to G.J.D. at Gerald\_Diebold@Brown.edu, Telephone: 401 863 3586

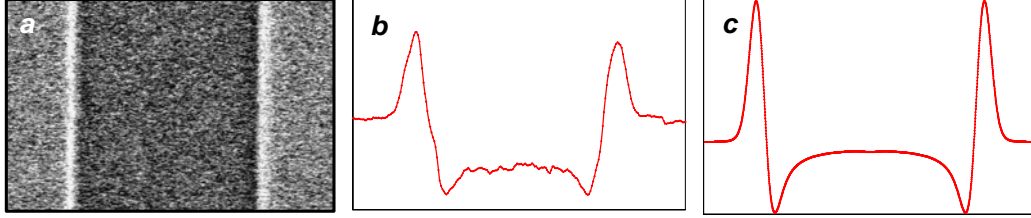


**Figure 2.** (Left) Experimental, x-ray, phase contrast image of a nylon line taken at 90 kV. (Center) Numerical average of the experimental image in the horizontal direction. (Right) Calculated image of the nylon line.

### 1.1. X-ray phase contrast imaging

The qualitative features of in-line, phase contrast imaging image can be found in Ref. 3 which gives the x-ray intensity  $I(x)$  from a weak phase object in one dimension produced from a parallel radiation beam as

$$I(x) = 1 + \frac{\lambda z}{2\pi} \frac{d^2}{dx^2} \phi(x), \quad (1)$$

where  $z$  is the object-to-image distance  $\lambda$  is the wavelength of the radiation, and  $\phi(x)$  is the phase change undergone by the radiation in traversing the object. The most surprising feature of the method is that it is insensitive to the radiation wavelength, which appears only as a multiplicative factor in Eq. 1. The appearance of the second space derivative of the phase as the determinant of contrast gives the images a sensitivity to phase variations, which, in soft tissue, amounts to the formation of outlines of objects having differing densities from their surroundings. The dependence of the contrast on the distance  $z$  according to Eq. 1 would appear to indicate that an arbitrarily large contrast can be obtained by simply increasing  $z$ ; however, this expression was derived under the assumption of a perfect plane wave of x-radiation which accounts for the idealized dependence on this parameter. An experimental phase contrast image of a nylon wire is shown in Fig. 2. In general, the effect of phase contrast is to enhance the absorption contrast since the dark fringe coincides with the more highly absorbing part of the body and the light fringe coincides with the weakly absorbing part of the body.

The problem with conventional x-ray mammography is its limited contrast for detecting the small density changes associated with tumors.<sup>4</sup> The contrast in x-ray mammography is achieved to a large extent by operating the x-ray tube at low voltages so that there is significant absorption of the x-ray beam in its traversal of the breast. As noted in Ref. 4, the demands on this modality for detection of the small density changes characteristic of tumors as well as the fine structure of calcifications while at the same time as delivering a low dose to the patient are severe. Despite the difficulties, though, mammography remains the preferred modality for screening for breast tumors.

### 1.2. Photothermal effects

Laser induced photothermal effects in the visible and near infrared spectral region have been known for some time.<sup>5-7</sup> There are various experimental arrangements for creating and recording the thermal waves, which usually involve measuring the deflection of a low divergence laser beam. One of the simplest experimental arrangements is to use a pulsed or continuous laser to create a thermal wave at the boundary between a transparent and an absorbing medium. The thermal diffusion wave created by absorption of the laser beam propagates away from the interface generating changes in the density of the medium, and consequently its index of refraction. If another laser beam, referred to as the "probe beam" is directed perpendicularly to the direction of the heating beam at a point near the interface, then the probe beam will be deflected in an amount dependent on the density gradient. The common Nd:YAG pulsed laser produces radiation bursts on the duration of 10 ns, which, even in a weak absorber, can give rise to enormous temperature gradients. Elementary calculations show that an 800 nm, 15 ns long laser beam with a fluence of 0.25 mJ/cm<sup>2</sup> directed at the interface between water and blood, considered in a one-dimensional geometry, gives a temperature gradient on the order of 10<sup>6</sup> K/m. Shorter laser

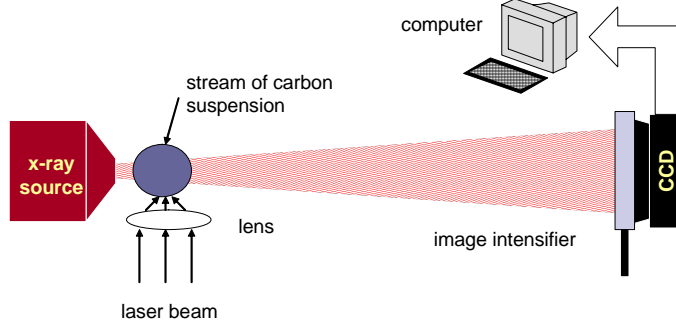


**Figure 3.** Schematic diagram of the apparatus used to record laser modified x-ray images which consists of a microfocus x-ray tube, a gated image intensifier and a CCD camera equipped with a phosphor.. The firing of the laser and the gating of the image intensifier are synchronized with a pulse generator.

pulses, obtained from, for instance, fs lasers which are commercially available, will produce correspondingly higher temperature gradients.

Both a thermal wave and an acoustic wave are launched as a consequence of absorption of a pulsed laser beam. As noted in the theory of the transient grating,<sup>8-10</sup> absorption of pulsed laser radiation generates a thermal wave and an acoustic wave, both of which have associated density change. The former is described by equations that govern the thermal mode of wave motion, and the latter by the acoustic mode.<sup>11</sup> For pulsed laser excitation, the appropriate time scales for detecting the acoustic wave and the thermal wave can be different as the acoustic wave is a propagational wave, and the thermal wave is diffusive. The important point though is that it is possible to modify an image taken at any wavelength by inducing density changes through any means whatever, since the index of refraction is dependent on density.

## 2. EXPERIMENTS

For applications to biology and medicine, the modification of x-ray images through absorption of laser energy has the possibility of taking advantage of the well-known, high optical contrast of blood in the near infrared<sup>12, 13</sup> to provide differential optical absorption and hence the generation of thermal and acoustic waves. In fact, it is this optical contrast on which the increasingly promising method of photoacoustic imaging is based.<sup>12, 13</sup> The object of the experiments reported here is to explore laser modification of x-ray images. In particular, the method of in-line phase contrast imaging has been selected owing to its high resolution and contrast.

The imaging apparatus used in these experiments, as shown in Fig. 3 consists of a microfocus x-ray tube (Oxford, Inc. Model UM-M1) and a liquid nitrogen cooled CCD camera (Roper Scientific, Model 7382-0001) with a pixel size of 19  $\mu\text{m}$ . The CCD camera views a *CsI* fiber optic plate (Hamamatsu Model J6676). The geometrical parameters used in these experiments were  $R_1 = 0.11\text{ m}$  and  $R_2 = 1.0\text{ m}$ , so that there is a magnification of 10 in the image. The image intensifier (Photek Ltd., Model MCP 125 equipped with a GM10-50 gate unit) used a P47 X-ray scintillator. A Nd:YLF laser (Photonics Industries, Model GM-30-527) produced 532 nm radiation at 2 kHz with a pulse duration of 200 ns.

Experiments were carried out by focusing the laser beam onto an approximately 1 mm diameter stream of a carbon suspension in water using a lens with a 40 cm focal length. The image intensifier was gated on for 100  $\mu\text{s}$  at the time of the firing of the laser. The image shown in Fig. 4 was acquired over 100 firings of the laser for a total image acquisition time of 500 ms with the laser operating at 10 mJ per pulse..

## 3. DISCUSSION

Experiments with photothermal modulation of x-ray images of a flowing carbon suspension clearly show the effects of absorption of pulsed laser radiation at the point of focusing at (a) in Fig. 4. Unfortunately, the laser

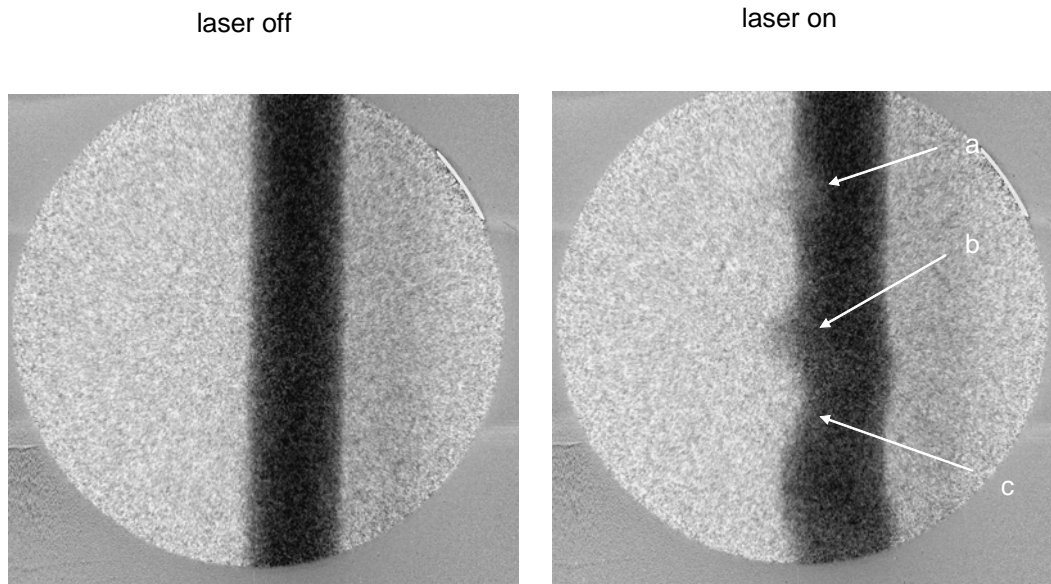


**Figure 4.** (Left) X-ray image of a flowing stream of an aqueous carbon suspension. (Right) X-ray image of the carbon suspension synchronized with the firing of the laser. The point marked (a) corresponds to the position where the laser beam is focused.

fluence required to produce the photothermally modified images is quite high so that even a visually discernable modification of the carbon suspension stream is evident. It became clear in the experiments that the resolution of the apparatus is not adequate to detect photothermal density modification at low fluences. In fact, a comparison of the images in Figs 2 and 4 indicate that there is very little phase contrast if the latter, which can be attributed to the poor resolution of the image intensifier and the long integration time that is a consequence of using a continuous x-ray source in an arrangement where the duty cycle of the gating is small. High resolution imaging requires that any mechanical drift in generation of the image be smaller than the desired resolution in the image. Despite the shortcomings of the apparatus, the modification of the stream at points (b) and (c) show the power of the method, in general, for time resolved imaging.

A rigorous test of the utility of photothermal modulation of x-ray imaging would appear to require the use of an intense pulsed x-ray source that could be synchronized with the laser. The overall ability of the imaging system to record phase contrast would clearly be a requirement for such an experiment as resolution is paramount. For the technique, in general, there is a trade off in the resolution of the imaging system and the time gating of the detector: an image recorded at a short time after the firing of the laser will be modified by large density gradients but which will be highly localized in space requiring high resolution of the imaging apparatus, whereas images recorded on a longer time scale will be modified by smaller density gradients, but which extend over a larger spatial extent relaxing the requirement for resolution. Given the experimental results reported here, it appears that the use of a synchrotron x-ray source with its short pulse length, high repetition rate, and high brightness, synchronized to a pulsed laser would provide the optimum experimental configuration for observing photothermal modulation of biological samples at low laser fluences.

#### 4. ACKNOWLEDGEMENT

The authors, GJD, TJH, and GC are grateful for the support of this research by the US Army Medical Research and Materiel Command under grant DAMD17-02-1-0307, GJD and CRP under grant W81XWH-04-1-0481; CL through an NIH Ruth L. Kirschstein fellowship; and CRP under NSF grant CHE-0405599..



## REFERENCES

1. S. W. Wilkins, T. Gureyev, D. Gao, A. Pogany, and A. W. Stevenson, "Phase-contrast imaging using polychromatic hard x-rays," *Nature* **384**, pp. 335–338, 1996.
2. A. Momose *Instruments & Methods in Physics Research, Section A* **352**, p. 622, 1995.
3. A. Pogany, D. Gao, and S. Wilkins, "Contrast and resolution in imaging with a microfocus x-ray source," *Rev. Sci. Instr.* **68**, pp. 2774–2782, 1997.
4. J. Bushberg, J. Seibert, and E. Leidholdt Jr, *The Essential Physics of Medical Imaging*, Williams and Wilkins, Baltimore, 1994.
5. A. Mandelis, ed., *Progress in Photothermal and Photoacoustic Science and Technology*, vol. I, Elsevier, New York, 1992.
6. A. Mandelis, ed., *Photoacoustic and Thermal Wave Phenomena in Semiconductors*, North Holland, New York, 1987.
7. J. A. Sell, ed., *Photothermal Investigations fo Solids and Fluids*, Academic Press, Boston, 1989.
8. H. J. Eichler, P. Gunter, and K. W. Pohl, *Laser-Induced Dynamic Gratings*, Springer, Berlin, 1985.
9. T. Sun, J. Morais, G. J. Diebold, and M. B. Zimmt, "Investigation of viscosity and heat conduction effects on the evolution of a transient picosecond photoacoustic grating," *J. Chem. Phys* **97**, pp. 9324–9334, 1992.
10. H. X. Chen and G. J. Diebold, "Production of the photoacoutic effect and transient gratings by molecular volume changes," *J. Chem. Phys* **104**, pp. 6730–6741, 1996.
11. P. M. Morse and K. U. Ingard, *Theoretical Acoustics*, Harwood Academic, 1991.
12. S. A. Ermilov, A. Conjusteau, K. Mehta, R. Lacewell, P. M. Hendricks, and A. Oraevsky, p. 608601. Biomedical Optoacoustics, SPIE, 2006.
13. J. T. Oh, M. L. Li, X. Xie, G. Stoica, and L. V. Wang, p. 60860C. Biomedical Optoacoustics, SPIE, 2006.

## The theory of ultrasonic vibration potential imaging

A.C. Beveridge<sup>1</sup>, S. Wang<sup>1</sup>, V.E. Gusev<sup>2</sup> and G.J. Diebold<sup>1</sup>

<sup>1</sup>*Department of Chemistry, Brown University, Providence, RI 02912, USA*

<sup>2</sup>*Université du Maine, Av. Sessiaen, 72085 Le Mans Cedex 09, France*

**Abstract.** The ultrasonic vibration potential refers to the production of a time varying voltage when ultrasound passes through a colloidal or ionic solution. The vibration potential can be used as an imaging method for soft tissue by recording its phase, time of arrival, and magnitude relative to the launching of a burst of ultrasound. A theory of the effect can be found from Maxwell's equations. Experimental results demonstrating the imaging method are shown for bodies with simple geometries.

### 1. INTRODUCTION

The generation of a voltage, known as the ultrasonic vibration potential, by the passage of ultrasound through a colloidal or ionic suspension is an electrokinetic effect that arises from charge separation induced by the sound wave. In either ionic or colloidal solutions, the phenomenon arises from disturbance of the equilibrium distribution of charge in solution. In the case of a colloid, particles suspended within solution are charged as a result of chemical groups attached to the particles. There must therefore be a counter charge in the fluid to give the solution overall charge neutrality. In almost every case the density of the colloidal particles and the surrounding fluid differ from each other, so that when sound passes through a suspension, the motions of the particles and fluid differ owing to their different inertias. A dense particle has a smaller amplitude motion than the fluid, causing the fluid to flow back and forth across the particle surface on alternating cycles of the acoustic wave. When the fluid flows over the particles, it carries the counter charge in the fluid resulting in a distortion of the normally spherical distribution of charge around the particles. The result is the production of a dipole at the site of each colloidal particle. For ionic solutions, a different mass of the anion and cation can result in a corresponding charge separation in solution that gives rise to a macroscopic voltage. The vibration potential was originally predicted by Debye [1] for ionic solutions. Following its observation in ionic solutions, it was subsequently found in colloidal suspensions, which generally give larger amplitude vibration potentials than ionic solutions. The theory of the effect has been reviewed by several authors [2–4].

The vibration potential can be used as a means of imaging colloidal or ionic species within a body that is a weak conductor [5]. Here, we outline the problem of determining the current in a pair of electrodes from a colloidal object with an arbitrary shape imbedded in an inert medium irradiated with ultrasound. There are two mechanisms for producing the current, one proportional to the time derivative of the electric displacement produced by the object, and a second where an ion current is generated by the electric field distribution produced by the ultrasound irradiated object. An experimental demonstration of the method is reported for colloidal objects.

### 2. THE DIFFERENTIAL EQUATION FOR THE POTENTIAL

The first step in the theory for imaging is to determine the polarization that the colloidal object produces and to incorporate this polarization into Maxwell's equations. The most direct route is to determine the potential in the body containing the object, from which the electric field and displacement can be found. Second, a frequency domain equivalent to this expression is found. The solution to the frequency domain equation for the potential is found by using the Green's function method for a pair of electrodes in contact with the body. Once the Green's function is known, a potential can be determined for an

object with an arbitrary shape. Next, the electric field and electric displacement are found, from which the current in the electrodes is determined.

The electric field  $\mathbf{E}$  produced across a region of colloid by a pressure  $p$ , has been given by O'Brien [6] as

$$\mathbf{E} = \frac{f \Delta \rho_m \mu_E}{\rho_m \sigma^*} \nabla p, \quad (2.1)$$

where  $f$  is the volume fraction of colloidal particles in the fluid,  $\mu_E$  is the electrophoretic mobility of the particles,  $\rho_m$  is the mass density of the suspension, and  $\Delta \rho_m$  is the difference in density between the particles and the surrounding fluid, and  $\sigma^*$  is the complex conductivity.

The effect of the passage of sound through the object, which is taken to be colloidal, is to produce an acoustic polarization  $\mathbf{P}_a$  within the object, so that the displacement vector becomes  $\mathbf{D} = \varepsilon \mathbf{E} + \mathbf{P}_a$ , where  $\varepsilon$  is the dielectric constant of the object and the surrounding medium, assumed to be identical. The polarization produced by the sound, within the context of the present calculation, is taken to be

$$\mathbf{P}_a = \alpha(\mathbf{x}, \omega) \nabla p$$

where

$$\alpha(\mathbf{x}, \omega) = \varepsilon f \Delta \rho_m \mu_E / \rho_m \sigma^*. \quad (2.2)$$

The parameter  $\alpha(\mathbf{x}, \omega)$  contains the space dependence of the concentration of colloid in addition to its dependence on the physical parameters of the colloidal suspension. For the present problem biological tissue is considered. Owing to the high absorption of ultrasound by water at frequencies above 10 MHz, it is reasonable to employ the quasi-electrostatic approximation  $\nabla \times \mathbf{E} \simeq 0$ , so that the electric field generated by the colloid can be written in terms of a potential  $\phi$  as

$$\mathbf{E} = -\nabla \phi. \quad (2.3)$$

It can be shown [7] that the potential can be found by solution of

$$\sigma \nabla^2 \phi + \varepsilon \frac{\partial}{\partial t} \nabla^2 \phi = \frac{\partial}{\partial t} (\nabla \cdot \mathbf{P}_a). \quad (2.4)$$

That is, if  $\mathbf{P}_a$  is known as a function of space and time then  $\phi$  can be determined. It can be seen that Eq. 2.4 is the fundamental equation for production of the potential distribution in space and time arising from a vibration potential whose spatial distribution is given by  $\alpha(\mathbf{x}, \omega)$ . It is further evident from the form of the left hand side of Eq. 2.4 that there are two mechanisms for production of the potential, one dependent on the conductivity of the body, and the other on its dielectric constant. Equation 2.4 can be transformed to the frequency domain by assuming that the acoustic pressure, the polarization, and the potential vary sinusoidally in time. The frequency domain differential equation for the potential is found to be

$$\nabla^2 \tilde{\phi} = \nabla \cdot (\alpha^\dagger \nabla \tilde{p}), \quad (2.5)$$

where  $\alpha^\dagger$  is given by  $\alpha^\dagger(\mathbf{x}, \omega) = \frac{i\omega}{\sigma + i\omega\varepsilon} \alpha(\mathbf{x}, \omega)$ , where frequency domain quantities are denoted with a tilde. Note that Eq. 2.5 is of the form of Poisson's equation, which is commonly encountered in electrostatics.

### 3. THE SOLUTION FOR THE POTENTIAL

Solution to Poisson's equation requires specification of boundary conditions. In the present problem, the boundaries are considered to be determined by two parallel, infinite plates separated a distance  $h$  with the ultrasound propagating perpendicularly to planes of the electrodes. The problem is simplified if both electrodes are maintained at ground potential. This can be effected by wiring a conductor between the two plates. In practice, the grounding of the plates can be carried out by attaching the electrodes to a low input impedance amplifier, which permits detection of the current and at the same time keeps the electrodes at essentially zero potential. The potential  $\tilde{\phi}$  for all points within the body can be determined using the Green's function solution to Poisson's equation. The potential, according to Green's theorem, is given by the sum of a volume and a surface integral. The Green's function is constructed so that it is zero on the surfaces of the electrodes. It can be seen that the result of assumption of zero potential on the electrodes and the use of a Green's function that is zero on the electrodes as well is that the surface integral becomes zero. The result of the calculation gives the frequency domain potential as

$$\tilde{\phi}(\mathbf{x}) = \int_{V'} G_D(\mathbf{x}, \mathbf{x}') \nabla' \cdot [\alpha^\dagger(\mathbf{x}', \omega) \nabla' \tilde{p}(\mathbf{x}')] dV', \quad (3.1)$$

where  $G_D(\mathbf{x}, \mathbf{x}')$  is the Green's function. The complicated form of the Green's function makes its evaluation over the region between the parallel plates cumbersome. However, the potential itself is not so important; it is the current in the external circuit that is of primary interest.

#### 4. THE CURRENT IN THE ELECTRODES

A current is generated in the external circuit as a result of the time varying polarization induced by the ultrasound in the colloid. The time varying polarization acts to produce an electric field and an electric displacement in the body. The variation in time of the displacement vector  $\mathbf{D}$  gives a current given by  $\mathbf{J}_P = \partial \mathbf{D} / \partial t$ . Since the potential is known throughout the body, the electric field can be found from the potential through Eq. 2.3, which, together with the relation for a linear dielectric  $\mathbf{D} = \epsilon \mathbf{E}$ , gives the polarization current as

$$\mathbf{J}_P(\mathbf{x}) = -\epsilon \frac{\partial}{\partial t} \nabla \tilde{\phi}(\mathbf{x}). \quad (4.1)$$

Thus, if the body is a dielectric and has a vanishing conductivity, there will still be a current in the external circuit as a result of the time varying polarization generated by the colloidal object.

The second mechanism for producing a current in the external circuit is more direct: wherever there is an electric field, there must also be a current of free charge carriers that follows the electric field lines  $\mathbf{J}_F$ , the magnitude of which is determined by the conductivity through the relation  $\mathbf{J}_F = \sigma \mathbf{E}$ . The current density expressed in terms of the potential becomes

$$\mathbf{J}_F(\mathbf{x}) = -\sigma \nabla \tilde{\phi}(\mathbf{x}). \quad (4.2)$$

The total current  $I$  must be the sum of the normal components of the two current densities integrated over the surface of one of the electrodes  $S$ , which, when written in terms of the potential, becomes

$$I = - \int \left[ \epsilon \frac{\partial}{\partial t} \nabla \tilde{\phi}(\mathbf{x}) + \sigma \nabla \tilde{\phi}(\mathbf{x}) \right] dx dy,$$

giving the current in the external circuit as

$$I = \frac{(\sigma + i\omega\epsilon)}{2\pi^2 h} \iint_{S'} dx dy \int_{V'} \frac{\partial}{\partial z} G_D(\mathbf{x}, \mathbf{x}')|_{z=0} \nabla' \cdot [\alpha^\dagger(\mathbf{x}', \omega) \nabla' \tilde{p}(\mathbf{x}')] dV'. \quad (4.3)$$

The result [7] of evaluating the integral in Eq. 4.3 is

$$I = \frac{i\omega}{h} \int_V \alpha(\mathbf{x}, \omega) \frac{\partial}{\partial z} p(\mathbf{x}) dx dy dz, \quad (4.4)$$

which gives the current for an arbitrary spatial distribution of colloid. A useful integral can be derived from Eq. 4.4 by using the linearized Navier-Stokes law for an inviscid fluid to replace the space derivative of the pressure giving

$$I = -\frac{i\rho\omega^3}{h} \int_V \alpha(\mathbf{x}, \omega) u(\mathbf{x}) dx dy dz. \quad (4.5)$$

The current is thus seen to be an integral of the displacement of the ultrasonic wave  $u(\mathbf{x})$  integrated over the region of the body containing the colloidal object.

#### 5. EXPERIMENTS

As a rudimentary demonstration of the capability of the vibration potential for imaging, an  $XY$  scan of a focused transducer across an agarose block containing a colloidal disk and ring was made. The agarose block was placed at the bottom of a cell with the agarose making contact with the electrode leading to the preamplifier. A saline solution in a cylindrical enclosure formed one of the electrodes for the cell as it made contact with the aluminum housing of the cell. The saline solution permitted translation of the transducer in a plane across the top of the cell and provided a delay line for the ultrasound as well. Ultrasound was generated using a 5.1 cm diameter, 15.2 cm focal length  $\text{LiNiO}_4$  transducer.

The ultrasound beam was approximately 3 mm in diameter where it probed the colloidal objects. The transducer was driven by a pulse generator that produced 900 kHz voltage bursts 28  $\mu\text{s}$  long with a repetition rate of 50 Hz, amplified by a gated power amplifier. The transducer was rastered in the

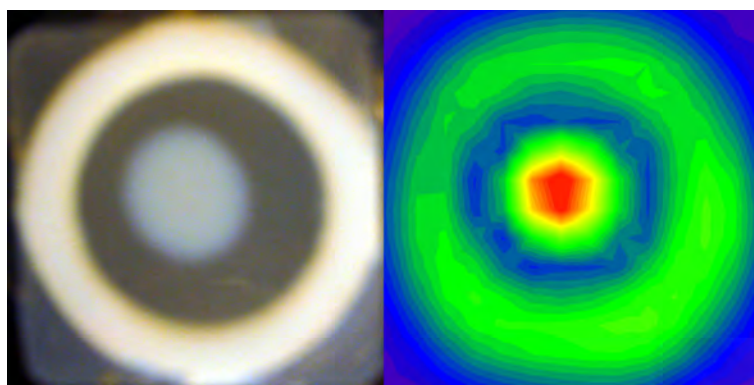


**Figure 1.** Colloidal ring and disk. Left: photograph. Right: vibration potential image. The colloidal objects were made by mixing 20 nm colloidal silica with agarose. The objects were then cast in an agarose block.

$XY$  plane while signals from the preamplifier were digitized and stored in a computer. Signals from the preamplifier were fed to both a digitizer and a lock-in amplifier that recorded simultaneously the amplitude and phase of the signal. Figure 1 shows a photograph and a vibration potential image of the colloidal ring and disk. The vibration potential image, in this case, is a measurement of the amplitude of the vibration potential as the transducer is rastered. As such, it does not rely on the mathematical model given in the previous section for the current.

## 6. SUMMARY

Equations 4.4 and 4.5 give expressions for the current in a circuit generated by a colloidal or ionic object inside a body. The evaluation of these expressions is possible for objects with simple geometries such as layers or spheres. Eqs. 4.4 and 4.5 also provide a starting point for the inverse problem where a current is recorded at various frequencies and the geometry of the object is determined. The image given here uses perhaps the simplest method of imaging where only an amplitude is recorded; more sophisticated images with depth resolution are clearly possible given the theoretical description of problem. Although not discussed here, the contrast mechanism for vibration potential imaging is unique. Its large variation in response to whole blood and muscle tissue suggests the use of vibration potential imaging to medical imaging.

## Acknowledgements

These experiments were supported by the US Army Medical Research and Materiel Command under Grant DAMD17-02-1-0307. Opinions, interpretations, conclusions, and recommendations are those of the authors and are not necessarily endorsed by the US Army.

## References

- [1] Debye, P. J. *JCP* **1856**, 1, 13.
- [2] Hunter, R. J. *Colloids and Surfaces* **1998**, 141, 37
- [3] Zana, R.; Yeager, E. . In *Modern Aspects of Electrochemistry*; Bockris, J. O.; Conway, B. E.; White, R. E., Eds.; Plenum: 1982.
- [4] Dukhin, A. S.; Goetz, P. J. *Colloids and Surfaces A* **2001**, 192, 267-306.
- [5] Beveridge, A. C.; Wang, S.; Diebold, G. J. *submitted for publication* .
- [6] OBrien, R. W. *J. Fluid Mech.* **1988**, 190, 71-86.
- [7] Gusev, V.; Diebold, G. *submitted for publication* .

# Frequency domain vibration potential imaging: Objects with symmetry in one dimension

Shougang Wang, Andrew C. Beveridge,<sup>a)</sup> Shengqiong Li, and Gerald J. Diebold<sup>b)</sup>

*Department of Chemistry, Brown University, Providence, Rhode Island 02912*

Cuong K. Nguyen

*Department of Physics, Brown University, Providence, Rhode Island 02912*

(Received 15 September 2006; accepted 6 November 2006; published online 13 December 2006)

Frequency domain, ultrasonic vibration potential imaging can be carried out by irradiating a colloidal object with a plane ultrasonic wave and recording the magnitude and phase of the current in a pair of electrodes as a function of the frequency. The method is applied to imaging of objects with symmetry in one dimension including a thin layer, a thick layer, pairs of layers, and layers with differing colloidal concentrations. The experimental results show agreement with the theory of vibration potential imaging where the recorded signal is proportional to the integral of the concentration of colloidal or ionic species over the pressure gradient in the ultrasonic wave. © 2006 American Institute of Physics. [DOI: 10.1063/1.2403933]

The ultrasonic vibration potential<sup>1-3</sup> refers to a voltage that is developed across a colloidal or ionic solution as a result of the passage of ultrasound. In the case of a colloid,<sup>4-7</sup> the normally spherical distribution of the counter-charge around colloidal particles is distorted by the passage of a sound wave that accelerates the particles and fluid in the colloid at different rates. The distortion of the electrical charge around the particles results in the formation of dipoles at the sites of each of the particles in the suspension, which, when summed over a macroscopic distance, can be measured as a potential over a distance parallel to the propagation direction of the ultrasound.

The application of the vibration potential to imaging has been described in Refs. 8 and 9 and a theory for determination of the vibration potential from a knowledge of the geometry of the irradiated body has been given in Ref. 10. Here we describe the application of vibration potential imaging to objects with symmetry in one dimension showing the capability of the method for frequency domain imaging.

The apparatus for the experiments, as shown in Fig. 1, is a cell with a housing made of aluminum, which provides both an electrical ground and shielding from stray electromagnetic radiation. The colloidal object rests inside the cell on a 25 mm thick agarose block at the bottom and is covered at the top with 10 cm of degassed tap water that acts to form an electrical connection between the top of the phantom and the grounded aluminum housing. The top and bottom of the phantom are electrically isolated. A metal plate, or in some of the experiments, a platinum wire, at the bottom of the phantom is connected through a feedthrough in the cell wall to a rf preamplifier (Analog Devices, Inc., model AD8021) with an amplification of 100. The amplified signal is then sent to a gated amplifier controlled by a transistor-transistor logic (TTL) signal from a digital delay generator synchronized to the firing of the ultrasonic burst that drives the transducer. The duration of the TTL signal is tailored so that the gated amplifier passes signals only at a time when the spatial

extent of the ultrasonic pulse fills the phantom; hence, the vibration potential generated when the ultrasound enters and leaves the colloidal region of the phantom is gated out.<sup>11</sup> The signal from gated amplifier is sent to a rf lock-in amplifier that records the in-phase  $x$  and quadrature  $y$  components of the signal, from which the magnitude  $R$  and phase  $\phi$  of the signal are determined. All data were taken with a time constant of 1 s. Ultrasound was generated by an unfocused 25.4 mm diameter LiNbO<sub>3</sub> transducer (Valpey Fisher Co., model E1178) driven by a pulsed power amplifier (RITEC, Inc., model GA2500) with a 0.2% duty cycle. The power amplifier is driven by a function generator which provides a slow frequency sweep over a preset range.

The first experiments were with thin layers made of 50  $\mu\text{m}$  thick lens paper saturated with a colloidal silica suspension (Snow Tex-OL-40 with a particle concentration of  $2.5 \times 10^{15}/\text{cm}^3$  manufactured by Nissan Chemical, Inc.) that was placed between two 25 mm thick agarose blocks made from 1% agarose (Sigma A9539) in water. The experiment was carried out by sending 35 cycles of a sinusoidal wave with a 50 Hz repetition rate to the power amplifier. The results of two experiments are shown in Fig. 2.

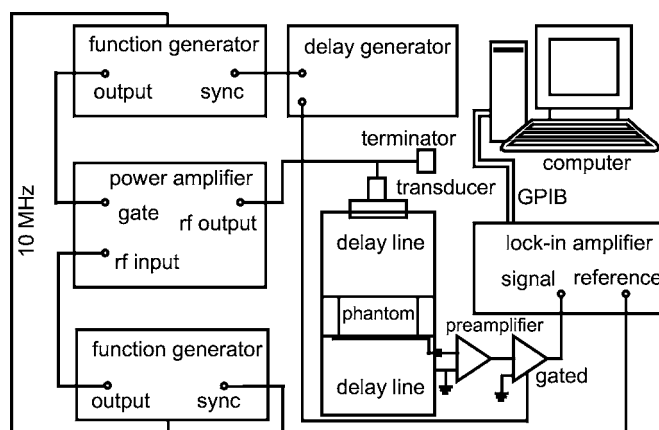


FIG. 1. Diagram of the experimental apparatus used to record vibration potentials in agarose phantoms. The internal oscillators in the two function generators are locked together with a 10 MHz synchronization signal.

<sup>a)</sup>Present address: Los Alamos National Laboratory, MS M888, Los Alamos, NM 87545.

<sup>b)</sup>Electronic mail: gerald\_diebold@brown.edu

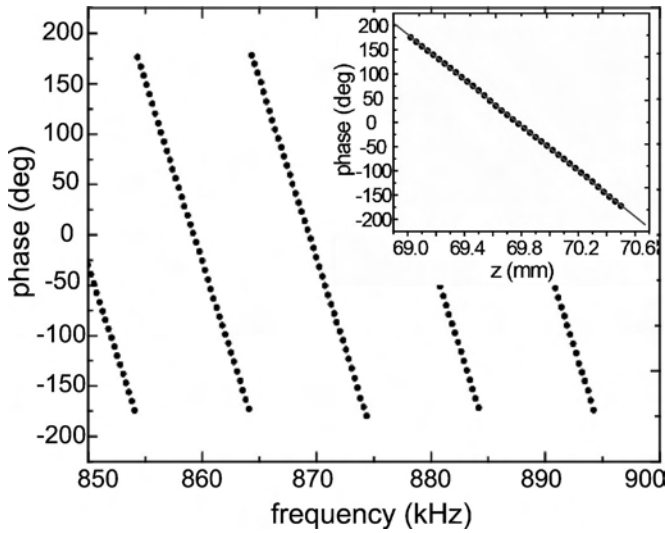


FIG. 2. Lock-in amplifier phase (in degrees) vs frequency recorded with a thin colloidal layer. Inset: Lock-in amplifier phase (in degrees) vs transducer-to-layer distance  $z_0$  for a thin colloidal layer.

According to the theory for objects with symmetry in one dimension,<sup>9,10</sup> the current per unit area arising from the vibration potential  $I(\omega)$  is given by an integral over the length of the cell,

$$I(\omega) = \Gamma \int \alpha(z) \frac{\partial p}{\partial z} dz, \quad (1)$$

where  $p$  is the pressure in the acoustic wave of frequency  $\omega$ ,  $\alpha(z)$  is a quantity proportional to the concentration of colloid,<sup>10</sup>  $\Gamma$  is a space independent quantity, and  $z$  is the coordinate. Consider generation of the vibration potential by a delta function layer at a position  $z_l + z_t$  from the transducer where the distribution of colloid in space is given by  $\alpha(z) = \bar{\alpha}_0 \delta(z - z_l)$ , where  $\bar{\alpha}_0$  is a constant with dimensions of  $\alpha$  times length. For a transducer (located at a coordinate  $-z_t$  from the first electrode) generating a plane wave, the acoustic pressure can be taken to be of the form  $p(\omega, z) = p_0 e^{-i[k(z+z_t) - \omega t]}$ , where  $p_0$  is a constant,  $k$  is the wave number given by  $k = \omega/c$ , and  $c$  is the sound speed. Note that the effect of acoustic reflections, which must influence signal generation, is not considered here. It follows from Eq. (1) that the signal generated is

$$I(\omega) = \Gamma_D e^{-i(kz_0 - \omega t)}, \quad (2)$$

where  $z_0 = z_t + z_l$  and  $\Gamma_D$  is a space independent quantity. Since the phase lag in the signal is given by  $2\pi f z_0/c$ , the distance between the transducer and the thin layer  $z_0$  can be determined from the slope of a phase lag versus frequency plot. If the sound speed is taken as 1523 m/s,  $z_0$  is found from the data in Fig. 2 to be  $150 \pm 2$  mm in excellent agreement with the measured<sup>12</sup> value of 150 mm.

A second experiment was done with the thin layer by fixing the frequency of the ultrasonic burst and translating the transducer upwards, i.e., in the position  $z$  direction. According to Eq. (2), a plot of the phase shift versus  $z_0$  is a line with a slope  $2\pi f/c$ . The data shown in the inset of Fig. 2 yield a sound speed in water of  $1486 \pm 40$  m/s in reasonable agreement with the room temperature value of 1523 m/s.

Consider a colloidal layer of finite thickness, the center of which is located a distance  $z_0$  from the transducer, and

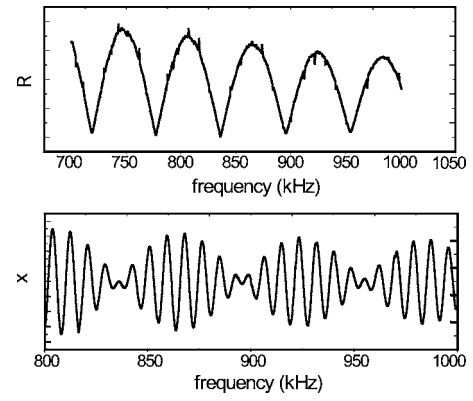


FIG. 3. Magnitude  $R$  in arbitrary units (upper plot) and in-phase component  $x$  (lower plot) vs frequency for a single colloidal 25.4 mm layer.

having a thickness  $L$ . The integration in Eq. (1) is over the range of  $z_0 - L/2$  to  $z_0 + L/2$  giving the recorded current as

$$I(\omega) = L \Gamma_L \text{sinc}(kL/2) e^{-i(kz_0 - \omega t)}, \quad (3)$$

where  $\Gamma_L$  is a space dependent quantity. For the experiments, a phantom was made by mixing colloidal silica with hot agarose (5% silica colloid by volume) and casting the layer over a previously formed 25 mm layer of neat agarose. A second 25 mm layer of neat agarose was poured on top of the silica layer to make a three layered object, only the center of which generated an appreciable vibration potential. The ultrasound from the transducer was a series of bursts whose spatial extent was greater than the layer thickness. The thickness of the colloidal layer was 25.4 mm; the thickness determined by a least squares fit of the data shown in Fig. 3 to Eq. (3) gave  $25.2 \pm 0.3$  mm. The center position of the layer was 175 mm away from the transducer, while the vibration potential data gave  $177 \pm 2$  mm.

For a sample containing two layers of colloid with dimensionless concentration parameters  $\alpha_1$  and  $\alpha_2$ , whose centers are at distances  $z_1$  and  $z_2$  from the transducer and whose thicknesses are  $L_1$  and  $L_2$ , Eq. (1) gives the signal as

$$S(k, t) = \Gamma_L [\alpha_1 L_1 \text{sinc}(kL_1/2) e^{-i(kz_1 - \omega t)} + \alpha_2 \text{sinc}(kL_2/2) e^{-i(kz_2 - \omega t)}], \quad (4)$$

the real part of which gives the in-phase component of the lock-in amplifier output. A phantom was made of two 3.5 mm thick colloidal silica disks (with  $\alpha_1 = \alpha_2$ ) placed in agarose, one on top of the other. The centers of the two disks were 174 and 191 mm from the transducer. Figure 4 shows the in-phase component of the lock-in amplifier output versus frequency. From a least squares fit of the experimental data to Eq. (4), the thicknesses of the layers were found to be  $3.4 \pm 0.2$  and  $3.7 \pm 0.2$  mm; and their distances from the transducer were determined to be  $175 \pm 2$  and  $193 \pm 3$  mm.

In another experiment, the phantom was made of two colloidal silica disks, one 10 mm and the other 12 mm thick, with the centers of the two disks 177 and 188 mm from the transducer. The concentration of the layer farthest from the transducer was twice that of the top layer. Figure 4 shows the results of the experiment, showing the in-phase component of the lock-in signal versus frequency. The fitting procedure gave the ratio of the colloid concentrations as  $1.9 \pm 0.3$ , the thicknesses of the layers as  $10.2 \pm 0.3$  and  $13.8 \pm 0.4$  mm, and the distances of the layers from the transducer as  $178 \pm 2$  and  $188 \pm 3$  mm, for the upper and lower layers, respectively.



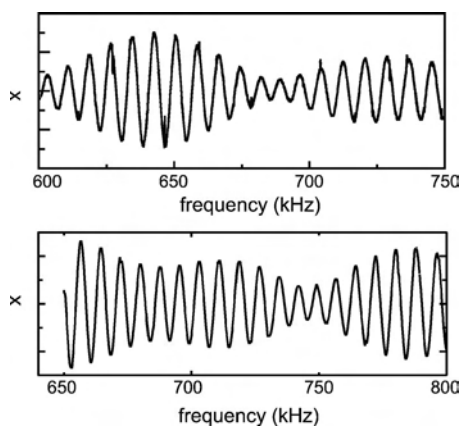


FIG. 4. Upper plot: In-phase component of the lock-in amplifier signal from a phantom made of two identical layers of colloid silica. Lower trace: In-phase component of the lock-in signal from a phantom made of two layers with different concentrations of colloidal silica.

In the theory given in Ref. 10, it has been assumed that the quantity  $\alpha$  is frequency independent which means that a factor of  $\omega$  appears in  $\Gamma$  in Eq. (1). In preliminary experiments with colloidal silica, an approximately  $1/f$  dependence of signal amplitude on frequency  $f$  has been found, albeit the frequency range of the experiments has been small. Thus, if the frequency dependence of  $\alpha$  is absorbed in  $\Gamma$ , then both  $\alpha$  and  $\Gamma$  can be taken as frequency independent quantities, as was done in deriving Eqs. (2)–(4).

If a focused transducer is employed, it is not difficult to see that a three-dimensional image could be constructed from a two-dimensional scan of the position of the transducer perpendicular to the propagation direction to the

acoustic wave vector where frequency domain data such as those given here are taken at each pixel. Alternately, image formation using time domain signals from a focused, short pulse of ultrasound rastered across a body can be employed much in the same manner as conventional ultrasound imaging. At this point, since imaging of only simple objects has been investigated, it is not certain whether time domain or frequency domain methods are preferable for acquiring images.

This work was supported by the US Army Medical Research and Materiel Command under Grant No. DAMD17-02-1-0307. Opinions, interpretations, conclusions, and recommendations are those of the authors and are not necessarily endorsed by the US Army.

<sup>1</sup>P. J. Debye, J. Chem. Phys. **1**, 13 (1933).

<sup>2</sup>R. J. Hunter, Colloids Surf., A **141**, 37 (1998).

<sup>3</sup>R. Zana and E. Yeager, *Modern Aspects of Electrochemistry* (Plenum, New York, 1982), Vol. 14, p. 1.

<sup>4</sup>R. W. O'Brien, J. Fluid Mech. **190**, 71 (1988).

<sup>5</sup>R. W. O'Brien, J. Colloid Interface Sci. **113**, 81 (1986).

<sup>6</sup>R. W. O'Brien, J. Fluid Mech. **212**, 81 (1990).

<sup>7</sup>R. W. O'Brien, D. W. Cannon, and W. N. Rolands, J. Colloid Interface Sci. **173**, 406 (1995).

<sup>8</sup>A. C. Beveridge, S. Wang, and G. J. Diebold, Proc. SPIE **5320**, 95 (2004).

<sup>9</sup>A. C. Beveridge, S. Wang, and G. J. Diebold, Appl. Phys. Lett. **85**, 5466 (2004).

<sup>10</sup>V. E. Gusev and G. J. Diebold, Ultrasound Med. Biol. **31**, 273 (2005).

<sup>11</sup>For example, in Fig. 2(a) of Ref. 8, only the large amplitude signal in the center of the figure is passed.

<sup>12</sup>As the phantoms change dimensions with the loss of moisture, it was found that the most accurate determination of the length parameters could be made by recording the time delay for appearance of the vibration potential or a reflected ultrasound pulse.

# Vibration Potential Imaging: Theory and Preliminary Results

Andrew C. Beveridge, Shougang Wang, \*Vitalyi Gusev, and Gerald J. Diebold

Department of Chemistry, Brown University, Providence, RI 02912 USA

\*Laboratoire de Physique de l'Etat Condensé, UPRESA, LeMans 72085, Cedex 09, France

## ABSTRACT

The ultrasonic vibration potential refers to the generation of a potential when ultrasound traverses a colloidal or ionic solution. The vibration potential can be used for imaging of tissue by sending a burst of ultrasound into a body and recording the vibration potential on the surface of the body with a pair of electrodes attached to a preamplifier and signal processing electronics. The theory of imaging in one-dimension is based on an integral of the ultrasound burst over the colloid distribution in space. A complete theory gives the current from the vibration potential as an integral of the product of the pressure with the component of the gradient of the colloid distribution in space in the direction of propagation of the ultrasound.

## 1. Introduction

Colloids, in general, consist of dense particles suspended in a fluid. Since the particles are charged owing to chemical groups on the particle surface, there is a counter charge that surrounds each particle, which normally has a spherical distribution around the particle when the suspension is at rest. The counter charge gives the solution overall charge neutrality, and is responsible for the stability of the colloid, since the repulsion of the counter charges keeps the particles at a distance from each other thereby preventing agglomeration and maintaining the stability of the suspension. When sound traverses a colloidal suspension, the motions of a particles in the suspension and the surrounding fluid differ because of the inertia of a particle and an equivalent volume of fluid differ. The result is that fluid flows back and forth over the particle surface on alternating half cycles of the acoustic wave. Since the counter charge is attached to the fluid, a dipole is generated at the site of each particle, which on addition over one half cycle of the sound wave results in a macroscopic voltage that can be recorded with two electrodes in solution. Similar considerations show that a vibration potential is generated in ionic solutions where the cation and anion have different effective masses in solution.

The vibration potential was predicted by Peter Debye<sup>1</sup> in 1933 for ionic solutions. Some time later the effect was found in ionic solutions; subsequently, much larger effects were found in colloidal suspensions. The theory of voltage production has been reviewed by several authors<sup>2-4</sup>. Here, we use O'Brien's expression, valid for dilute solution, for the electric field  $\mathbf{E}$  produced by a pressure  $p$ ,

$$\mathbf{E} = -\frac{\phi^0 \Delta\rho \mu_E}{\rho K^*} \nabla p, \quad (1)$$

where  $\phi^0$  is the volume fraction of particles,  $\Delta\rho$  is the density difference between the particles and the fluid,  $\mu_E$  is the electrophoretic mobility,  $\rho$  is the solution density, and  $K^*$  is the complex conductivity of the suspension. It can be seen that the effect is directly proportional to  $\Delta\rho$ , density difference between the colloidal particle and the surrounding fluid. Suspended particles with densities greater than or less than the fluid density produce a vibration potential, but particles with the same density as the fluid do not produce voltages when sound is present. If viscosity

is ignored, the Navier-Stokes law is simplified giving the gradient of the pressure in terms of the fluid acceleration  $\ddot{\mathbf{u}}(\mathbf{r},t)$  as

$$\ddot{\mathbf{u}} = -\nabla p / \rho. \quad (2)$$

In a one dimensional geometry with a plane wave propagating along the  $z$  axis, the acceleration can be written in terms of the displacement  $\mathbf{u}(z,t)$  at a time  $t$  as

$$\ddot{\mathbf{u}}(z, t) = -(ck)^2 \mathbf{u}(z, t), \quad (3)$$

where  $k$  is the wave number and  $c$  is the sound speed, where the radial frequency of the wave  $\omega$  can be set to  $ck$ . Consider a body that has a colloidal object with some arbitrary distribution of concentration as a function of the  $z$  coordinate,  $c(z)$ . The vibration potential is recorded externally to the irradiated body, and it assumed that  $c(z)$  can be zero at some points in space, but that the matter surrounding the colloidal region is a weak conductor so that the vibration potential can be recorded externally. The potential across the body  $\Delta\Psi$  is given by

$$\Delta\Psi(t) = \int \mathbf{E} \cdot d\mathbf{z}, \quad (4)$$

which is an integration over the dot product of the field and the coordinate, which in one dimension reduces to

$$\Delta\Psi(t) = \Gamma \int \hat{u}(\hat{z}, t) c(\hat{z}) d\hat{z}, \quad (5)$$

where  $\Gamma$  is a proportionality constant given by  $\Gamma = -\omega^2 \phi^0 \Delta\mu_E u_0 L / \rho K^*$ ,  $u_0$  is the magnitude of the acoustic displacement, and  $L$  is the length of the colloidal region, with the integration extending over the spatial extent of the sound wave. The expression for the potential has been written in terms of a dimensionless integral, which determines the time evolution of the potential.

The integral of the fluid displacement over the colloidal region given in Eq. 5 has an interpretation that explains many of the features of vibration potential imaging. The important conclusion to be drawn from Eq. 5 is that the signal is an integral of the sound wave over the distribution of colloid. More precisely, this should be written as a sum over all of the dipoles created by the sound wave, but within the context of a continuum model, the use of the integral is warranted. Consider a body with electrodes on its surface at the points  $z=0$  and  $z=3L$  with a distribution  $c(z)$  that is unity for  $z$  between  $L$  and  $2L$  and zero otherwise. The regions from  $z=0$  to  $L$  and from  $2L$  to  $3L$  are taken to be weak conductors. It follows that a short burst of sound whose spatial extent is shorter than  $L$  will produce a signal as it enters the colloidal region at  $z=L$ , but, when the burst lies totally within the colloidal region,  $L$  to  $2L$ , the potential will integrate to zero since the contributions of the positive and negative voltages over each half cycle cancel out. Thus an experiment would record two bursts of voltage, with the first voltage coming at a time  $L/c$  and the second burst coming at  $2L/c$ . The results for such an experiment with colloidal silica are shown in Fig. 1 where the two bursts can be seen with an intervening time period where the signal is zero corresponding to the time where the burst lies wholly within the colloidal layer.

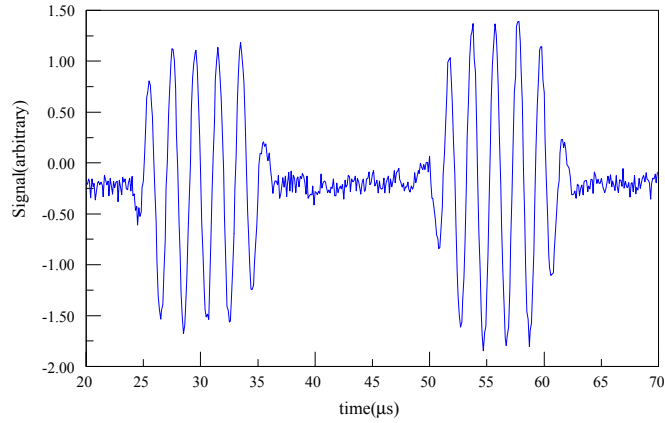


Figure 1. Response of a 25 mm silica colloid to a burst of five pulses of ultrasound. The length of the sound burst in time corresponds to a “short” burst, where the spatial extent of the burst is short compared with the layer of colloid.

The second important experimental case is when the burst has a spatial extent longer than  $L/c$ . This would correspond to a “long” burst of ultrasound, or continuous irradiation of the body. Here, the magnitude of the signal depends on whether an integral number of wavelengths of the sound equals  $L$  or not. If  $n\lambda=L$ , where  $n$  is an integer and  $\lambda$  is the wavelength of the sound, then there is an exactly equal number of half cycles producing positive and negative voltages in the colloid so that no overall voltage is recorded at the electrodes. On the other hand, if an integral number of half wavelengths equals the length of the colloidal region,  $n\lambda/2=L$ , then the maximum signal will be recorded at the electrodes. A long burst was used to record the signal shown in Fig. 2.

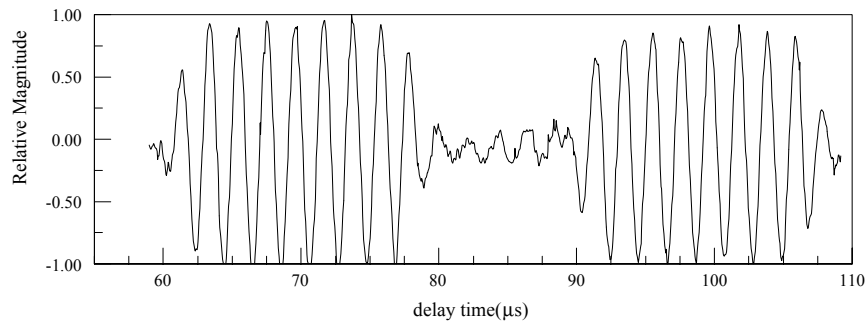


Figure 2 Experimental recording of vibration potential versus time for a burst whose spatial extent is large compared to the thickness of the colloidal region. The transducer was driven with a bipolar sinusoidal burst of 13 pulses at a driving voltage of 10 Vpp. The length of colloid channel was 25 mm; the frequency of the ultrasound was 494 kHz.

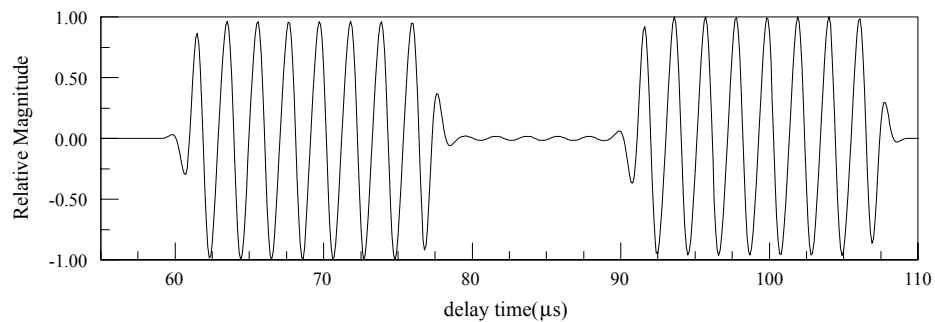


Figure 3 Theoretical calculation (corresponding to the conditions of Fig. 2) of the vibration potential versus time for a burst whose spatial extent is large compared to the thickness of the colloidal region. At the center of the trace, cancellation of the vibration potential is seen since an integral number of wavelengths of the ultrasound fit into the length of the colloidal region.

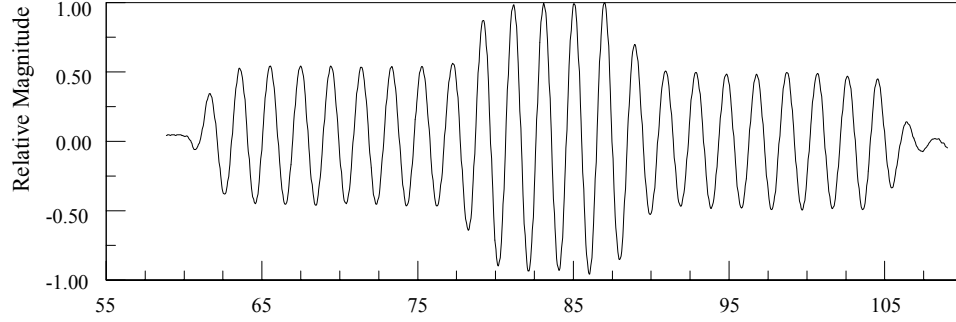


Figure 4 Calculation of the vibration potential versus time for a burst whose spatial extent is large compared to the thickness of the colloidal region from Eq. 2. The transducer driven with a bipolar sinusoidal burst of 13 pulses at a driving voltage of 10 Vpp. The length of colloid channel was 25 mm; the frequency of the ultrasound is 465 kHz.

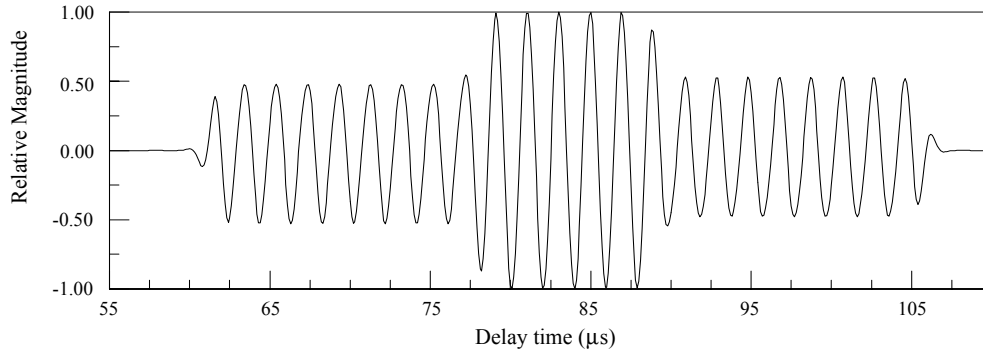


Figure 5 Theoretical calculation from Eq. 2 (corresponding to the conditions in Fig. 4) of the vibration potential versus time for a burst whose spatial extent is large compared to the thickness of the colloidal region. The large signal in the center corresponds to an integral number of half wavelengths fitting into the colloid channel.

For production of the vibration potential in a geometry more complicated than the one-dimensional case discussed above, the problem can be found from Maxwell's equations where the effect of the ultrasound is taken to produce a polarization within the irradiated body. For a body with a uniform dielectric constant  $\epsilon$  and conductivity  $\sigma$ , the problem reduces to solving Poisson's equation

$$\nabla^2 \phi = \nabla \cdot (\alpha' \nabla p) , \quad (6)$$

where  $\phi$  is the potential and  $\alpha'$  is given by

$$\alpha'(\omega) = \frac{\phi^0 \Delta \rho \mu_E / K^* \rho}{\epsilon - i \frac{\sigma}{\omega}}$$

In the case of a pressure wave propagating along the  $z$  axis, and with the electrodes intersecting the acoustic beam at perpendicular incidence, the solution to Poisson's equation can be found from a Green's function, which, for grounded electrodes, gives the current  $I$  generated by the time dependent pressure as

$$I = \frac{2\pi}{h} \int (\nabla \alpha')_z p dx dy dz , \quad (7)$$

where  $h$  is the distance between the two electrodes. It can be seen that the current is proportional to the pressure integrated over the  $z$  component of the spatial gradient of the colloidal suspension. The experimental implementation of the Dirichlet conditions imposed on the problem is a pair of electrodes at zero voltage, which would be implemented by use of a low input impedance preamplifier, such as a charge sensitive amplifier.

## 2. Experimental Results

Vibration potentials were generated using an apparatus where ultrasound is generated by a transducer attached to a vertical acoustic delay line that is attached to a cell containing the colloidal suspension. At the exit of the cell, opposite to the entrance delay line is an exit delay line used to eliminate or reduce reflections as the sound burst leaves the cell. Electrodes, one of which is attached to a grounded aluminum housing, are mounted on the ends of the delay lines. One electrode is wired to a low noise amplifier (Analog Devices, Inc. Model AD 8021) with an amplification of 100. The output of the preamplifier is fed to an oscilloscope and averaged over a number of bursts of ultrasound. The transducer is a conventional 500 kHz pzt transducer. A pulse generator whose output is fed to a power amplifier (Rytech, Inc. Model GA 2500) was used to drive the transducer. Imaging was carried out by translating a focused transducer across phantoms located at the bottom of the cell. The phantom was a block of agarose within which was cast a disk and a ring of colloidal silica mixed with agarose. The block of agarose contacted the bottom electrode that led to the input of the preamplifier. A column of dilute salt water formed the other electrode and also served as the delay line from the focused transducer. Signals from the preamplifier were digitized and stored, and were fed to a radio frequency lock-in amplifier as well. A computer rastered the focused beam across the phantom so that at each  $xy$  point, the digitized signal as well as the lock-in signal amplitude and phase were recorded in the computer.

The first experiment was carried out to determine the response of the phase of the lock-in amplifier to changes in the  $z$  coordinate. Figure 6 shows the phase of the quadrature component of the lock-in amplifier output as the transducer is scanned vertically in the  $z$  direction. Also shown is the time of arrival of the vibration potential. The phase of the quadrature

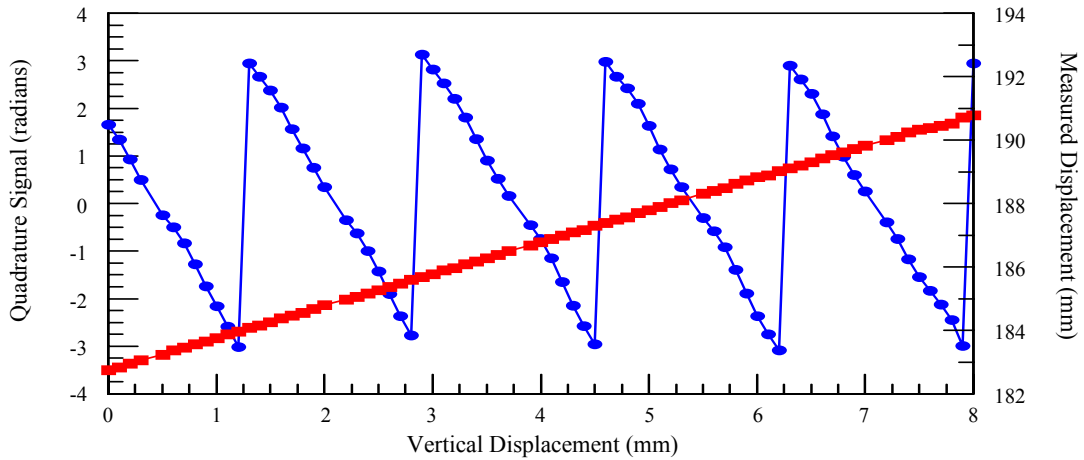


Figure 6. Straight line: Measured displacement in mm from time of arrival measurements versus displacement generated by the translation stage calculated using a sound speed of 1500 m/s. Sawtooth curve: phase of the quadrature signal from the lock-in amplifier versus vertical displacement of the transducer from a phantom.

component of the lock-in amplifier shows a decreasing signal as the displacement of the transducer from the phantom is increased. The jumps of  $2\pi$  correspond to resetting of the phase since the lock-in amplifier is restricted

to magnitudes of less than  $\pi$ . An integration of the phase can be used to determine distance. The time of arrival signal shown in the plot is found by setting a threshold for the signal amplitude. As such, the signal is capable of mapping out surfaces but without any information on the internal properties of the colloidal object.

There are several ways to carry out imaging with the vibration potential. The most obvious way would be to focus the ultrasound, and to record the time of arrival of the incident vibration potential signal, much in the way that conventional ultrasound is used in imaging. The present method under investigation uses a transducer that gives a narrow beam over a length in the  $z$  direction. The addition of focusing to the present technique would give somewhat better resolution. Clearly, the use of high frequency with its attendant higher focusing would improve the sharpness of the image. A surface recording, the rudiments of which are shown in Fig. 6 could be extended to a system where the body is irradiated from several sides, which would give a three-dimensional surface image. It is possible to show through the use of Eq. 5 that recording the in-phase and quadrature signals at a number of frequencies can be used to determine a curves, which when Fourier transformed, yield  $c(z)$  for a one-dimensional inversion of data. Such a procedure could be used at each  $xy$  point. There are methods based on Eq. 7 which use wide beams and an assumption of a spherical object that can be inverted to give the diameter of the sphere. Alternately, the time dependence of the vibration potential signal from a burst of ultrasound can be predicted for specific geometries using Eq. 7

### Acknowledgement

This work was supported by the US Army Medical Research and Materiel Command under Grant DAMD17-02-1-0307. Opinions, interpretations, conclusions and recommendations are those of the author and are not necessarily endorsed by the US Army. The authors are grateful for the assistance of Mr. S. Woythayler for design of the rf amplifier and electronics.

### References

1. P. Debye, J. Chem. Phys. 1, 13 (1933)
- 2 R. Zana, and E. Yeager, in "Modern Aspects of Electrochemistry (Plenum, New York, 1982) Bockris, J. O'M., Conway, B. E., & White, R. E. eds.
3. R. J.Hunter, "Recent developments in the Electroacoustic characterization of colloidal suspensions and emulsions" Colloids and Surfaces 141, 37-65 (1998)
4. A. S.Dukhin and P. J. Goetz, "New developments in acoustic and electroacoustic spectroscopy for characterizing concentrated dispersions". Colloids and Surfaces A 192, 267-306 (2001)
4. We use Eq. (4.2) from R. W. O'Brien, "Electro-acoustic effects in a dilute suspension of spherical particles", J. Fluid Mech. 190, 71-86 (1988)



● *Original Contribution***IMAGING WITH THE ULTRASONIC VIBRATION POTENTIAL: A THEORY FOR CURRENT GENERATION**

VITALYI E. GUSEV\* and GERALD J. DIEBOLD†

\*Université du Maine, Le Mans, France; and †Department of Chemistry, Brown University, Providence, RI, USA

(Received 26 August 2004, revised 27 October 2004, accepted 2 November 2004)

**Abstract**—The current in a circuit produced by a time-varying polarization generated by an object within a body in response to the passage of ultrasound (US) is found through solution to Maxwell's equations. Current generation is modelled in a body with uniform dielectric constant and conductivity where a finite region within the body produces an ultrasonic vibration potential. The results of the calculation form the mathematical basis for imaging through use of the ultrasonic vibration potential. (E-mail: Gerald\_Diebold@brown.edu) © 2005 World Federation for Ultrasound in Medicine & Biology.

**Key Words:** Ultrasound, Ultrasonic vibration potential, Imaging.

**INTRODUCTION**

The generation of a voltage in a colloidal or ionic suspension by ultrasound (US) is known as the ultrasonic vibration potential. In the case of a colloid, particles suspended within solution are charged and, in turn, are surrounded by a counter charge in the fluid giving the solution overall charge neutrality. Because the density of the particle and the surrounding fluid typically differ from each other, the passage of a sound through a suspension causes the motions of the particles and fluid to differ: in the typical case where the particles are denser than the surrounding fluid, the particles will execute a smaller amplitude motion than that of the fluid, with a phase that lags that of the fluid. The flow of the fluid relative to the particle distorts the normally spherical charge distribution of the counter charge and results in the creation of a dipole at the site of each particle, which alternates in direction on alternating cycles of the sound wave. If a pair of electrodes is placed in solution a distance one half of the sound wavelength apart, an alternating voltage can be recorded across the electrodes. The theory of the vibration potential, which was originally predicted by Debye (1933) for ionic solutions, has been reviewed by several authors

(Hunter 1998; Dukhin and Goetz 2001; Zana and Yeager 1983).

Here, we discuss the generation of the vibration potential as a means of imaging of colloidal or ionic species within an inert medium (Beveridge et al. 2004a, 2004b). The problem is to calculate the current developed in a pair of electrodes when US passes through a colloidal or ionic object within a body. The calculation for the Dirichlet problem is carried out for a pair of parallel electrodes at zero potential in contact with a medium with an isotropic conductivity and dielectric constant, within which is embedded an object with an arbitrary geometry of the same conductivity and dielectric constant as the surrounding medium, but which produces a vibration potential on the passage of US. There are two mechanisms for production of an alternating current in the circuit connecting the two electrodes: the first is the production of a current driven by the electric field in the body induced by the polarization, and the second is the generation of charges on the electrodes as a result of imposition of a time-varying polarization in the region between the parallel plates. This paper is divided into sections giving a derivation of Poisson's equation for determining the field from an arbitrary colloidal object, derivation of a Green's function for the parallel electrode geometry, and derivation of three expressions that can be used for calculating the current in an external circuit for an arbitrary object.

Address correspondence to: Dr. Gerald J. Diebold, Department of Chemistry, 324 Brook Street, Providence, RI 02912 USA. E-mail: Gerald\_Diebold@brown.edu

### POISSON'S EQUATION

The electric field  $\mathbf{E}$  produced across a region of colloid by a pressure  $p$ , according to O'Brien (1988) is given by:

$$\mathbf{E} = \frac{f\Delta\rho_m\mu_E}{\rho_m\sigma^*} \nabla p, \quad (1)$$

where  $f$  is the volume fraction of colloidal particles in the fluid,  $\mu_E$  is the electrophoretic mobility of the particles,  $\rho_m$  is the mass density of the suspension and  $\Delta\rho_m$  is the difference in densities between the particles and the surrounding fluid, and  $\sigma^*$  is the complex conductivity (O'Brien 1986; The complex conductivity  $\sigma^*$  used by O'Brien is a generalized conductivity that relates the current density to the electric field in a colloid).

Consider generation of the vibration potential in a medium with conductivity  $\sigma$ , and dielectric constant  $\varepsilon$ , assumed uniform throughout the medium under consideration, but with one region of the medium, referred to here as the object, that generates a vibration potential on the passage of sound. By combining the charge conservation relation  $\nabla \cdot \mathbf{J} = \partial\rho/\partial t$ , where  $\mathbf{J}$  is the current density and  $\rho$  is the charge density, with the constitutive relation  $\mathbf{J} = \sigma\mathbf{E}$ , where  $\mathbf{E}$  is the electric field and  $\sigma$  is the real part of the conductivity, and Maxwell's equation  $\rho = \nabla \cdot \mathbf{D}$ , where  $\mathbf{D}$  is the electrical displacement, it follows that:

$$\nabla \cdot (\sigma\mathbf{E}) = -\frac{\partial}{\partial t}(\nabla \cdot \mathbf{D}). \quad (2)$$

The effect of the passage of sound through the object, which is taken to be colloidal, is to produce an acoustic polarization  $\mathbf{P}_a$  within the object, so that the displacement vector becomes:

$$\mathbf{D} = \varepsilon\mathbf{E} + \mathbf{P}_a, \quad (3)$$

where  $\varepsilon$  is the dielectric constant of the object and the surrounding medium, assumed to be identical. It is assumed that the polarization  $\mathbf{P}$  varies in space, depending on whether the coordinate is within the object or in the inert region of the body. The polarization produced by the sound, within the context of the present calculation, is taken to be:

$$\mathbf{P}_a = \alpha(\mathbf{x}, \omega) \nabla p \quad (4)$$

where

$$\alpha(\mathbf{x}, \omega) = \varepsilon f \Delta\rho_m \mu_E / \rho_m \sigma^*.$$

The notation for  $\alpha(\mathbf{x}, \omega)$  explicitly contains the space variable to indicate that it takes on different values in the colloidal and non colloidal regions. The combination of eqn (3) with eqn (2) gives:

$$\nabla \cdot \left[ \sigma\mathbf{E} + \frac{\partial}{\partial t}(\varepsilon\mathbf{E} + \mathbf{P}_a) \right] = 0. \quad (5)$$

For the present problem, where the media under consideration would normally be biologic tissue, the frequencies where the vibration potential can be generated are restricted owing to ultrasonic absorption; hence, it is reasonable to make the quasi-electrostatic approximation where  $\nabla \times \mathbf{E} \approx 0$ , so that the electric field can be written in terms of a potential  $\phi$  as:

$$\mathbf{E} = -\nabla \phi. \quad (6)$$

Substitution of eqn (6) into eqn (5) gives:

$$\sigma\Delta^2\phi + \varepsilon\frac{\partial}{\partial t}\nabla^2\phi = \frac{\partial}{\partial t}(\nabla \cdot \mathbf{P}_a), \quad (7)$$

from which the potential in the time domain can be determined from a knowledge of  $\mathbf{P}_a$  in space and time. Equation (7) can be found in the frequency domain by assuming that the acoustic pressure, the polarization and the potential vary sinusoidally in time according to:

$$p = \text{Re}[\tilde{p}(\mathbf{x})e^{i\omega t}]$$

$$\mathbf{P}_a = \text{Re}[\tilde{\mathbf{P}}_a(\mathbf{x})e^{i\omega t}]$$

$$\phi = \text{Re}[\tilde{\phi}(\mathbf{x})e^{i\omega t}],$$

which, on substitution into eqn (7), gives Poisson's equation for the frequency domain potential in terms of the acoustic polarization as:

$$\nabla^2\tilde{\phi} = \frac{i\omega}{\sigma + i\omega\varepsilon} \nabla \cdot \tilde{\mathbf{P}}_a, \quad (8)$$

or

$$\nabla^2\tilde{\phi} = \nabla \cdot (\alpha^\dagger \nabla \tilde{p}), \quad (9)$$

where  $\alpha^\dagger$  is given by:

$$\alpha^\dagger(\mathbf{x}, \omega) = \frac{i\omega}{\sigma + i\omega\varepsilon} \alpha(\mathbf{x}, \omega). \quad (10)$$

It can be seen that eqns (8) and (9) are Poisson's equations with the acoustic polarization acting as a source. The source is dependent on derivatives of both the colloidal object and the pressure in space.

### GREEN'S FUNCTION FOR THE POTENTIAL

Consider the geometry for imaging a colloidal object of arbitrary shape inside a weakly conducting body with a pair of conducting electrodes in contact with the external surface of the body, as shown in Fig. 1. The electrodes are considered to be parallel and spaced a distance  $h$  apart, with the direction of the US taken to be

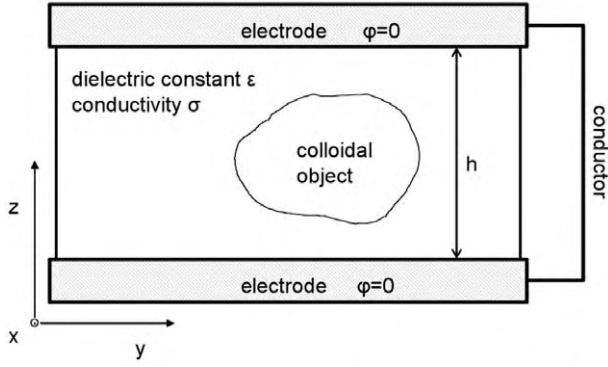


Fig. 1. A colloidal object is embedded within a body. The object and the surrounding region are taken to have a conductivity  $\sigma$  and a dielectric constant  $\epsilon$ . Only the colloidal region within the body produces a vibration potential; the region outside the object is considered to be inert.

along the  $z$ -axis. The electrodes are assumed to be connected to each other through a conductor or, equivalently, through an amplifier with an input impedance of nearly zero so that the potentials of each of the electrodes are effectively zero. The potential  $\tilde{\phi}$  within the body can be determined from a Green's function solution to Poisson's equation through use of a Dirichlet Green's function  $G_D(\mathbf{x}, \mathbf{x}')$ , that satisfies the equation:

$$\nabla^2 G_D(\mathbf{x}, \mathbf{x}') = \delta(\mathbf{x} - \mathbf{x}'), \quad (11)$$

where  $\mathbf{x}$  and  $\mathbf{x}'$  are the field and source points, respectively. The potential, according to Green's theorem is then given by:

$$\tilde{\phi}(\mathbf{x}) = \int_{V'} G_D \nabla' \cdot (\alpha^\dagger \nabla' \tilde{p}) dV' + \oint \left[ \tilde{\phi} \frac{\partial G_D}{\partial n'} - G_D \frac{\partial \tilde{\phi}}{\partial n'} \right] dS', \quad (12)$$

where the integration in both integrals is over the primed coordinates, and where the derivatives in the surface integral are taken with respect to the surface normal  $n$ . Because the potentials on the planes at  $z = 0$  and  $z = h$  are taken to be zero, it is convenient to construct a Green's function that is also zero on the surfaces of the electrodes and to take the surface of integration to be a rectangular enclosure in the body, with its ends at the positions of the electrodes where the potential is zero, and where the enclosure extends to infinity in the  $x$  and  $y$  directions.

Consider the Fourier transformation of the spatial coordinate in eqn (11) through the transform pair:

$$\bar{f}(\kappa_x, \kappa_y) = \frac{1}{(2\pi)^2} \int_{-\infty}^{\infty} \int_{-\infty}^{\infty} f(x, y) e^{-i(\kappa_x x + \kappa_y y)} dx dy \quad (13a)$$

$$f(x, y) = \int_{-\infty}^{\infty} \int_{-\infty}^{\infty} \bar{f}(\kappa_x, \kappa_y) e^{i(\kappa_x x + \kappa_y y)} d\kappa_x d\kappa_y \quad (13b)$$

to give the Green's function  $\bar{G}_D(\kappa_x, \kappa_y, z; \mathbf{x}')$  in reciprocal space. Fourier transformation of eqn (11) gives:

$$\left( \frac{\partial^2}{\partial z^2} - \kappa_x^2 - \kappa_y^2 \right) \bar{G}_D(\kappa_x, \kappa_y, z; \mathbf{x}') = \frac{1}{(2\pi)^2} \delta(z - z') e^{-i(\kappa_x x' + \kappa_y y')}, \quad (14)$$

where the Green's function in reciprocal  $xy$  space is  $\bar{G}_D(\kappa_x, \kappa_y, z)$ . Because the Green's function must vanish at  $z = 0$  and  $z = h$ , it can be of the form  $\bar{G}_D = \sum A_m \sin(d_m z)$ , where  $d_m = m\pi/h$ ,  $A_m$  is a constant independent of  $z$  and  $m$  is an integer ranging from 1 to  $\infty$ . By multiplication of eqn (14) by  $\sin d_m' z$  and integration of the resulting expression from 0 to  $h$ , it can be shown that the reciprocal space Green's function is given by:

$$\bar{G}_D(\kappa_x, \kappa_y, z; \mathbf{x}') = -\frac{1}{2\pi^2 h} \sum_1 \frac{\left[ \sin\left(\frac{m\pi}{h} z\right) \sin\left(\frac{m\pi}{h} z'\right) \right]}{\left[ \left(\frac{m\pi}{h}\right)^2 + \kappa_x^2 + \kappa_y^2 \right]} \times e^{-i\kappa_x x' - i\kappa_y y'}, \quad (15)$$

which, on transformation back to coordinate space according to eqns (13a) and (13b) gives the Green's function as:

$$G_D(\mathbf{x}, \mathbf{x}') = -\frac{1}{2\pi^2 h} \sum_1 \sin\left(\frac{m\pi}{h} z\right) \sin\left(\frac{m\pi}{h} z'\right) \times \int_{-\infty}^{\infty} \int_{-\infty}^{\infty} \frac{e^{i\kappa_x(x-x') + i\kappa_y(y-y')}}{\left[ \left(\frac{m\pi}{h}\right)^2 + \kappa_x^2 + \kappa_y^2 \right]} d\kappa_x d\kappa_y. \quad (16)$$

Because the potential  $\tilde{\phi}$  is zero on the upper and lower electrodes by assumption, and  $G_D(\mathbf{x}, \mathbf{x}')$  is zero on the upper and lower electrodes by construction, the surface integrals in eqn (12) are zero, so that the frequency domain potential is given by the volume integral:

$$\tilde{\phi}(\mathbf{x}) = \int_{V'} G_D(\mathbf{x}, \mathbf{x}') \nabla' \cdot [\alpha^\dagger(\mathbf{x}', \omega) \nabla' \tilde{p}(\mathbf{x}')] dV', \quad (17)$$

where  $G_D(\mathbf{x}, \mathbf{x}')$  is given by eqn (16) and where the integration over the primed coordinates is explicitly indicated in the integrand.

## THE CURRENT IN THE ELECTRODES

There are two mechanisms for production of current in the electrodes (O'Brien 1988). If the region between the two plates is a nonconducting dielectric, a current will be generated in the external circuit connecting the two electrodes as a result of the flow of charge induced by the time-varying polarization induced by the US in the colloidal or ionic object. The current density  $\mathbf{J}_p$  generated by a time-varying displacement vector  $\mathbf{D}$  is given by  $\mathbf{J}_p = \partial \mathbf{D} / \partial t$ , where the displacement vector can be found from the potential through eqn 6 and the constitutive relation for a dielectric  $\mathbf{D} = \epsilon \mathbf{E}$ . Thus,  $\mathbf{J}_p$  is found from the potential as

$$\mathbf{J}_p(\mathbf{x}) = -\epsilon \frac{\partial}{\partial t} \nabla \phi(\mathbf{x}). \quad (18)$$

Similarly, when a field is produced in a weak conductor by a time-varying polarization, the current density for the free charge  $\mathbf{J}_f$  is related to the electric field as  $\mathbf{J}_f = \sigma \mathbf{E}$ , so that the current density expressed in terms of the potential becomes:

$$\mathbf{J}_f(\mathbf{x}) = -\sigma \nabla \phi(\mathbf{x}), \quad (19)$$

The current produced by both mechanisms  $I$  is found by integrating the normal component of the electric field, that is, the component perpendicular to one of surfaces, over the surface of one of the electrodes  $S$ ; hence, the expression for the frequency domain current  $\tilde{I}$  in the external circuit is given by:

$$\tilde{I} = \frac{(\sigma + i\omega\epsilon)}{2\pi^2 h} \int \int_{S'} dx dy \int_V \frac{\partial}{\partial z} G_D(\mathbf{x}, \mathbf{x}') \Big|_{z=0} \nabla' \cdot [\alpha^\dagger(\mathbf{x}', \omega) \nabla' \tilde{p}(\mathbf{x}')] dV',$$

which, on substitution of  $G_D(\mathbf{x}, \mathbf{x}')$  from eqn (16) carrying out the differentiation with respect to  $z$ , and evaluation of the integral at  $z = 0$  gives:

$$\tilde{I} = \frac{(\sigma + i\omega\epsilon)}{2\pi^2 h} \int \int_{S'} dx dy \int_V \sum_1 \left( \frac{m\pi}{h} \right) \sin \left( \frac{m\pi}{h} z' \right) \times \int_{-\infty}^{\infty} \int_{-\infty}^{\infty} \frac{e^{i\kappa_x(x-x') + i\kappa_y(y-y')}}{\left[ \left( \frac{m\pi}{h} \right)^2 + \kappa_x^2 + \kappa_y^2 \right]} d\kappa_x d\kappa_y \nabla' \cdot [\alpha^\dagger(\mathbf{x}', \omega) \nabla' \tilde{p}(\mathbf{x}')] dV'. \quad (20)$$

Note that the factor of  $(\sigma + i\omega\epsilon)$  appears both in the prefactor to the integral and in the denominator of eqn (10) that defines  $\alpha^\dagger$ ; hence, eqn (20) can be expressed in terms of  $\alpha$  rather than  $\alpha^\dagger$ . The integration over  $x$  and  $y$  gives  $(2\pi)^2 \delta(\kappa_x) \delta(\kappa_y)$ , which simplifies eqn (20) considerably. Through use of the identity:

$$\sum_1 \frac{\sin nx}{n} (-1)^n = -\frac{1}{2}x$$

eqn 20a can be shown to reduce to:

$$\tilde{I} = -\frac{i\omega}{h} \int_V z \left[ \frac{\partial}{\partial x} \left( \alpha \frac{\partial}{\partial x} \tilde{p} \right) + \frac{\partial}{\partial y} \left( \alpha \frac{\partial}{\partial y} \tilde{p} \right) + \frac{\partial}{\partial z} \left( \alpha \frac{\partial}{\partial z} \tilde{p} \right) \right] dx dy dz, \quad (21)$$

where the primes have been dropped in the integrand. If each of the terms in eqn (21) is integrated by parts, noting that the dimensions of the object are such that it does not contact either of the electrodes, so that  $\alpha$  can be taken as zero at  $z = h$  or  $z = 0$ , it is not difficult to show that the only term that remains is the third term in the integrand, so that the current is given by:

$$\tilde{I} = \frac{i\omega}{h} \int_V \alpha(\mathbf{x}, \omega) \frac{\partial}{\partial z} p(\mathbf{x}) dx dy dz. \quad (22)$$

It is also possible to carry out an integration of this expression by parts as well, giving an alternate expression for the current in the circuit as:

$$\tilde{I} = -\frac{i\omega}{h} \int_V [\nabla \alpha(\mathbf{x}, \omega)]_z p(\mathbf{x}) dx dy dz. \quad (23)$$

A useful integral can be derived from eqn (22) by using the linearized Navier–Stokes law for an inviscid fluid,  $\nabla p / \rho = -\ddot{\mathbf{u}}$  where  $\mathbf{u}$  is the displacement of the medium in the acoustic field. The acceleration in a plane wave can be expressed in terms of the displacement through the relation  $\ddot{\mathbf{u}} = -\omega^2 \tilde{\mathbf{u}}$ . Thus, an expression for the current in terms of the displacement in the plane wave can be written as:

$$\tilde{I} = \frac{i\rho\omega^3}{h} \int_V \alpha(\mathbf{x}, \omega) \tilde{u}(\mathbf{x}) dx dy dz. \quad (24)$$

## INFINITE SLAB

The problem of a slab of thickness  $a$  located between two metal electrodes connected by a low-impedance amplifier, as shown in Fig. 2, can be solved by application of eqn (23). The impedance of the amplifier is taken to be so small that it acts as a short circuit, so that the potential of the two electrodes can be considered as

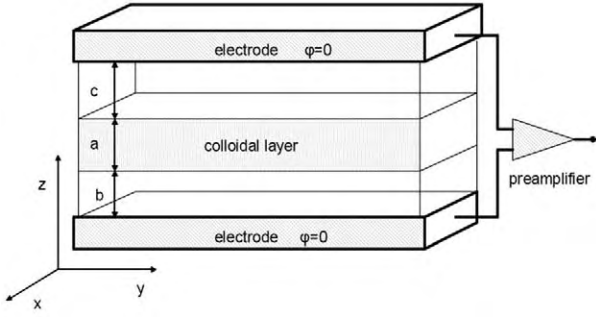


Fig. 2. An infinite slab of a colloidal suspension lies between two electrodes. The input impedance of the amplifier is considered to be sufficiently low that the potential of each electrode can be taken to be zero.

zero. The slab and the surrounding material are considered to have the same dielectric constant  $\epsilon$ ; however, the slab in region “a”, located between  $z = b$  and  $z = b + a$  is assumed to be the only region where a vibration potential is generated. The ultrasonic beam is assumed to be continuous and to propagate along the positive  $z$ -axis. For the present problem, the distribution of colloid in space is given by  $\alpha(z, \omega) = \alpha_0[u(z - b) - u(z - b - a)]$ , where  $\alpha_0$  refers to a value of  $\alpha(x, \omega)$  independent of  $x$  in layer  $a$  whose magnitude is given by eqn (4), and  $u$  is the Heaviside function. Because the layers are considered to be infinite in the  $x$  and  $y$  directions, a current per unit area  $J$  is generated by the time-varying polarization, which, according to eqn (23), is found to be:

$$\tilde{J} = -\frac{i\omega\alpha_0}{h}[\tilde{p}(b+a) - \tilde{p}(b)]. \quad (25)$$

It is possible to consider the same problem without the use of eqn (23) by assuming a time-varying polarization  $\mathbf{P}_a$  that is generated by the vibration potential, and calculating the resulting current when the material in layers “b” and “c” are dielectrics with dielectric constant  $\epsilon$ . From eqn (3a), the electric field in the three regions is given by:

$$E(z) = \frac{1}{\epsilon}[D_0 - P_a(z)], \quad (26)$$

where  $E$ ,  $D$  and  $P_a$  are the components of electric field, displacement, and acoustic polarization along the positive  $z$ -axis. The acoustic polarization has a value  $P_a$  inside region  $a$ , and is zero in regions  $b$  and  $c$ . Because there are no free charges in the three layers, the displacement vector has a constant value  $D_0$ . From eqn (6), it follows that:

$$\phi(h) - \phi(0) = 0 = -\int_0^h Edz = \frac{-1}{\epsilon} \left[ \int_0^h D_0 dz - \int_b^{b+a} P_a dz \right]. \quad (27)$$

Therefore, the component of the displacement vector along the  $z$ -axis in all three layers is given by:

$$D_0 = \frac{1}{h} \int_b^{b+a} P_a dz. \quad (28)$$

It is not difficult to show that the electric fields and polarizations in regions  $b$  and  $c$  are identical. If an integration volume is taken as a closed cylindrical volume crossing the region between the upper electrode and region  $b$ , then it follows from Maxwell's equation  $\nabla \cdot \mathbf{D} = \rho$  that  $D_0 = -\sigma_s$ , where  $\sigma_s$  is the charge density on the upper electrode. Because magnitude of the current density  $J$  is given by  $J = d\sigma_s/dt$ , the frequency domain current density is:

$$\tilde{J} = -\frac{i\omega}{h} \int_b^{b+a} P_a dz, \quad (29)$$

which, for an acoustic polarization  $\tilde{\mathbf{P}}_a = \alpha(\omega, \mathbf{x})\nabla\tilde{p}$ , recovers eqn (25), as found directly from eqn (23), above.

Note the simplification that follows from the assumption of a 1-D geometry in this problem. If an acoustic beam with a finite cross-section were employed, then the direction of the electric field would not be parallel to the  $z$ -axis over the entire area of the slab, and a more complicated calculation of the current density would be required. The magnitude of the error in determining the current density through use of eqn (25) for a finite cross-section acoustic beam would, of course, depend on the dimensions of the beam relative to the width of the gaps between the colloidal layer and the conductors.

## DISCUSSION

Equations (22) to (24) give three equivalent expressions for the current in a circuit generated by a colloidal or ionic object inside a body irradiated by a beam of US. The third of these gives perhaps the most intuitive picture of the process of current generation, in that it states that the current is proportional to material displacement in the acoustic wave integrated over the region where colloid is present. Thus, the production of current is seen as proportional to the integration of the dipole moments at the sites of the particles over the region where there is a displacement caused by the acoustic wave. Note that, depending on the frequency and spatial extent of the wave, the integration can be finite or zero. This property



is seen explicitly in the solution for the current given by eqn (25), which shows that a sinusoidal pressure wave whose spatial extent is smaller than the length of the colloidal region generates no signal when the wave is confined within the colloidal layer (in which case  $\tilde{p}(b+a) = \tilde{p}(b) = 0$ ); only when such a short burst enters or exits the layer is a current produced. For a continuous wave, or an ultrasonic burst whose spatial extent is large compared with the layer thickness, when an even or odd number of half wavelengths of the acoustic wave equals the length of the colloidal layer, the vibration potential across the layer integrates to zero, or takes on a maximal value. For other wavelengths, the signal integrates to some current intermediate between these two extrema. Further, it is easy to see that recording the frequencies that give consecutive maxima and minima in the vibration potential permits determination of the layer thickness. The simple example of the slab also makes clear the interpretation of eqn (23), in that a gradient of the concentration of colloid is required for a current to be generated for burst of US: a fixed amplitude sound wave crossing a boundary between colloidal and inert material generates a current at the points where it enters or leaves the colloidal region. Equally, eqn (22) states that, if there is an acoustic wave that varies in space propagating wholly within a colloidal layer of uniform concentration, it is possible to observe a current from the vibration potential.

Different methods of generating an image are evident in the results obtained here. In addition to determination of the thickness of a colloidal or ionic layer in a 1-D geometry already mentioned, a method based on the time of appearance of the vibration potential is inherent in eqns (23) and (24). The distance a colloidal region lies from the launching point of an ultrasonic wave can be determined from a knowledge of the sound speed in the body and the appearance time of the vibration potential signal relative to the launching time of the sound wave,

in a manner analogous to conventional ultrasonic imaging. In general, the frequency-dependence of the current for a continuous ultrasonic wave, or the time-dependence of any acoustic burst sequence generated by an object whose geometry is known, can be determined from eqn (23). It is expected that, for a number of simple geometries, straightforward expressions for the vibration potential can be obtained in closed form, which will prove of value in the interpretation of vibration potential signals for imaging (Beveridge et al. 2004b). In summary, the present work gives explicit expressions for the current recorded in an imaging experiment for objects whose geometry is known *a priori*; in addition, it gives a starting point for solution of the inverse problem where vibration potential data are gathered to determine the spatial extent of an arbitrary object whose geometry and location within a body is sought.

**Acknowledgements**—This work was supported by the US Army Medical Research and Materiel Command (grant DAMD17-02-1-0307). Opinions, interpretations, conclusions and recommendations are those of the authors and are not necessarily endorsed by the US Army.

## REFERENCES

- Beveridge AC, Wang S, Diebold GJ. Vibration potential imaging: Theory and preliminary results. *Proc SPIE* 2004a;5320:95–100.
- Beveridge AC, Wang S, Diebold GJ. Imaging based on the ultrasonic vibration potential. *Appl Phys Lett* 2004;85:5466–5468.
- Debye PJJ. A method for determination of the mass of electrolytic ions. *Chem Phys* 1933;1:13–16.
- Dukhin AS, Goetz PJ. New developments in acoustic and electroacoustic spectroscopy for characterizing concentrated dispersions. *Colloids Surfaces A* 2001;192:267–306.
- Hunter RJ. Recent developments in the electroacoustic characterization of colloidal suspensions and emulsions. *Colloids Surfaces* 1998;141:37–66.
- O'Brien RWJ. The high frequency dielectric dispersion of a colloid. *Colloid Interface Sci* 1986;113:81–93.
- O'Brien RWJ. Electro-acoustic effects in a dilute suspension of spherical particles. *Fluid Mech* 1988;190:71–86.
- Zana R, Yeager E. Ultrasonic vibration potentials. In: Bockris JO'M, Conway BE, White RE, eds. *Modern aspects of electrochemistry*. New York: Plenum, 1983:1–60.

# ULTRASONIC VIBRATION POTENTIAL IMAGING: THEORY AND EXPERIMENTS

Shougang Wang, Cuong K. Nguyen, and Gerald J. Diebold  
Department of Chemistry, Brown University, USA, 02912

## ABSTRACT

The ultrasonic vibration potential refers to the voltage generated when ultrasound traverses a colloidal or ionic fluid. The theory of imaging based on the vibration potential is reviewed, and an expression given that can be used to determine the signal from arbitrary objects. The experimental apparatus consists of a pair of parallel plates connected to the irradiated body, a low noise preamplifier, a radio frequency lock-in amplifier, translation stages for the ultrasonic transducer that generates the ultrasound, and a computer for data storage and image formation. Experiments are reported where bursts of ultrasound are directed onto colloidal silica objects placed within inert bodies.

## 1. INTRODUCTION

Colloids are suspensions of charged particles in a liquid, the amount of the charge being governed by the attachment of chemical groups to the surface. Since each particle is charged, thus there must be a counter charge residing in the fluid surrounding the particle in order to have overall charge neutrality of the fluid. In the absence of a disturbance, the charge distribution around each particle is spherical; however, when sound propagates through a suspension where the particles have either a higher or lower density than that of the surrounding fluid, the motion of the particle will differ from that of the fluid surrounding the particle in cases where the density of the particle differs from that of the fluid. Since the counter charge is carried by the fluid and the charge on the particle is bound chemically to the particle surface, the oscillatory motion of the fluid relative to the particle distorts the spherical counter charge distribution so that on alternating cycles of the sound wave, a dipole is created at the site of each particle. If a pair of electrodes is placed in the solution a distance apart that is less than one half the sound wavelength, an alternating potential, known as the ultrasonic vibration potential, is found between the electrodes at the oscillation frequency of the acoustic wave. Similar considerations show that vibration potentials are generated in ionic solutions as well. The theory of the colloidal vibration potential as it pertains to ionic and colloidal solutions has been given in Refs..<sup>1-5</sup>

In this paper, we give a review of the principles of the theory vibration potential imaging<sup>6</sup> and describe imaging experiments<sup>6-8</sup> with colloidal objects that show the basic features of the modality.

## 2. THEORY OF CURRENT GENERATION

As shown in Fig. 1, the apparatus for recording a vibration potential signal is a pair of parallel electrodes covering the body of interest with a beam of ultrasound directed at perpendicular incidence to the plates. It is assumed that the colloidal object and the dielectric between the electrodes have the same conductivity  $\sigma$  and dielectric constant  $\epsilon$ . The interaction of the ultrasound with the colloidal object within the body gives rise to a varying polarization on the object which, in turn, generates a time varying displacement. As a result of the presence of the time varying displacement, a current is generated in a circuit connected to the two plates.

Signal production is described in detail in Ref..<sup>6</sup> The first step in finding the signal in an imaging experiment is determining the electric field  $\mathbf{E}$  produced across a region of colloid by a pressure field  $p$ . According to Ref..<sup>4</sup> the electric field is given by  $\mathbf{E} = (f \Delta \rho_m \mu_E / \rho_m \sigma^*) \nabla p$ , where  $f$  is the volume fraction of colloidal particles in the fluid,  $\mu_E$  is the electrophoretic mobility of the particles,  $\rho_m$  is the mass density of the suspension, and  $\Delta \rho_m$  is the difference in densities between the particles and the surrounding fluid, and  $\sigma^*$  is the complex conductivity.

---

For further information, send correspondence to G.J.D. at Gerald\_Diebold@Brown.edu, Telephone: 401 863 3586

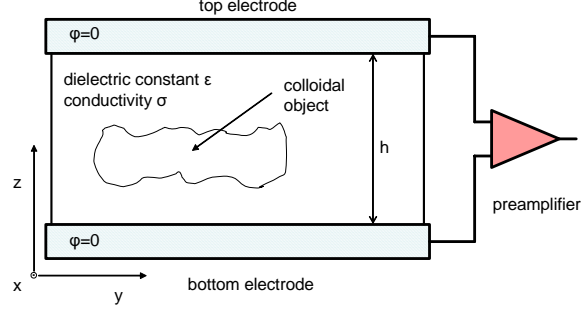


**Figure 1.** Diagram of an imaging apparatus. A beam of ultrasound propagating along the z-axis is scanned over a body containing a colloidal object. The electrodes are connected to a low input impedance amplifier so that the potential difference between the two electrodes is zero.

In accord with the discussion given above, if the colloidal particles in suspension have the same density as the fluid, no vibration potential is generated by the passage of ultrasound.

The electric displacement  $\mathbf{D}$  is related to the acoustic polarization  $\mathbf{P}_a$  and the electric field in the dielectric through the relation

$$\mathbf{D} = \varepsilon \mathbf{E} + \mathbf{P}_a. \quad (1)$$

where  $\varepsilon$  is the dielectric constant. The polarization produced by the sound is taken to be

$$\mathbf{P}_a = \alpha(\mathbf{x}, \omega) \nabla p,$$

where the factors that govern production of the vibration potential are absorbed in to the parameter  $\alpha(\mathbf{x}, \omega)$  given by

$$\alpha(\mathbf{x}, \omega) = \varepsilon f \Delta \rho_m \mu_E / \rho_m \sigma^*. \quad (2)$$

The electric field in the quasielectrostatic approximation can be written in terms of a potential  $\phi$  as  $\mathbf{E} = -\nabla \phi$ . From Maxwell's equations, it can then be shown that

$$\sigma \nabla^2 \phi + \varepsilon \frac{\partial}{\partial t} \nabla^2 \phi = \frac{\partial}{\partial t} (\nabla \cdot \mathbf{P}_a), \quad (3)$$

which shows that the potential be determined from a knowledge of  $\mathbf{P}_a$  in space and time. By transforming Eq. 3 into the frequency domain, a Poisson equation of the form

$$\nabla^2 \tilde{\phi} = \nabla \cdot (\alpha^\dagger \nabla \tilde{p}) \quad (4)$$

is obtained where a modified form of the function that describes the spatial distribution of the colloid in space  $\alpha^\dagger$  is given by

$$\alpha^\dagger(\mathbf{x}, \omega) = \frac{i\omega}{\sigma + i\omega\varepsilon} \alpha(\mathbf{x}, \omega). \quad (5)$$

Next, in order to solve Eq. 4 it is necessary to specify boundary conditions on the potential and to determine a Green's function. For the geometry given in Fig. ??, the appropriate Dirichlet Green's function,<sup>6</sup> which has the property that it vanishes at the surfaces of the two electrodes, is given by

$$G_D(\mathbf{x}, \mathbf{x}') = -\frac{1}{2\pi^2 h} \sum_1^\infty \sin\left(\frac{m\pi}{h} z\right) \sin\left(\frac{m\pi}{h} z'\right) \int_{-\infty}^\infty \int_{-\infty}^\infty \frac{e^{i\kappa_x(x-x') + i\kappa_y(y-y')}}{[(\frac{m\pi}{h})^2 + \kappa_x^2 + \kappa_y^2]} d\kappa_x d\kappa_y. \quad (6)$$



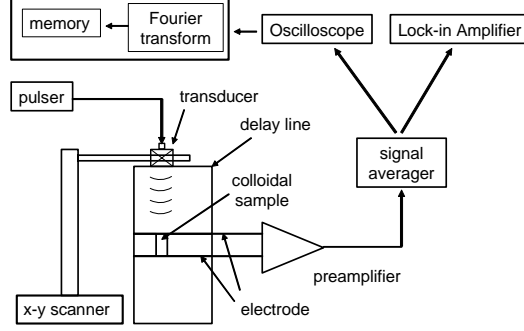


**Figure 2.** Diagram of the experimental apparatus. The instrument can be used with the transducer in a fixed position in experiments when the entire phantom is irradiated with at plane wave, or the transducer can be rastered across the phantom when a focused transducer is used

Since the Green's function has been constructed to vanish at the electrode surfaces and the potential is specified to be zero on the electrodes, the surface integrals that contribute to the potential are identically zero; hence the expression for the frequency domain potential is

$$\tilde{\phi}(\mathbf{x}) = \int_{V'} G_D(\mathbf{x}, \mathbf{x}') \nabla' \cdot [\alpha^\dagger(\mathbf{x}', \omega) \nabla' \tilde{p}(\mathbf{x}')] dV', \quad (7)$$

where  $G_D(\mathbf{x}, \mathbf{x}')$  is given by Eq. 6. There are two sources for current in the circuit, a polarization current density dependent on the time derivative  $\mathbf{D}$  equal to  $-\epsilon \frac{\partial}{\partial t} \nabla \phi(\mathbf{x})$ , and a current  $\sigma \mathbf{E}$  from electrical conduction equal to  $-\sigma \nabla \phi(\mathbf{x})$ . By summing these two contributions the expression for the current in the circuit is found to be

$$\tilde{I} = -\frac{i\omega}{h} \int_V [\nabla \alpha(\mathbf{x}, \omega)]_z p(\mathbf{x}) dx dy dz. \quad (8)$$

Thus, the current measured in the circuit is proportional to the  $z$  component of the gradient of the distribution of colloid in space. It follows that the vibration potential signal responds only to changes in concentration of the colloidal species in space—a constant distribution of colloid in space yields no current.

### 3. APPARATUS AND EXPERIMENTS

The experimental apparatus as shown in Fig. 2 consists a cell made of aluminum as the sample housing with the colloidal object placed in the middle of the cell. Ultrasound was generated by a 25.4 mm in diameter PZT transducer driven by a pulse generator (Hewlett Packard Inc. Model 8114) and RF power amplifier (Ritec, Inc. Model. GA2500), or by a high voltage pulser (Panametrics, Inc. Model 8114A). The delay line, which is typically a weak saline solution, at the top of sample guarantees that the sample is in the far field of the transducer. The delay line at the bottom of the cell is used to eliminate the effect of sound reflections at the bottom of the cell. Electrodes are placed on both sides of the sample. The top electrode is directly connected to the aluminum housing which is used as ground; the bottom electrode is connected to a feedthrough connector leading to an RF preamplifier (Analog Devices, Inc. Model AD8021) with a voltage gain of 100, whose output is fed to a wideband switched-input operational amplifier used for gating (Burr-Brown Corp. Model OPA678). The gated amplifier eliminates the RF pick-up at time zero and the signal generated by the sound reflected from the bottom of the cell. The gated signal is sent to an RF lock-in amplifier (SRS Model 844) whose output is displayed on an oscilloscope and recorded in a computer. Both the magnitude and phase of the vibration potential signal are stored in the computer.

A plot of vibration potential versus time for a colloidal silica layer is shown in Fig. 3. The pulser used in the experiment generates a spike of high voltage, which when delivered to the transducer produces an acoustic pulse that is approximately one cycle of 1 MHz radiation. The phase inversion predicted by the theory for the

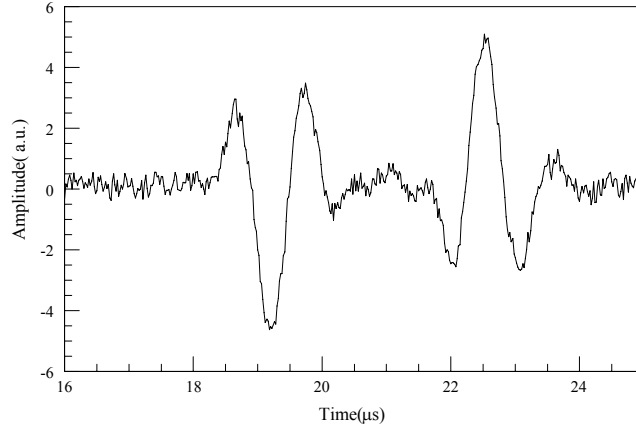


**Figure 3.** Experimental plot of vibration potential signal from a 5 mm colloidal silica layer versus time. The acoustic pulse was generated by a voltage spike from the Panametrics Inc. pulser. The phase difference of  $\pi$  in the signals corresponding to entering and exiting a layer is a characteristic of vibration potential imaging.

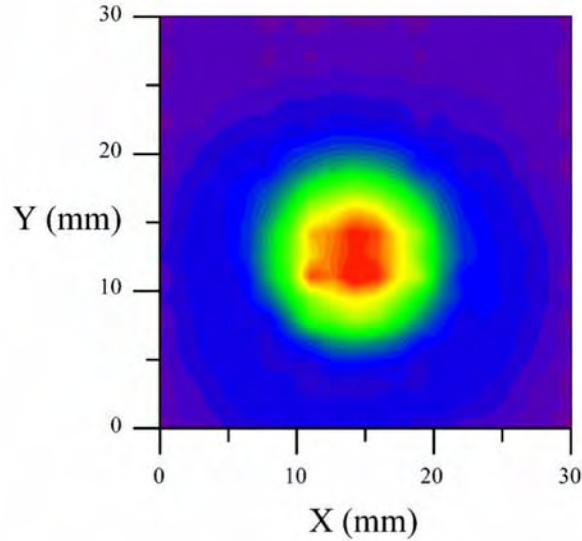


**Figure 4.** Vibration potential image of a disk shaped, colloidal object formed by scanning a focused transducer. Only the vibration potential where the pulse entered the colloidal object was used to record the image. The transducer used to produce the ultrasound was driven by a few cycles of 1 MHz radiation from the Ritec, Inc. pulse generator.

pulse entering and leaving the layer is clearly evident in the vibration potential signal. The delay time between the firing of the acoustic pulse and the appearance of the first peak in the vibration potential gives the distance between the transducer and the layer, while the time difference between the two vibration potential pieces yields the thickness of the layer, provided the sound speed is known.

Formation of two-dimensional images is carried out by rastering a focused 1 MHz transducer across the cell in which the sample is placed. The simplest image, an example of which is shown in Fig. 4, is obtained by plotting the magnitude of the vibration potential signal versus position. The resolution in the image is dependent on the resolution achieved by the transducer.

#### 4. DISCUSSION

In an imaging modality based on the amplitude of the vibration potential signal, contrast in the image is necessarily determined by the relative colloidal and ionic characteristics of objects within the body being investigated. Blood, which is a marker for malignant tumors, is well-known to be both colloidal and ionic, whereas muscle tissue, for instance, is not considered to have any colloidal characteristics. Previous vibration potential imaging experiments<sup>7</sup> have, in fact, shown that there is a difference in the magnitude of the vibration potential between whole blood and muscle tissue on the order of 500. It follows then, that the application of vibration potential imaging to biological tissue would be expected to give a map of the concentration of blood in space

#### 5. ACKNOWLEDGEMENT

The support of the US Army Medical Research and Materiel Command under Grant DAMD17-02-1-0307 is gratefully acknowledged.

#### REFERENCES

1. P. J. Debye, *J. Chem. Phys.* **1**, 13 (1933).
2. R. J. Hunter, *Colloids and Surfaces* **141**, 37 (1998).
3. R. Zana, E. Yeager, *Modern Aspects of Electrochem.* **14**, 1 (1982).
4. R. W. O'Brien, *J. Fluid Mech.* **190**, 71 (1988).
5. R. W. O'Brien, *J. Colloid and Interface Sci.* **113**, 81 (1986).
6. V. E. Gusev, G. J. Diebold, *Ultrasound in Med. and Biol.* **31**, 273 (2005).
7. A. C. Beveridge, S. Wang, G. J. Diebold, *Appl. Phys. Lett.* **85**, 5466 (2004).
8. A. C. Beveridge, S. Wang, G. J. Diebold, *Proc. SPIE 2004* **5320**, 95 (2004).

# X-ray phase-contrast imaging: transmission functions separable in Cartesian coordinates

Guohua Cao, Theron J. Hamilton, Christoph Rose-Petruck, and Gerald J. Diebold

*Department of Chemistry, Brown University, Providence, Rhode Island 02912, USA*

Received September 1, 2006; revised October 19, 2006; accepted October 27, 2006;  
posted November 1, 2006 (Doc. ID 74560); published March 14, 2007

In-line, x-ray phase-contrast imaging is responsive to both phase changes and absorption as the x radiation traverses a body. Expressions are derived for phase-contrast imaging of objects having transmission functions separable in Cartesian coordinates. Starting from the Fresnel–Kirchhoff integral formula for image formation, an expression is found for the phase-contrast image produced by an x-ray source with nonvanishing dimensions. This expression is evaluated in limiting cases where the source-to-object distance is large, where the source acts as a point source, and where the weak phase approximation is valid. The integral expression for the image is evaluated for objects with simple geometrical shapes, showing the influence of the source dimensions on the visibility of phase-contrast features. The expressions derived here are evaluated for cases where the magnification is substantially greater than one as would be employed in biological imaging. Experiments are reported using the in-line phase-contrast imaging method with a microfocus x-ray source and a CCD camera.

© 2007 Optical Society of America

OCIS codes: 340.0340, 110.7440.

## 1. INTRODUCTION

The method of in-line phase-contrast imaging,<sup>1,2</sup> where contrast is produced by refraction of x rays, has strong appeal for high-resolution imaging of biological tissue as a result of its high resolution and its sensitivity to density variations. Basically, the phase-contrast method consists of directing a spatially coherent source of x radiation such as the output from an x-ray synchrotron<sup>3–5</sup> onto an object and recording the resulting x-ray intensity pattern on film or an equivalent detector such as a CCD camera. The conversion of phase changes, introduced by traversal of the x radiation through a body with density variations, into intensity changes in the image is an interference phenomenon that can be described by the Huygens principle.<sup>6</sup> A more intuitive picture of phase-contrast imaging has been given in Ref. 2, which shows that at points in a body where strong variations in the index of refraction are found deflection of the x radiation takes place to produce either an accumulation or a loss of x-ray photons at points on the image plane irrespective of whether the radiation is monochromatic.<sup>7</sup>

The theory of phase-contrast imaging<sup>8,9</sup> shows that the transmission function, which can include absorption, denoted  $q(X, Y)$ , where  $X$  and  $Y$  are the coordinates on the object perpendicular to the propagation direction of the radiation, governs image formation through the well-known Fresnel–Kirchhoff integral.<sup>6</sup> Here we derive expressions using the Fresnel–Kirchhoff diffraction integral that can be used to calculate phase-contrast images where the transmission function  $q(X, Y)$  or, in the weak phase approximation, where the phase function  $\phi(X, Y)$  is separable. That is, we find integral expressions for cases where  $q(X, Y)$  can be written as the product of two one-dimensional functions,  $q(X, Y) = q_x(X)q_y(Y)$ , and, in a second case, where the phase function is separable as a prod-

uct,  $\phi(X, Y) = \phi_x(X)\phi_y(Y)$ . The derivation of the expression for the intensity at the image plane given in Section 2 includes the effects of source size, which is evaluated for the case of a Gaussian intensity profile. The expression for the intensity is also reduced to an expression for a point source, the case of symmetry in one dimension, a nearly plane wave, and a weak phase object. Section 3 gives examples of the use of the mathematical expressions in calculating images. Results from experiments with a microfocus x-ray source are given in Section 4. Section 5 describes the utility of the factorization of the transmission function, describes facets of the use of x-ray phase-contrast imaging for biological applications, and compares the results given here with previous studies. The work reported here focuses on imaging where the magnification of the object and the resolution are appropriate for detection of small density variations in biological specimens.

## 2. IMAGE FORMATION

### A. Two-Dimensional Transmission Function

The electric field  $f$  on the image plane for an x-ray source of unit electric field amplitude that approximates a point source is governed by the Fresnel–Kirchhoff integral,<sup>9</sup>

$$f = \frac{i}{\lambda} \int_{\Sigma_0} \frac{e^{-ik|\mathbf{r}-\mathbf{r}'|}}{|\mathbf{r}-\mathbf{r}'|} d\sigma, \quad (1)$$

where  $\Sigma_0$  is the plane of the object,  $\mathbf{r}'$  is the coordinate on the object plane,  $k$  is the wavenumber of the radiation,  $d\sigma$  represents integration over the object, and  $\mathbf{r}$  is the coordinate on the image plane. With the notation given in Fig. 1 the distance between the integration point on the object

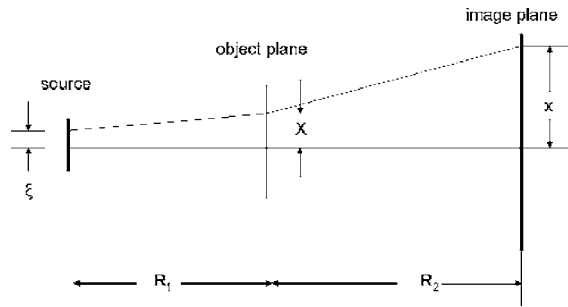


Fig. 1. Schematic drawing of the imaging apparatus and coordinates for phase-contrast imaging with a finite source size. The coordinates on the source, object, and image planes are denoted  $(\xi, \eta)$ ,  $(X, Y)$ , and  $(x, y)$ , respectively.

plane  $\mathbf{r}'$  and the point  $\mathbf{r}$  in the image plane can be written as  $|\mathbf{r}-\mathbf{r}'|=[R_2^2+(x-X)^2+(y-Y)^2]^{1/2}$  and expanded to first order. The electric field in the object plane is of the form  $e^{-ik|\mathbf{r}''-\mathbf{r}'|}/|\mathbf{r}''-\mathbf{r}'|$ , where  $\mathbf{r}''$  is the coordinate on the source plane and can be expanded in a similar manner. In the Fresnel approximation,<sup>8</sup> Eq. (1) reduces to<sup>10</sup>

$$f(x,y) = \frac{i}{\lambda} \frac{e^{-ik(R_1+R_2)}}{R_1 R_2} \int e^{-ik(\xi-X)^2/2R_1} e^{-ik(x-X)^2/2R_2} q_x(X) dX \times \int e^{-ik(\eta-Y)^2/2R_1} e^{-ik(y-Y)^2/2R_2} q_y(Y) dY, \quad (2)$$

where the transmission function  $q(X, Y)$  has been taken to be a separable function of the form

$$q(X, Y) = \begin{cases} q_x(X)q_y(Y) & \text{if } |X| \leq a \text{ and } |Y| \leq b \\ 1 & \text{if } |X| > a \text{ or } |Y| > b \end{cases}, \quad (3)$$

where  $2a$  and  $2b$  are the dimensions of the object in the  $X$  and  $Y$  directions, respectively. The transmission functions in both the  $X$  and the  $Y$  directions are assumed to be of the form

$$q(\xi) = e^{i\phi(\xi) - \mu(\xi)},$$

so that the phase of the wave as it exits the object is governed by  $\phi$  and the absorption<sup>11</sup> by  $\mu$ .

Consider the  $X$  integration in Eq. (2), which extends from  $-\infty$  to  $\infty$ . Following Ref. 3, the  $X$  integration can be written as

$$\int_{-\infty}^{\infty} E q(X) dX = \int_{-\infty}^{\infty} E dX + \int_{-a}^a E [q(X) - 1] dX,$$

where the exponential factor in Eq. (2) is denoted  $E$ . The same procedure can be applied to the integral over  $Y$  so that Eq. (2) becomes

$$f(x,y) = S \left\{ \underbrace{\int_{-\infty}^{\infty} e^{-ik(\xi-X)^2/2R_1} e^{-ik(x-X)^2/2R_2} dX}_{\alpha} + \underbrace{\int_{-a}^a e^{-ik(\xi-X)^2/2R_1} e^{-ik(x-X)^2/2R_2} [q_x(X) - 1] dX}_{\beta} \right\} \times \left\{ \underbrace{\int_{-\infty}^{\infty} e^{-ik(\eta-Y)^2/2R_1} e^{-ik(y-Y)^2/2R_2} dY}_{\gamma} + \underbrace{\int_{-b}^b e^{-ik(\eta-Y)^2/2R_1} e^{-ik(y-Y)^2/2R_2} [q_y(Y) - 1] dY}_{\kappa} \right\}, \quad (4)$$

where  $S = i e^{-ik(R_1+R_2)}/\lambda R_1 R_2$ . Equation (4) gives the field at any point  $(x, y)$  on the image plane for radiation emanating from a point  $(\xi, \eta)$  on the source plane that traverses an object with a transmission function of the form  $q_x(X)q_y(Y)$ .

The term in Eq. (4) denoted  $\alpha$  can be written as

$$\alpha = e^{-ik\xi^2/2R_1 - ikx^2/2R_2} \int_{-\infty}^{\infty} e^{-ikX^2(1/R_1+1/R_2)/2 + ik(\xi/R_1+x/R_2)X} dX. \quad (5)$$

By completing the square in the integrand of Eq. (5) and carrying out the integration, using integrals of the form  $\int_0^\infty \cos(a^2x^2)dx = \int_0^\infty \sin(a^2x^2)dx = \sqrt{\pi/2}/2a$  for  $a > 0$ , we can show that the quantity  $\alpha$  reduces to

$$\alpha = \sqrt{\frac{2\pi R_1 R_2}{ik(R_1+R_2)}} e^{-ik(x-\xi)^2/2(R_1+R_2)}. \quad (6)$$

The term  $\gamma$  in Eq. (4) is evaluated in the same manner and is identical to  $\alpha$ , but with  $x$  replaced by  $y$  and with  $\xi$  replaced by  $\eta$ . The terms  $\beta$  and  $\gamma$  require specification of the transmission function in order to complete the integration.

Consider a Gaussian-source intensity distribution of the form

$$s(\xi, \eta) = \frac{1}{\pi\sigma^2} e^{-(\xi^2+\eta^2)/\sigma^2},$$

where  $\sigma$  is the length parameter for the source.

The intensity<sup>10</sup> recorded at the image plane for an incoherent source with a source intensity distribution  $s(\xi, \eta)$  at the source plane is

$$I(x,y) = \iint |f(x,y)|^2 s(\xi, \eta) d\xi d\eta, \quad (7)$$

which, according to Eq. (4), becomes

$$I(x, y) = \int \int |(\alpha + \beta)(\gamma + \kappa)|^2 s(\xi, \eta) d\xi d\eta. \quad (8)$$

For the case of a source intensity that is separable as a product of two functions  $s(\xi)$  and  $s(\eta)$ ,

$$s(\xi, \eta) = s(\xi)s(\eta);$$

since  $\alpha$  and  $\beta$  are functions of  $x$  and  $\xi$  only and  $\gamma$  and  $\kappa$  are functions of  $y$  and  $\eta$  only, the double integral in Eq. (8) can be factored as a product of two independent integrals to give

$$I(x, y) = \left( \frac{1}{\lambda R_1 R_2} \right)^2 \frac{1}{\sigma \sqrt{\pi}} \int (\alpha \alpha^* + 2 \operatorname{Re}(\alpha \beta^*) + \beta \beta^*) e^{-\xi^2/\sigma^2} d\xi \times \frac{1}{\sigma \sqrt{\pi}} \int (\gamma \gamma^* + 2 \operatorname{Re}(\gamma \kappa^*) + \kappa \kappa^*) e^{-\eta^2/\sigma^2} d\eta. \quad (9)$$

It follows that  $I(x, y)$  can be written as

$$I(x, y) = \left( \frac{1}{\lambda R_1 R_2} \right)^2 [I_{\alpha\alpha^*}(x; q_x) + 2 \operatorname{Re} I_{\alpha\beta^*}(x; q_x) + I_{\beta\beta^*}(x; q_x)] \times [I_{\alpha\alpha^*}(y; q_y) + 2 \operatorname{Re} I_{\alpha\beta^*}(y; q_y) + I_{\beta\beta^*}(y; q_y)], \quad (10)$$

where

$$I_{\alpha\alpha^*}(x; q_x) = \frac{1}{\sigma \sqrt{\pi}} \int \alpha \alpha^* e^{-\xi^2/\sigma^2} d\xi, \quad (11)$$

$$I_{\alpha\beta^*}(x; q_x) = \frac{1}{\sigma \sqrt{\pi}} \int \alpha \beta^* e^{-\xi^2/\sigma^2} d\xi, \quad (12)$$

$$I_{\beta\beta^*}(x; q_x) = \frac{1}{\sigma \sqrt{\pi}} \int \beta \beta^* e^{-\xi^2/\sigma^2} d\xi. \quad (13)$$

The three integrals over  $q_y$  in the last factor in Eq. (10) are defined similarly. Substitution of  $\alpha$  from Eq. (6) into Eq. (11) and integration of the resulting expression gives

$$I_{\alpha\alpha^*}(x; q_x) = 2\pi \frac{R_1 R_2}{k(R_1 + R_2)}. \quad (14)$$

The integral  $I_{\beta\beta^*}$  in Eq. (13) is

$$I_{\beta\beta^*}(x; q_x) = \frac{1}{\sigma \sqrt{\pi}} \int_{-a}^a e^{-ik(x-X)^2/2R_2} [q_x(X) - 1] dX \times \int_{-a}^a e^{ik(x-X')^2/2R_2} [q_x(X') - 1]^* dX' \times \int_{-\infty}^{\infty} e^{-ik(\xi-X)^2/2R_1} e^{ik(\xi-X')^2/2R_1} e^{-\xi^2/\sigma^2} d\xi. \quad (15)$$

Completion of the square in the exponent of the second integral and integration of the resulting expression<sup>12</sup> give Eq. (15) as

$$I_{\beta\beta^*}(x; q_x) = \int_{-a}^a e^{-ik(x-X)^2/2R_2 - ik(X^2/2R_1)} [q_x(X) - 1] dX \times \int_{-a}^a e^{ik(x-X')^2/2R_2 + ik(X'^2/2R_1)} \times [q_x(X') - 1]^* e^{-k^2\sigma^2(X-X')^2/4R_1 R_2} dX'.$$

From Eqs. (4) and (12), the quantity  $I_{\alpha\beta^*}$  is seen to be

$$I_{\alpha\beta^*}(x; q_x) = \frac{1}{\sigma} \sqrt{\frac{2R_1 R_2}{ik(R_1 + R_2)}} \int_{-a}^a e^{ik(x-X)^2/2R_2} [q_x(X) - 1]^* \times dX \int_{-\infty}^{\infty} e^{-ik(x-\xi)^2/2(R_1+R_2)} e^{ik(\xi-X)^2/2R_1 - \xi^2/\sigma^2} d\xi.$$

Completion of the square in the second integral and integration of the resulting expression<sup>12</sup> give Eq. (12) as

$$I_{\alpha\beta^*}(x; q_x) = \sqrt{\frac{2\pi R_1 R_2}{i\hat{\beta}k(R_1 + R_2)}} e^{-ik(x^2/2(R_1+R_2))\hat{\beta}} \times \int_{-a}^a e^{ik(x-X)^2/2R_2} [q_x(X) - 1]^* \times e^{ik(X^2/2R_1)\hat{\beta}} e^{-k^2\sigma^2(x-X)^2/4R_1(R_1+R_2)\hat{\beta}} dX,$$

where the parameter  $\hat{\beta}$  is defined as

$$\hat{\beta} = 1 - i \frac{k\sigma^2(R_2/R_1)}{2(R_1 + R_2)}.$$

By factoring  $I_{\alpha\alpha^*}(x; q_x)$  out of each term in Eq. (10) and placing it in the prefactor, we find the intensity becomes

$$I(x, y) = \frac{1}{(R_1 + R_2)^2} [1 + 2 \operatorname{Re} \hat{I}_{\alpha\beta^*}(x; q_x) + \hat{I}_{\beta\beta^*}(x; q_x)] \times [1 + 2 \operatorname{Re} \hat{I}_{\alpha\beta^*}(y; q_y) + \hat{I}_{\beta\beta^*}(y; q_y)], \quad (16)$$

where

$$\hat{I}_{\alpha\beta^*}(x; q_x) = \sqrt{\frac{k(R_1 + R_2)}{i2\pi\hat{\beta}R_1 R_2}} e^{-ik(x^2/2(R_1+R_2))\hat{\beta}} \int_{-a}^a e^{ik(x-X)^2/2R_2} \times [q_x(X) - 1]^* e^{ik(X^2/2R_1)\hat{\beta}} e^{-k^2\sigma^2(x-X)^2/4R_1(R_1+R_2)\hat{\beta}} dX, \quad \hat{I}_{\beta\beta^*}(x; q_x) = \frac{1}{2\pi} \frac{k(R_1 + R_2)}{R_1 R_2} \int_{-a}^a e^{-ik(x-X)^2/2R_2} e^{-ik(X^2/2R_1)} \times [q_x(X) - 1] dX \int_{-a}^a e^{ik(x-X')^2/2R_2} e^{ik(X'^2/2R_1)} \times [q_x(X') - 1]^* e^{-k^2\sigma^2(X-X')^2/4R_1 R_2} dX'.$$

Following specification of the transmission function for the object, the intensity at the image plane can be calculated from Eq. (16), which requires both single and double integrations over the transmission function.

### B. Point Source

The intensity at the image plane for a point source located a distance  $R_1$  from the object is found easily from Eq. (16) by taking the limit as  $\sigma$  approaches zero, which gives  $\hat{\beta} = 1$ . The intensity at the image plane for a point source  $I^P(x, y)$  is thus found to be

$$I^P(x, y) = \frac{1}{(R_1 + R_2)^2} [1 + 2 \operatorname{Re} \hat{I}_{\alpha\beta^*}^P(x; q_x) + \hat{I}_{\beta\beta^*}^P(x; q_x)] \times [1 + 2 \operatorname{Re} \hat{I}_{\alpha\beta^*}^P(y; q_y) + \hat{I}_{\beta\beta^*}^P(y; q_y)], \quad (17)$$

where

$$\hat{I}_{\alpha\beta^*}^P(x; q_x) = \sqrt{\frac{k(R_1 + R_2)}{i2\pi R_1 R_2}} e^{-ik(x^2/2(R_1 + R_2))} \int_{-a}^a e^{ik(x - X)^2/2R_2} \times [q_x(X) - 1]^* e^{ik(X^2/2R_1)} dX, \\ \hat{I}_{\beta\beta^*}^P(x; q_x) = \frac{k(R_1 + R_2)}{2\pi R_1 R_2} \left| \int_{-a}^a e^{-ik(x - X)^2/2R_2} e^{-ik(X^2/2R_1)} \times [q_x(X) - 1] dX \right|^2.$$

Since  $\hat{I}_{\alpha\beta^*}^P$  and  $\hat{I}_{\beta\beta^*}^P$  are related to each other, it is possible to write  $\hat{I}^P(x, y)$  in a form convenient for computation as

$$\hat{I}^P(x, y) = \frac{1}{(R_1 + R_2)^2} [1 + \hat{I}_{\alpha\beta^*}^P(x; q_x)|^2 + \hat{I}_{\alpha\beta^*}^P(y; q_y)|^2]. \quad (18)$$

### C. Large Source-to-Object Distance

When  $R_1$  becomes very large compared with  $R_2$ , the parameter  $\hat{\beta}$  can be approximated as

$$\hat{\beta} \approx 1 - i \frac{k\sigma^2}{2R_1} \left( \frac{R_2}{R_1} \right),$$

and the intensity at the image plane becomes

$$I^{PW}(x, y) = \frac{1}{R_1^2} [1 + 2 \operatorname{Re} \hat{I}_{\alpha\beta^*}^{PW}(x; q_x) + \hat{I}_{\beta\beta^*}^{PW}(x; q_x)] \times [1 + 2 \operatorname{Re} \hat{I}_{\alpha\beta^*}^{PW}(y; q_y) + \hat{I}_{\beta\beta^*}^{PW}(y; q_y)], \quad (19)$$

where

$$\hat{I}_{\alpha\beta^*}^{PW}(x; q_x) = \sqrt{\frac{k}{i2\pi\hat{\beta}R_2}} e^{-ik(x^2/2R_1\hat{\beta})} \int_{-a}^a e^{ik(x - X)^2/2R_2} \times [q_x(X) - 1]^* e^{ik(X^2/2R_1\hat{\beta})} e^{-k^2\sigma^2(x - X)^2/4R_1^2\hat{\beta}} dX, \\ \hat{I}_{\beta\beta^*}^{PW}(x; q_x) = \frac{1}{2\pi R_2} \int_{-a}^a e^{-ik(x - X)^2/2R_2} e^{-ik(X^2/2R_1)} \times [q_x(X) - 1] dX \int_{-a}^a e^{ik(x - X')^2/2R_2} e^{ik(X'^2/2R_1)} \times [q_x(X') - 1]^* e^{-k^2\sigma^2(X - X')^2/4R_1^2} dX'.$$

If  $R_1$  approaches infinity, the quantity  $\hat{\beta}$  becomes 1, and Eq. (19) reduces to an expression that describes a perfect plane wave.

### D. Weak Phase Objects

The functional form of Eq. (3) is somewhat restrictive. For a number of two-dimensional objects with rectangular symmetry, the transmission function describing the object is of the form

$$q(X, Y) = e^{i\phi_x(X)\phi_y(Y) - \mu_x(X)\mu_y(Y)}, \quad (20)$$

where  $\phi_x(X)$  and  $\mu_x(X)$  are the phase change and absorption of the x radiation as a function of the coordinate. Unfortunately, Eq. (20) does not separate as a product of the form  $q_x(X)q_y(Y)$ . However, for objects that produce weak phase changes and small absorption in the radiation beam, it is possible to approximate the factor  $q(X, Y)$ , as

$$q(X, Y) = 1 + \hat{f}_x(X)\hat{f}_y(Y)(i\delta kt - \mu_0 t/2),$$

where  $\hat{f}_x(X)$  and  $\hat{f}_y(Y)$  are dimensionless functions that describe the thickness of the object,  $\delta$  is the relative change in index of refraction between the object and the material in the surrounding body,  $t$  is a length parameter, and  $\mu_0$  is the intensity absorption coefficient<sup>11</sup> of the object. It is assumed that both the phase and the absorption can be written in terms of a single function.

By carrying out calculations analogous to those given above, it is possible to write the intensity on the image plane for weak phase and absorption objects as

$$I^W(x, y) = \frac{1}{(R_1 + R_2)^2} [1 + 2 \operatorname{Re}(-kt\delta + i\mu_0 t/2) \times \hat{I}_{\alpha\beta^*}^W(x; \hat{f}_x)\hat{I}_{\alpha\beta^*}^W(y; \hat{f}_y) + (k^2\delta^2 t^2 + \mu_0^2 t^2/4) \times \hat{I}_{\beta\beta^*}^W(x; \hat{f}_x)\hat{I}_{\beta\beta^*}^W(y; \hat{f}_y)], \quad (21)$$

where

$$\hat{I}_{\alpha\beta^*}^W(x; \hat{f}_x) = \sqrt{\frac{k(R_1 + R_2)}{2\pi\hat{\beta}R_1 R_2}} e^{-ikx^2/2(R_1 + R_2)\hat{\beta}} \int_{-a}^a \hat{f}_x^*(X) \times e^{ik(X^2/2R_1\hat{\beta}) + ik(x - X)^2/2R_2} e^{-k^2\sigma^2(x - X)^2/4R_1^2(R_1 + R_2)\hat{\beta}} dX, \\ \hat{I}_{\beta\beta^*}^W(x; \hat{f}_x) = \frac{1}{2\pi} \frac{k(R_1 + R_2)}{R_1 R_2} \int_{-a}^a \int_{-a}^a \hat{f}_x(X)\hat{f}_x^*(X') \times e^{-ik[X^2/2R_1 + (x - X)^2/2R_2] + ik[X'^2/2R_1 + (x - X')^2/2R_2] - k^2\sigma^2(X - X')^2/4R_1^2} \times dXdX'.$$

The corresponding quantities  $\hat{I}_{\alpha\beta^*}^W(x; \hat{f}_y)$  and  $\hat{I}_{\beta\beta^*}^W(x; \hat{f}_y)$  are determined by substitution of the function  $\hat{f}_y$  for  $\hat{f}_x$  in the above integrals. Note that the functions  $\hat{f}_x$  and  $\hat{f}_y$  are assumed to be zero outside the object whose outer dimensions are taken as  $\pm a$  and  $\pm b$ , in the  $x$  and  $y$  directions, respectively. To determine the intensity from a point source, Eq. (21) can be evaluated with  $\sigma = 0$  and  $\hat{\beta} = 1$ .



### 3. CALCULATED IMAGES

From Eq. (17) it is clear that, for objects with symmetry in the  $y$  direction,  $\hat{I}_{\alpha\beta}^P(y; q_y)$  must vanish because  $q_y(Y)=1$ . For the case of a wire of radius  $a$ , the transmission function is given by

$$q_x(X) = e^{2ik\delta a\sqrt{1-(X/a)^2} - \mu_0 a\sqrt{1-(X/a)^2}}, \quad (22)$$

where  $\delta$  is the real part of the index of refraction and  $\mu_0$  is the absorption coefficient of the wire. The results of calculations for a nylon line and a gold wire surrounded by a substance with  $q=1$  (which air approximates) are shown in Fig. 2. As can be seen in Fig. 2, the rapidity of the oscillations in intensity at the perimeter of the gold wire differs significantly from those of a material with a much lower index of refraction, such as nylon.

An example of an object whose transmission function is separable, as in Eq. (3), with the transmission functions in the  $X$  and  $Y$  directions given by equations of the form of Eq. (22), is a pair of crossed nylon lines. As in the case of the one-dimensional images of nylon, the high-frequency features seen in the point-source calculation are averaged to some extent when a source with nonvanishing dimensions is used; however, phase contrast still remains in the image, as shown in Fig. 3.

An example of an object whose phase function can be written as a product of two one-dimensional phase functions is a rectangle of dimensions  $a \times b$  and thickness  $t$ . The phase function is given by the product  $\phi(X)\phi(Y) = \delta t \hat{f}_x(X)\hat{f}_y(Y)$ , where  $\hat{f}_x(X) = u(X+a) - u(X-a)$ , where  $u$  is the Heaviside function. The function  $\hat{f}_y(Y)$  is defined similarly but with  $b$  replacing  $a$ . A pair of images calculated for a two-dimensional weak phase image are shown in Fig. 3.

A point to be noticed in calculating the image with Eq. (21) is that the use of only the first term in the expansion of the transmission function means that  $|q|^2$  is no longer unity. Hence, small errors are necessarily introduced in the calculated image.

### 4. EXPERIMENTS

The experimental apparatus used for recording phase-contrast images consists of a microfocus x-ray tube<sup>13</sup> (Oxford, Inc. Model UM-M1) and a Peltier effect cooled CCD camera (Roper Scientific, Model 7382-0001), which is configured with a fiber-optic bundle that views a fiber-optic scintillation to give an input-to-output image size ratio of unity. The magnification of the apparatus  $M$  at the image plane (the front surface of the fiber-optic scintillator) is given by  $M = (R_1 + R_2)/R_1$ . The CCD camera had a pixel

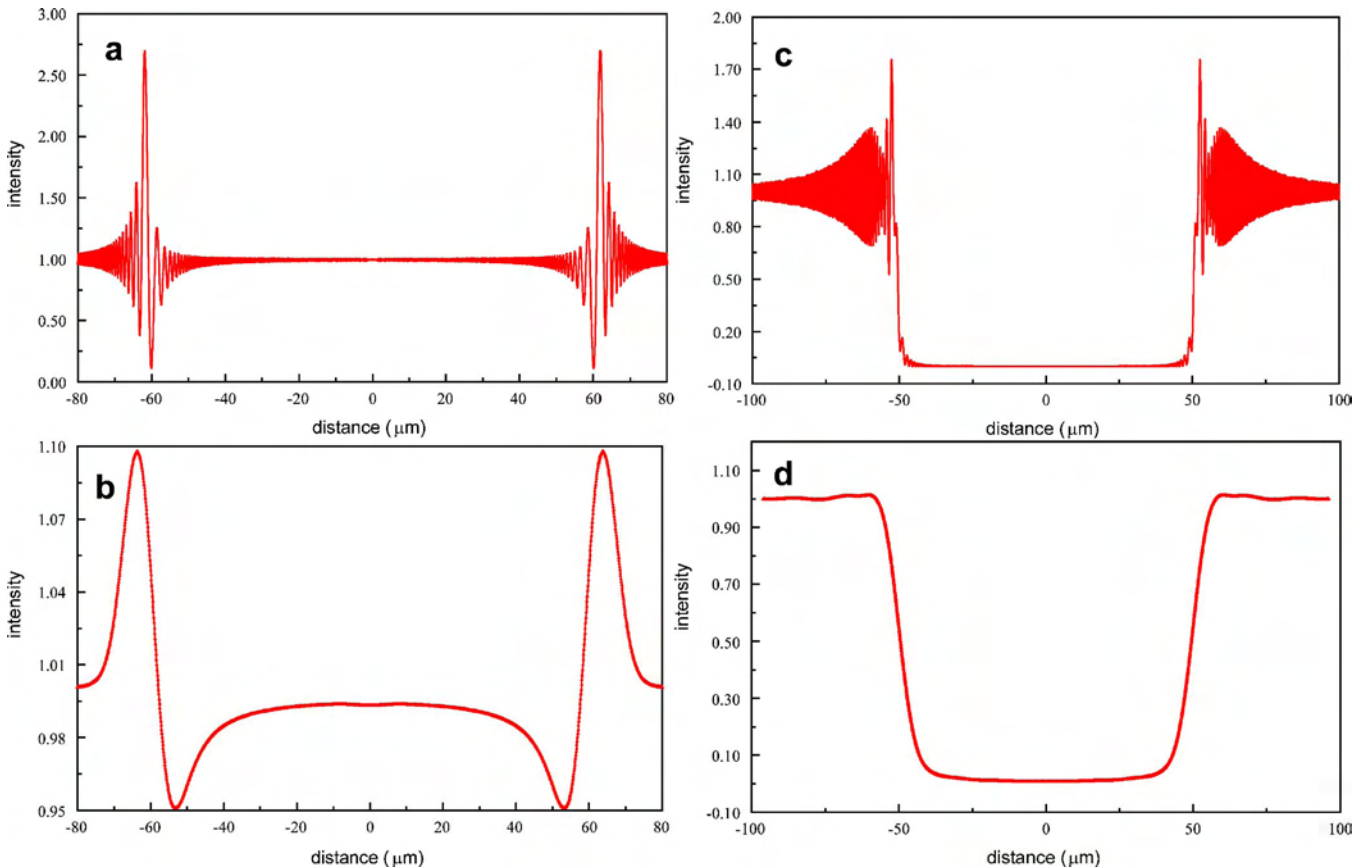


Fig. 2. (Color online) (left) x-ray phase-contrast images for a 60  $\mu\text{m}$  radius nylon line with  $R_1=0.2$  m,  $R_2=2.4$  m, and  $\lambda=41.3$  pm for (a) a point x-ray source from Eq. (18) and (b) a nonvanishing source with  $\sigma=6.75$   $\mu\text{m}$  from Eq. (16). The parameters describing the index of refraction of nylon are taken as  $\delta=1.0 \times 10^{-6}$  and  $\mu_0=0$ . (right) Calculated x-ray phase-contrast images for a 50  $\mu\text{m}$  radius gold wire with  $R_1=0.2$  m,  $R_2=2.4$  m, and  $\lambda=41.3$  pm for (c) a point x-ray source, from Eq. (18), and (d) a nonvanishing source with  $\sigma=6.75$   $\mu\text{m}$  from Eq. (16). The parameters describing the index of refraction of gold are taken as  $\delta=3.55 \times 10^{-6}$  and  $\mu_0=5.0 \times 10^4$   $\text{m}^{-1}$ .



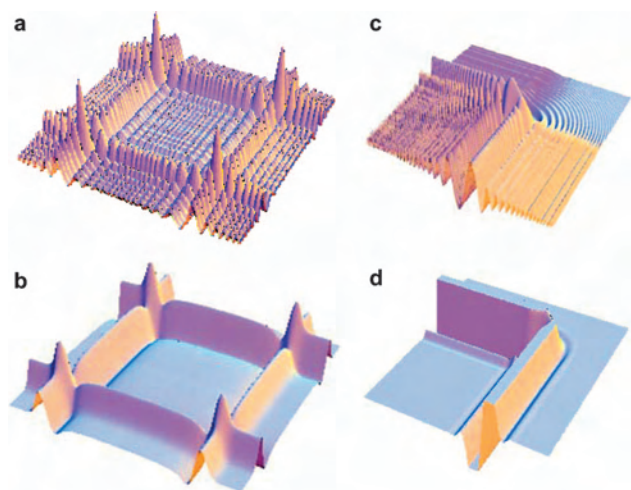


Fig. 3. Calculated x-ray phase-contrast images for a crossed pair of 120  $\mu\text{m}$  diameter nylon threads with  $R_1=0.2$  m,  $R_2=2.4$  m, and  $\lambda=41.3$  pm (a) for a point x-ray source, from Eq. (18), and (b) with a finite source size with  $\sigma=6.75$   $\mu\text{m}$  calculated using Eq. (16). The parameters  $\delta$  and  $\mu_0$  were taken to be  $1.0 \times 10^{-6}$  and 0, respectively. The maximum and minimum values of the intensity are (a) 6.34 and 0.01 and (b) 1.21 and 0.90. Calculated x-ray phase-contrast images for an 1.0  $\mu\text{m}$  thick Teflon square taken with  $R_1=1.3$  m,  $R_2=1.3$  m, and  $\lambda=41.3$  pm for (c) a point x-ray source from Eq. (21) evaluated with  $\sigma=0$ , and (d) a finite source size with  $\sigma=6.75$   $\mu\text{m}$  calculated using Eq. (21). The parameters  $\delta$  and  $\mu_0$  were taken as  $4.9 \times 10^{-7}$  and  $74.8$   $\text{m}^{-1}$ , respectively. The maximum and minimum values of the intensity are (c) 1.04 and 0.94 and (d) 1.01 and 0.98. The integration was carried out over a region 100  $\mu\text{m}$  by 100  $\mu\text{m}$  for both (c) and (d).

size of 15  $\mu\text{m} \times 15$   $\mu\text{m}$  and a field of view at the taper input of 50 mm  $\times$  50 mm. The x-ray source size, when the tube is operated at 90 kV, is specified by the manufacturer to have a full width at half-maximum of 14  $\mu\text{m}$ . The overall resolution of the phosphor screen, optics, and CCD camera was determined to be 120  $\mu\text{m}$  at the input of the phosphor screen by recording the intensity profile of a precision metal block and numerically differentiating the resulting intensity profile.

To simulate small density changes in an object with a simple geometry, a section of nylon line was imaged, and the results were compared with theory. The transmission function for the nylon line, which is taken to lie along the  $y$  axis, is

$$q_x(X) = e^{(2ik\delta - \mu_0)2a\sqrt{1-(X/a)^2}} \quad \text{for } |X| \leq a, \quad (23)$$

where  $\delta$  is the real component of the index of refraction and  $\mu_0$  is the absorption coefficient. Since there are no variations in transmission in the  $y$  direction, the transmission function  $g_y$  is unity. It follows that the second factor in brackets in Eq. (7) reduces to unity so that, as expected, there is contrast only in the  $x$  direction, as can be seen in the calculated image in Fig. 4.

An example of a material with a relatively large magnitude of  $\delta$  that would correspond to perhaps the limiting case of strong variations in tissue density, or possibly to a contrast agent, is gold. The images in Fig. 4 show the results of imaging a gold wire (having a circular cross sec-

tion) with the x-ray apparatus. Both the theoretical and the experimental images include absorption, which dominates the contrast.

A pair of identical nylon lines crossed at 90°, whose phase-contrast image is shown in Fig. 5, provides a test case for comparison of Eq. (16) with experiment. Transmission functions of the form given by Eq. (23) were used for both  $q_x$  and  $q_y$ . Since the calculations for the factors in brackets in Eq. (16) in the  $x$  and  $y$  directions are identical for this example, it is possible to save a factor of 2 in computation time.

An example of an object whose phase functions separate in Cartesian coordinates is a rectangle with a thickness  $t$ . The transmission function for the rectangle can be written as

$$q(X, Y) = e^{i\phi_x(X)\phi_y(Y) - \mu_x(X)\mu_y(Y)},$$

where  $\phi_x(X) = kt[u(X+a) - u(X-a)]$  and  $\phi_y(Y) = kt[u(Y+a) - u(Y-a)]$ , where  $u$  is the Heaviside function. The intensity at the image plane  $I^W(x, y)$  for the case of a weak phase object can be calculated for a point source and for a source with a Gaussian intensity distribution. Figure 5 shows the results of a numerical calculation and an experiment with a thin sheet of Teflon. At 30 kV, Teflon has an index of refraction and an absorption coefficient of the same order as that of soft tissue. Since the object has rectangular symmetry, only the image of one corner is shown.

## 5. DISCUSSION

The calculated phase-contrast images shown here have been carried out with x-ray wavelength and distance parameters  $R_1$  and  $R_2$  that give significant image magnification and take advantage of the high resolution of the method, as would be desirable in the imaging of biological samples. The magnification  $M$ , defined as  $M = (R_1 + R_2)/R_1$ , used in the calculations given here is 13. The expressions for the intensity given here reduce to the one-dimensional expressions in Ref. 3 and give the same oscillatory features in the image when values of  $R_1$  and  $R_2$  that give  $M$  near unity are chosen. The oscillatory features in the intensity distribution of the phase-contrast images seen in the calculations in Ref. 3 are not present in the images found here primarily as a result of the use of different values of  $R_1$  and  $R_2$ . Of note in both the calculations and the experiment with crossed nylon wires, as shown in Figs. 5(a) and 5(b), is the appearance of a dark spot at the center of the image that arises from the curvature of the wires.

The qualitative difference between the images of the gold and nylon wires shown here comes as a result of the relative rapidity of the variations in intensity at the perimeter of the gold wire. When an image is computed for a gold wire without absorption and using a perfect point source for the x radiation, rapid oscillations in intensity are found at the perimeter of the wire. The appearance of the gold wire in Fig. 4 without the typical phase-contrast features seen with the nylon line is a result of the relative rapidity of the intensity oscillations, which, after averaging over the finite extent of the x-ray source, results in visible phase-contrast features in the case of the nylon and virtually none in the case of the gold. Strong absorp-

tion is an additional factor in eliminating phase-contrast features, as in the case of gold.

There has been little discussion of the practical utility of considering the transmission function  $q(X, Y)$  as a product, that is, where  $q(X, Y) = q(X)q(Y)$ . Despite the obvious simplification in writing  $q$  in such a form for mathematical calculations, this separation appears to restrict its applicability to objects that extend to infinity in both directions, excluding common, closed geometry objects. Ultimately, a separation where the phase functions appear as products, but which requires the weak phase approximation, is more useful for practical application.

An important conclusion of the work presented here is that, with the source sizes of common, contemporary microfocus x-ray tubes, the utility of recording phase-contrast features in images is greatest when small density changes with large density gradients or, equivalently, small changes in  $\delta$  with strong gradients in  $\delta$  are present. While the high resolution of a phase-contrast imaging apparatus may be of value for detecting objects with large differences in the values of  $\delta$  and  $\mu_0$  such as gold or other metals in a body where  $\delta$  and  $\mu_0$  are small, the unique features of phase-contrast imaging appear to be brought out in imaging objects with small variations in  $\delta$  such as biological tissue.

It can be seen from the form of the integrands in Eq. (16) that the images can be scaled to the dimensions of

the object, such as the radius  $a$  in the examples of the wires presented here. Thus, images can be calculated as a function of a universal parameter,  $x/a$ , so that the integrations extend only over the range  $-1$  to  $1$ . Unfortunately, the use of such a dimensionless parameter also means that the distance parameters  $R_1$  and  $R_2$  become scaled and describe different experimental arrangements of the source-to-object and object-to-image distances.

A point to be noted in the present calculations relative to those where the effects of a nonvanishing source are treated through use of Fourier transform methods<sup>1,5,15</sup> is that for objects where the weak phase approximation is not valid the intensity given by Eq. (16) requires integration over the phase function evaluated in coordinate space; the Fourier transform method requires a two-dimensional Fourier transformation of the phase function,<sup>16</sup> which in some cases can prove to be problematic. For those cases where a weak phase object is of interest, the use of Fourier transform methods may be preferable to the use of Eq. (21).

As has been shown previously in the experimental images in Ref. 2, phase-contrast features taken with a nonvanishing source in a geometry that has a sizeable magnification tend to appear in the image as dark and bright features at the perimeters of objects as a result of deflection of the x radiation by strong density gradients, even when polychromatic radiation is used. The calculations

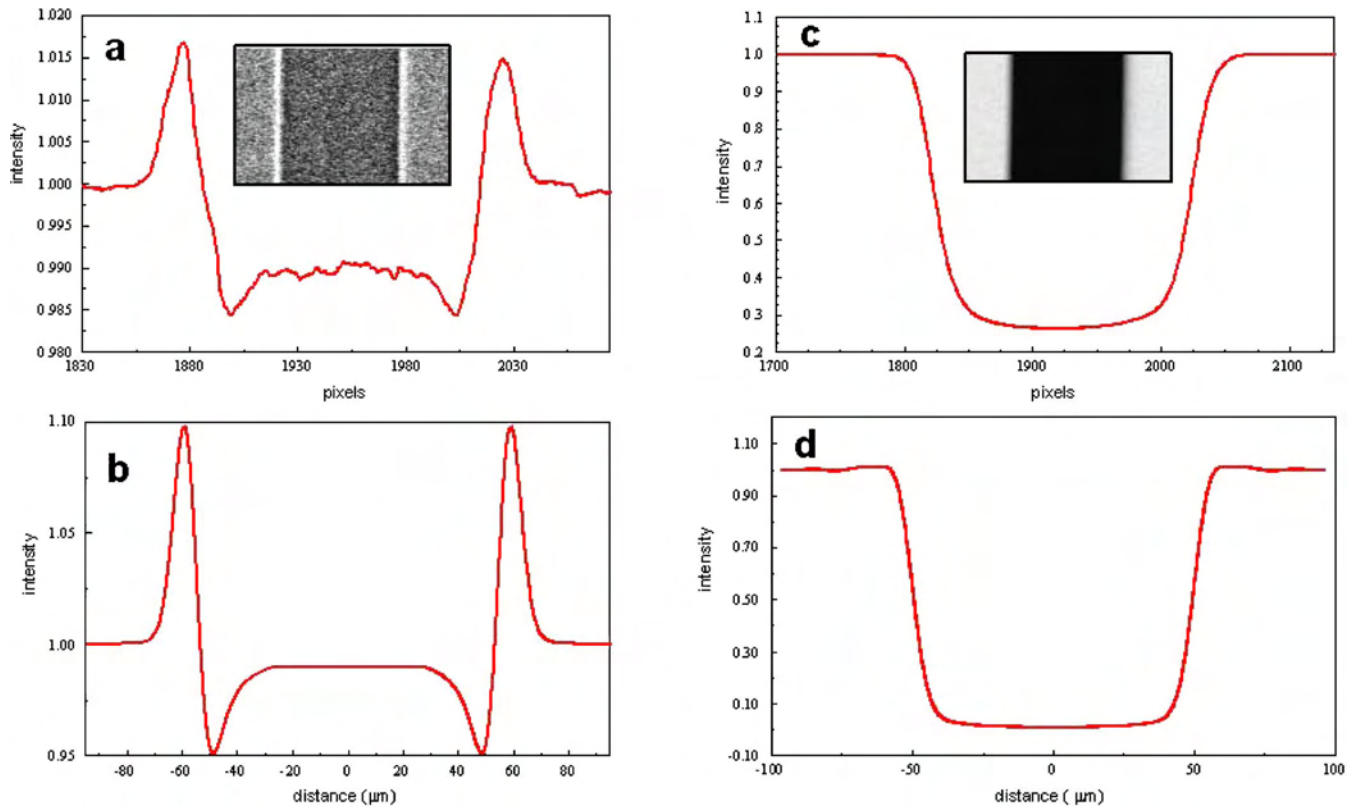


Fig. 4. (Color online) (left) (a) Intensity versus distance for a phase-contrast image of a 120  $\mu\text{m}$  diameter nylon line taken from a CCD image. The imaging parameters are  $R_1=0.18$  m and  $R_2=2.42$  m, with the x-ray tube operating for 3 min at 90 kV and 100  $\mu\text{A}$ . (b) Intensity versus distance for a nylon line calculated from Eq. (16) with  $\lambda=41$  pm,  $R_1=0.2$  m,  $R_2=2.4$  m,  $\sigma=6.75$   $\mu\text{m}$ , and  $\mu_0=0$ . Inset: section of an experimental CCD image used to determine the curve in (a). (right) (c) Intensity versus distance for a phase-contrast image of a 100  $\mu\text{m}$  diameter gold wire taken from a CCD image taken with  $R_1=0.18$  m and  $R_2=2.42$  m, with the x-ray tube operating for 3 min at 90 kV and 100  $\mu\text{A}$ , and (d) as calculated from Eq. (16) with  $\lambda=41$  pm,  $R_1=0.2$  m,  $R_2=2.4$  m,  $\sigma=6.75$   $\mu\text{m}$ , and  $\mu_0=50 \times 10^3$   $\text{m}^{-1}$ . Inset: section of a CCD image used to generate the curve in (c).

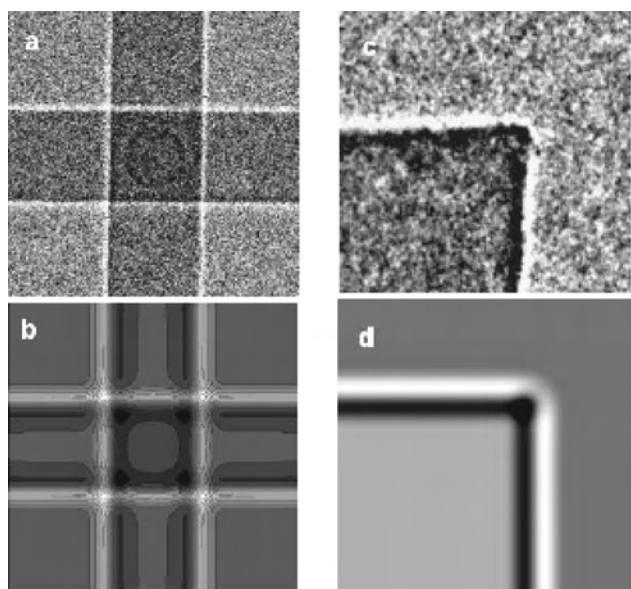


Fig. 5. (a) CCD image of a pair of crossed  $100\text{ }\mu\text{m}$  diameter nylon lines taken with  $R_1=0.18\text{ m}$  and  $R_2=2.42\text{ m}$  and with the x-ray tube operating for 3 min at 90 kV and  $100\text{ }\mu\text{A}$ . (b) A contour plot of the nylon lines calculated from Eq. (16) with  $\lambda=41\text{ pm}$ ,  $R_1=0.2\text{ m}$ ,  $R_2=2.4\text{ m}$ ,  $\sigma=6.75\text{ }\mu\text{m}$ , and  $\mu_0=0$ . (c) Intensity versus distance taken from a CCD image of a 1 cm long section of an  $80\text{ }\mu\text{m}$  thick Teflon rectangle with  $R_1=0.2\text{ m}$  and  $R_2=2.4\text{ m}$  and with the x-ray tube operating for 3 min at 90 kV and  $100\text{ }\mu\text{A}$ . (d) A contour plot of the corner calculated from Eq. (16) with  $\lambda=41\text{ pm}$ ,  $R_1=0.2\text{ m}$ ,  $R_2=2.4\text{ m}$ ,  $\sigma=6.75\text{ }\mu\text{m}$ ,  $\delta=1\times 10^{-6}$ , and  $\mu_0=0$ .

with the one- and two-dimensional objects given here show precisely this feature and point to the capabilities of x-ray phase-contrast imaging as a way of enhancing the diagnostic capabilities of x-ray imaging in general.

## ACKNOWLEDGMENTS

Authors G. J. Diebold, T. J. Hamilton, and G. Cao and G. J. Diebold and C. Rose-Petruck are grateful for the support of this research by the U.S. Army Medical Research and Material Command under grants DAMD17-02-1-0307 and W81XWH-04-1-0481, respectively. Opinions, interpretations, conclusions, and recommendations are those of the authors and are not necessarily endorsed by the U.S. Army.

Corresponding author G. J. Diebold can be reached by e-mail at Gerald-Diebold@Brown.edu.

## REFERENCES AND NOTES

1. P. Cloetens, R. Barrett, J. Baruchel, J.-P. Guigay, and M. Schlenker, "Phase objects in synchrotron radiation hard x-ray imaging," *J. Phys. D* **29**, 133–146 (1996).
2. S. W. Wilkins, T. Gureyev, D. Gao, A. Pogany, and A. W. Stevenson, "Phase-contrast imaging using polychromatic hard x-rays," *Nature* **384**, 335–338 (1996).
3. F. Arfelli, M. Assante, V. Bonvicini, A. Bravin, G. Cantatore, E. Castelli, L. D. Palma, M. DiMichiel, R. Longo, A. Olivo, S. Pani, D. Pontoni, P. Poropat, M. Prest, A. Rashevsky, G. Tromba, A. Vacchi, E. Vallazza, and F. Zanconati, "Low-dose phase contrast x-ray medical imaging," *Phys. Med. Biol.* **43**, 2845–2852 (1998).
4. P. Cloetens, W. Ludwig, J. Baruchel, D. V. Dyck, J. V. Landuyt, J. P. Guigay, and M. Schlenker, "Holotomography: quantitative phase tomography with micrometer resolution using hard synchrotron radiation x rays," *Appl. Phys. Lett.* **75**, 2912–2914 (1999).
5. S. Zabner, P. Cloetens, J. P. Guigay, and J. Baruchel, "Optimization of phase contrast imaging using hard x-rays," *Rev. Sci. Instrum.* **76**, 073705 (2005).
6. M. Born and E. Wolf, *Principles of Optics* (Pergamon, 1980).
7. A. Pogany, D. Gao, and S. Wilkins, "Contrast and resolution in imaging with a microfocus x-ray source," *Rev. Sci. Instrum.* **68**, 2774–2782 (1997).
8. J. M. Cowley, *Diffraction Physics* (North-Holland, 1984). The use of the Fresnel and the small-angle approximations require that parameters of the form  $(x-X)^2/R$  be small compared with unity; hence, in experiments, the coordinates of the object and the image should be restricted to small distances from the axis of propagation of the x radiation.
9. M. V. Klein, *Optics* (Wiley, 1970).
10. The electric field is taken as proportional to  $1/r$ . The intensity is expressed in units where the dielectric constant and permittivity are taken as unity so that the intensity becomes proportional to  $1/r^2$ .
11. We use the convention used in Ref. 7 where the field is attenuated proportional to  $\exp[-\mu(z)]$ . The intensity therefore is attenuated as  $\exp[-2\mu(z)]$ . The parameter  $\mu_0$  is taken as an intensity absorption coefficient.
12. I. S. Gradshteyn and I. M. Ryzhik, *Table of Integrals, Series, and Products*, 4th ed. (Academic, 1965).
13. The spectrum of the x-ray tube, which uses only a Be window, can be found in Ref. 14, p. 99.
14. J. Bushberg, J. Seibert, and E. Leidholdt, Jr., *The Essential Physics of Medical Imaging* (Williams and Wilkins, 1994).
15. B. D. Arhatari, A. P. Mancuso, A. G. Peele, and D. A. Nugent, "Phase contrast radiography: image modeling and optimization," *Rev. Sci. Instrum.* **75**, 5271–5276 (2004).
16. For objects where the weak phase approximation is not applicable, Fourier transformation (with respect to  $\eta$ ) of functions of the form  $\exp[i\phi(\eta+\lambda Df/2)]$ , where  $D$  is a length parameter and  $f$  is spatial frequency, is required to determine the intensity in the frequency domain; that is, for each value of  $f$  in the frequency domain, a Fourier transformation with respect to  $\eta$  must first be carried out. See Appendix A2 in Ref. 1.

# ULTRASONICALLY MODULATED X-RAY PHASE CONTRAST IMAGING

*Theron J. Hamilton, Guohua Cao, Claude J. Bailat,  
Jack Wands\*, Stephan Gehring\*, Christoph Rose-Petruck, and Gerald J. Diebold*

Brown University  
Department of Chemistry and Medical School Liver Research Center\*  
Providence, RI, USA, 02912

## ABSTRACT

We show that the radiation pressure exerted by a beam of ultrasound can be used for contrast enhancement in high resolution x-ray imaging of tissue. Interfacial features of objects are highlighted as a result of both the displacement introduced by the ultrasound and the inherent sensitivity of x-ray phase contrast imaging to density variations. The potential of the method is demonstrated by imaging various tumor phantoms and tumors from mice. The directionality of the acoustic radiation force and its localization in space permits the imaging of ultrasound-selected tissue volumes. The results suggest that the method may permit the detection of tumors in soft tissue in their early stages of development.

## 1. I. INTRODUCTION

The in-line phase contrast method of x-ray image formation[1, 2, 3] employs an x-ray source and image recording device, between which is interposed the body of interest. The similarity between conventional Roentgen shadowgraphy and phase contrast imaging, is apparent; however, the critical difference between the two modalities is the degree of lateral coherence of the beam generated by the x-ray source used in phase contrast imaging. In phase contrast imaging, it is the high spatial coherence of the source that permits detection of the small deflections that x-rays undergo in passing through the body which give rise to the interference pattern seen in the image. Phase contrast is produced in conventional radiography, however, the comparatively large size of the x-ray source results in an averaging of phase contrast features in the image so that they are no longer visible.

An important facet of phase contrast imaging that describes its qualitative features[3] is that, for a plane wave source, the contrast in the image can be written as

$$I(x) = 1 + \frac{\lambda z}{2\pi} \phi''(x) \quad (1)$$

where  $z$  is the object to image distance. That is, for a weak phase object, in the limit  $\pi \lambda u^2 \ll 1$ , where  $u$  is the spatial frequency, the contrast in the image is proportional to the

second space derivative of the phase function,  $\phi''(x)$  and that it increases linearly with an increase with  $z$ . A second important feature of phase contrast imaging[1], which is evidenced by Eq. 1, is the weak dependence of image formation on wavelength—images can be made using polychromatic x-radiation.

Acoustic radiation pressure can be used to enhance phase contrast in an image by creating displacement of objects within a body that have different sound speeds or densities from that of the bulk[4, 5]. The method is implemented by first recording a conventional phase contrast image of the body, which is stored in a computer. Next, the body is irradiated with a directed beam of ultrasound and a second image is taken. The two images are then subtracted pixel by pixel to give the acoustically modulated phase contrast image. The effect of the acoustic radiation force is to act to displace objects that have different sound speeds or densities from that of their surroundings an amount proportional to the square of the acoustic pressure. An image formed in this manner has highlighted phase contrast features and virtually no absorption contrast features.

The acoustic modulation of phase contrast images described here is related to elastographic imaging, where tissue movement is monitored in response to acoustic radiation or externally applied mechanical pressure. Work in this field have shown that variations in Young's modulus, which, in part, determines sound speed, permits acoustic differentiation of tissue[6][7][8]. It is known, for instance, that breast tumors have a significantly different Young's modulus from surrounding tissue, and that tumors move as rigid bodies in response to acoustic radiation pressure[9][10]. Thus, the response of a tumor to mechanical force can be used to provide a marker for specific tissue characteristics. In the method we present here, maximum phase contrast in the subtracted image is found when the displacement of the object is approximately equal to the width of a single x-ray fringe in the image.

Here, we report experiments using a microfocus x-ray tube and a CCD camera to record acoustically modulated x-ray phase contrast images. The rudiments of the theory of phase contrast image formation is given in Section II. Section III



describes experiments and Section IV discusses the method.

## 2. II. THEORY OF IMAGE FORMATION

The transverse coherence length  $d_{\perp}$  of radiation with a wavelength  $\lambda$  generated by a near point source of radiation with a source diameter  $\sigma$  recorded at a distance  $l$  from the source is given by

$$d_{\perp} = \frac{\lambda l}{\sigma}.$$

In practice, to achieve a high degree of lateral coherence it is essential to design the x-ray tube with a small source diameter. The resolution in the imaging forming device must be commensurate with dimensions of the phase contrast fringes, which constitutes a second requirement for observation of phase contrast in the image, but which can be overcome using several different contemporary image recording devices.

The complex index of refraction of a body  $n$  can be written

$$n = 1 - \delta + i\beta$$

where  $\delta$  is the real part of the index of refraction that accounts for phase contrast in the image, and  $\beta$  is the imaginary component of the index of refraction that governs absorption. Detailed expressions for both  $\delta$  and  $\beta$  show that both quantities are proportional to the density. The theory of phase contrast imaging is straightforward and is based on the Fresnell-Kirchhoff integral formulation of wave propagation[11]. In one dimension, the intensity  $I(x)$  recorded at the image plane is given by the square of the absolute value of the electric field  $f(x)$ , that is,

$$I(x) = |f(x)|^2 \quad (2)$$

where the field for a point source placed at the origin is given by

$$f(x) = \left( \frac{i}{\lambda R_1 R_2} \right)^{1/2} e^{-ikR_2} \int e^{-ik\frac{x}{2R_1}} q(X) e^{-ik\frac{(x-X)^2}{2R_2}} dX$$

where, as shown in Fig. 1  $R_1$  is the source to object distance,  $R_2$  is the object to image distance,  $k$  is the wavenumber of the radiation, and  $q(X)$  is the phase function at the plane of the object. The phase function includes the effects of both phase changes in the body of interest as well as absorption and can be expressed as

$$q(\xi) = e^{i\phi(\xi) - \mu(\xi)}$$

where  $\phi$  is the phase change undergone by the x-radiation as it passes through the body, and  $\mu$  is the absorption. The phase, in turn, is related to the real part of the index of refraction through

$$\phi(z) = -k \int_z \delta(z') dz'$$

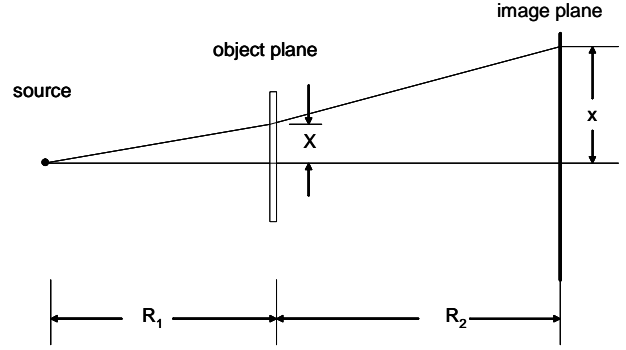


**Fig. 1.** Schematic diagram for x-ray phase contrast imaging. The source is taken to be a perfect point source in the calculation of the one-dimensional image.

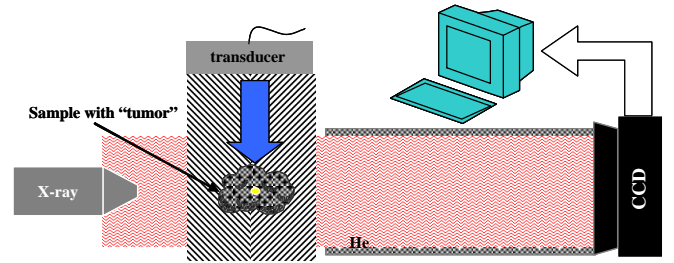


**Fig. 2.** Diagram of the apparatus. A He atmosphere in the x-ray path reduces x-ray scatter.

where the integration is along the path of the x-radiation which is taken as the  $z$  direction. By manipulation of Eq. 2, the intensity, written without factors common to both the constant and modulated terms  $\hat{I}(x)$ , can be written

$$\hat{I}(x) = |1 + A(x)|^2 \quad (3)$$

where

$$A(x) = \sqrt{\frac{i(R_1 + R_2)}{\lambda R_1 R_2}} e^{\frac{ikx^2}{2(R_1 + R_2)}} \int_{-a}^a e^{-ik\left[\frac{X^2}{2R_1} + \frac{(x-X)^2}{2R_2}\right]} [q(X) - 1] dX.$$

The integration specified for  $A(x)$  in Eq. 3 is carried out over the object; that is, the phase function  $q$  is taken to be unity outside the body of interest.

## 3. III. EXPERIMENTS

The apparatus used in these experiments consists of a micro-focus x-ray tube (Oxford, Inc. Model UM-M1), and a liquid nitrogen cooled CCD camera (Roper Scientific, Model 7382-0001) with a pixel size of 19  $\mu\text{m}$ . The CCD viewed a *CsI*

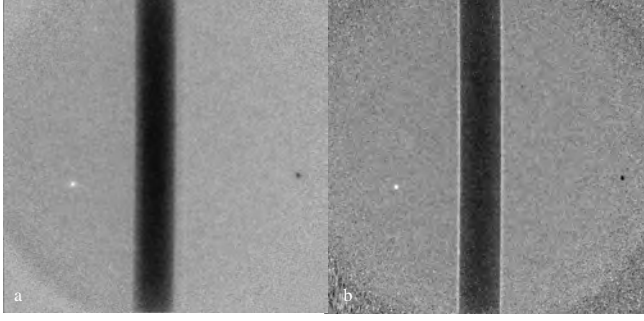


**Fig. 3.** (a) Image of a 300  $\mu\text{m}$  nylon line, surrounded by ambient air, taken with the x-ray tube operating with large source size. (b) Image of the same 300  $\mu\text{m}$  nylon line taken with the source diameter on the x-ray tube approximately 15  $\mu\text{m}$ . Phase contrast is visible in (b) which appears as bright features at the perimeter of the line.

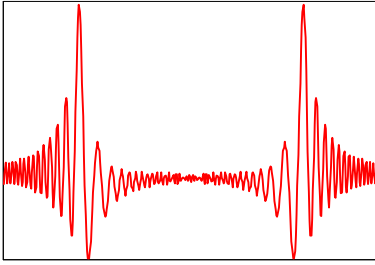


**Fig. 4.** Typical phase contrast intensity pattern for a nylon line calculated from Eq. 3. Absorption was not included in the calculation so the effects of phase contrast alone are shown.

fiber optic plate (Hamamatsu Model J6676) through a . As shown in Fig 2, the acoustic radiation is directed perpendicularly to the line of travel of the x-radiation. The acoustic radiation was generated by amplifying a 1.14 MHz sinusoidal wave in a power amplifier (Ritec, Inc. Model GA2500) whose output was fed to a  $\text{LiNbO}_3$  ultrasonic transducer attached to the sample.

The images shown in Fig. 3, both taken without the application of ultrasound, show the effect of the source size of the x-radiation on the image; only (b) taken with a small source size shows phase contrast features. The geometrical parameters were  $R_1 = 0.35 \text{ m}$ , and  $R_2 = 2.25 \text{ m}$  so that there is a magnification of 7.4 in the image. The x-ray tube was operated at a voltage 90 keV, and a current of 100  $\mu\text{A}$ . The exposure time for each image was 15 s.

A calculation of the phase contrast in the image was carried out using Eq. 3 using a value for  $\delta$  of  $3.276 \times 10^{-8}$  and

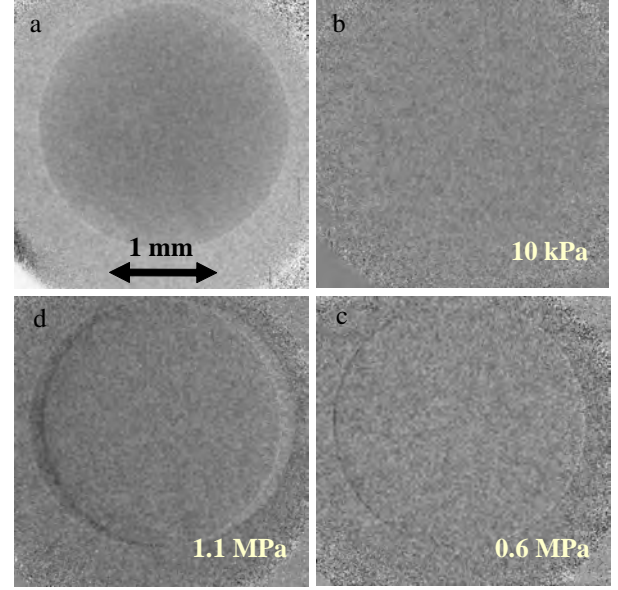


**Fig. 5.** (a) Phase contrast image of a 3 mm diameter Teflon sphere surrounded by water. (b)-(d) Acoustically modulated phase contrast image with successively higher intensities of acoustic radiation.

$\lambda$  of  $0.138 \times 10^{-10} \text{ m}$  and using the expression

$$\phi(\xi) = -2k\delta\sqrt{a^2 - \xi^2},$$

for the phase function, which pertains to a cylindrical geometry. No account is taken of the polychromaticity of the radiation, which would be expected in an experiment. The results of the calculation are shown in Fig. 4.

Experiments were done to demonstrate acoustic modulation of phase contrast images. The images shown in Fig. 5 show the effect of increasing acoustic radiation pressure on a Teflon sphere suspended in water by a fine glass fiber. The acoustic radiation consisted of 15  $\mu\text{s}$  bursts of radiation applied at a repetition frequency of 133 kHz.

An acoustically modulated phase contrast of a mouse skin tumor is shown in Fig. 6. The tissue sample is held in place by a thin plastic tube which also serves as a conduit for the ultrasound. The fine features in the subtracted image show how tissue with different elastic moduli move differentially in response to ultrasonic radiation pressure and highlight phase contrast in the image while the absorption seen in a conventional phase contrast image is almost totally eliminated.

#### 4. IV. DISCUSSION

The salient feature of x-ray phase contrast imaging as it is applied to soft tissue is its response to changes in density. Although the calculated phase contrast images show characteristic high frequency oscillations at the perimeter of objects with



**Fig. 6.** Subtracted phase contrast image.

density different from their surrounding arising from phase contrast, the experimental images presented here do not appear with such clarity. The heightened intensity at the edges of the nylon line in the experimental image comes as a result of averaging of the intensity oscillations predicted by theory for a perfect point source by the finite source diameter of the x-ray tube. Despite the averaging, distinct features on short length scale are clearly evident in the x-ray images.

A perhaps unique feature of the acoustic method discussed here is the vector character of the image. The acoustic radiation pressure is directional so that the subtracted image has a response only in the direction of the ultrasonic radiation force. The unique features of the method described here including high resolution, response to changes in elasticity parameters, and response to rapid variations in density at the edges of objects give acoustically modulated phase contrast imaging some possibility of tumor detection over conventional x-ray mammography.

## 5. ACKNOWLEDGEMENT

The authors GJD, TJH, GC, and CJB, are grateful for the support of this research by the US Army Medical Research and Materiel Command under grant DAMD17-02-1-0307; and GJD and CRP under grant W81XWH-04-1-0481.

## 6. REFERENCES

- [1] S.W. Wilkins, T.E. Gureyev, D. Gao, A. Pogany, and A. W. Stevenson, ,” *Nature*, vol. 384, pp. 335, 1996.
- [2] A. Momose, ,” *Instruments & Methods in Physics Research, Section A*, vol. 352, pp. 622, 1995.
- [3] A. Pogany, D. Gao, and S.W. Wilkins, ,” *Rev. Sci. Instr.*, vol. 68, pp. 2774, 1997.

- [4] T. J. Hamilton, C. J. Bailat, C. Rose-Petruck, and G. J. Diebold, ,” *Phys. med. Biol.*, vol. 49, pp. 4985, 2004.
- [5] C. J. Bailat, T. J. Hamilton, C. Rose-Petruck, and G. J. Diebold, ,” *Appl. Phys. Lett.*, vol. 85, pp. 4517, 2004.
- [6] L. Gao, K.J. Parker, R.M. Lerner, and S.F. Levinson, ,” *Ultrasound Med. Biol.*, vol. 22, pp. 959, 1996.
- [7] K. Nightingale, R. Nightingale, M. Palmeri, and G. Trahey, ,” *IEEE Ultrasonics Symp.*, p. 1319, 1999.
- [8] K. Nightingale, D. Stutz, R. Bentley, and G. Trahey, ,” *IEEE Symp.*, p. 525, 2002.
- [9] A.P. Sarvazyan, ,” *Ultrasound in Medicine and Biology*, vol. 24, pp. 1419, 1998.
- [10] S.A. McAleavey, ,” *IEEE Transactions UFFC*, vol. 50, pp. 631, 2003.
- [11] Miles V. Klein, *Optics*, John Wiley & Sons, Inc., 1970.

# **X-ray Phase Contrast Imaging: Transmission Functions Separable in Cylindrical Coordinates**

Guohua Cao<sup>1</sup>, Theron Hamilton<sup>1</sup>, Christopher M. Laperle<sup>2</sup>,

Christoph Rose-Petruck,<sup>1</sup> and Gerald J. Diebold<sup>1\*</sup>

<sup>1</sup>*Department of Chemistry and* <sup>2</sup>*The Liver Research Center,*

*RI Hospital and Warren Alpert Medical School,*

*Brown University, Providence, RI, USA, 02912*

A Fresnel-Kirchhoff integral can be used to calculate x-ray phase contrast images when the transmission function is known. Here expressions for image intensity are derived for objects with axial symmetry for an x-ray source with non-vanishing dimensions. An expression for the image intensity is given for an x-ray source whose intensity distribution is described by a Gaussian function, from which an expression for the limiting case of a point source of radiation is found. The expressions for image intensity are evaluated for cases where the magnification is substantially greater than one, as would be employed in biological imaging. Experiments using a micro-focus x-ray tube and CCD camera are reported to determine the capability of the method for imaging small spherical objects, such as gold particles, which might find application as contrast agents in biomedical imaging.

## **Introduction**

The appeal of the x-ray in-line phase contrast method[1, 2] for soft tissue imaging lies in its strong contrast for rapid variations in density which appear in the image as bright and dark outlines at the perimeters of objects. The in-line method is sensitive to absorption so that the image contains features both from absorption contrast, as in a conventional x-ray shadograph,

---

\*Electronic address: [Gerald\Diebold@Brown.edu](mailto:Gerald\Diebold@Brown.edu)



and phase contrast as well. If absorption contrast is not of primary interest, since the method relies on the deflection of x-radiation rather than their absorption, it is possible to employ hard, weakly absorbed x-radiation providing a significantly lower absorbed radiation dose than that in conventional x-ray shadowgraphy. In order to produce phase contrast in an image, the x-ray source must have a high degree of spatial coherence, hence, x-ray synchrotrons[3–5] or microfocus x-ray tubes[6–8] are typically used as radiation sources. A further feature of employment of sources with high spatial coherence, in addition to the benefit of phase contrast in the image, is that if the image recording device is chosen to have high resolution, the obvious advantage of high spatial resolution also becomes characteristic of the method adding to its overall utility as an imaging diagnostic.

From a knowledge of the transmission function  $q(X, Y)$ , where  $X$  and  $Y$  are the coordinates on the object perpendicular to the propagation direction of the radiation[8], the image produced with the in-line method can be determined from a Fresnel-Kirchhoff integral[9, 10]. Here, we derive expressions for in-line phase contrast imaging using a Fresnel-Kirchhoff integral for objects with cylindrical symmetry referred to the propagation direction of the x-radiation, that is, where the phase function for the object to be imaged can be expressed as a function of a radial coordinate  $R$  only. The derivation in Section I gives the electric field for a source with an arbitrary intensity distribution. Section II gives an expression for the image plane intensity for a Gaussian source intensity distribution. Section III gives limiting expressions for the image intensity for a point source, and for the limiting case of a large source-to-object distance. Experiments carried out with the goal of determining the capability of phase contrast imaging for detecting spherical objects are reported in Section IV. The work presented here focuses on imaging where the magnification of the object and the resolution are appropriate for detection of small density variations in biological specimens.

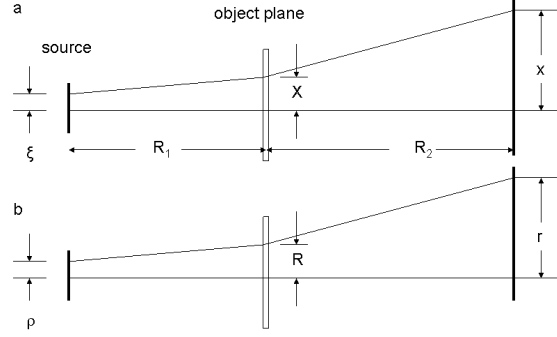


FIG. 1: Schematic drawing of the coordinates used in the evaluation of the Fresnel-Kirchhoff integral for phase contrast imaging with a non-vanishing, circularly symmetric source. The object and source are taken as lying in a line along the normal to the image plane. In (a) the Cartesian coordinates on the source, object, and image planes are denoted  $(\xi, \eta)$ ,  $(X, Y)$ , and  $(x, y)$ , respectively; in (b) the radial coordinates are denoted  $(\rho, \theta)$ ,  $(R, \Phi)$ , and  $(r, \phi)$ , respectively.

### I. ELECTRIC FIELD AT THE IMAGE PLANE

The electric field  $f$  at the image plane for an x-ray source of unit electric field amplitude is governed by the Fresnel-Kirchhoff integral[11] over a plane  $\Sigma_0$ ,

$$f(r) = \frac{i}{\lambda} \int_{\Sigma_0} \frac{e^{-ik|\mathbf{r}-\mathbf{r}'|}}{|\mathbf{r}-\mathbf{r}'|} d\sigma, \quad (1)$$

where  $\mathbf{r}$  is the coordinate in the image plane,  $\mathbf{r}'$  is the coordinate on the object plane,  $k$  is the wave number of the radiation, and  $d\sigma$  is an area element in the plane. For a point source or radiation located on the source plane at  $\mathbf{r}''$ , the electric field in the object plane is of the form  $e^{-ik|\mathbf{r}''-\mathbf{r}'|}/|\mathbf{r}''-\mathbf{r}'|$ . If  $D$  is the distance between planes, both  $|\mathbf{r}-\mathbf{r}'|$  and  $|\mathbf{r}''-\mathbf{r}'|$  are of the form  $|\mathbf{r}_a-\mathbf{r}_b| = \sqrt{D^2 + (x_a - x_b)^2 + (y_a - y_b)^2}$ , which can be expanded to first order in Cartesian coordinates to give the usual Fresnel approximation[8] to Eq. 1. Consider an object with a

transmission function  $q$ . When  $f$  is then expressed in cylindrical coordinates defined as

$$\xi = \rho \cos \theta \quad X = R \cos \Phi \quad x = r \cos \varphi$$

$$\eta = \rho \sin \theta \quad Y = R \sin \Phi \quad y = r \sin \varphi,$$

the electric field becomes

$$f(r) = \frac{i}{\lambda R_1 R_2} e^{-ik(R_1+R_2)} \int_0^\infty \int_0^{2\pi} e^{-\frac{ik}{2R_1}[\rho^2+R^2-2\rho R \cos(\theta-\Phi)] - \frac{ik}{2R_2}[r^2+R^2-2rR \cos(\varphi-\Phi)]} q(R) R dR d\Phi, \quad (2)$$

where  $q(R)$  is the transmission function for an object whose phase and absorption are a function of the coordinate  $R$  alone. The transmission function, which describes the phase deviation  $\phi$  and the (intensity) absorption  $\mu$  on traversal through the object, can be taken to be of the form

$$q(R) = \begin{cases} e^{i\phi(R)-\mu(R)/2} & \text{for } R \leq R_0 \\ 1 & \text{for } R > R_0, \end{cases} \quad (3)$$

where  $R_0$  is the radius of the object. Owing to the symmetry of both the object and source, the integrand in Eq. 2 must be independent of  $\varphi$  and can be evaluated at  $\varphi = 0$ .

The integral over  $R$  in equation 2 can be written as a sum of two integrals of the form

$$f(r) = \int_0^\infty E(R, \Phi) R dR d\Phi + \int_0^{R_0} E(R, \Phi) [q(R) - 1] R dR d\Phi,$$

where the exponential function in the integrand of Eq. 2 is denoted as  $E$ ; hence,  $f$  becomes the sum of two integrals  $\alpha$  and  $\beta$  multiplied by a common factor,

$$\begin{aligned} f(r) = & \frac{i}{\lambda R_1 R_2} e^{-ik(R_1+R_2)} e^{-\frac{ik}{2R_1}\rho^2 - \frac{ik}{2R_2}r^2} \underbrace{\left\{ \int_0^\infty R dR \int_0^{2\pi} e^{-\frac{ik}{2}\left(\frac{1}{R_1} + \frac{1}{R_2}\right)R^2 + \frac{ik}{R_1}\rho R \cos(\theta-\Phi) + \frac{ik}{R_2}r R \cos \Phi} d\Phi \right\}}_{\alpha} \\ & + \underbrace{\int_0^{R_0} R dR \int_0^{2\pi} [q(R) - 1] e^{-\frac{ik}{2}\left(\frac{1}{R_1} + \frac{1}{R_2}\right)R^2 + \frac{ik}{R_1}\rho R \cos(\theta-\Phi) + \frac{ik}{R_2}r R \cos \Phi} d\Phi}_{\beta}. \end{aligned}$$

The term denoted  $\alpha$  can be evaluated by noting that it is independent of  $\Phi$ , permitting  $\Phi$  to be taken as zero, completing the square in the argument of the exponential, and using the relation[12]

$$\int_0^{2\pi} e^{ia \sin(\zeta+\lambda)} d\zeta = 2\pi J_0(a),$$

which can also be shown to be independent of  $\zeta$ , together with [13]

$$\int_0^\infty J_0(\beta x) e^{\pm i a x^2} x dx = \pm \frac{i}{2a} e^{\mp i \frac{\beta^2}{4a}}$$

to give

$$\alpha = -\frac{2\pi i R_1 R_2}{k(R_1 + R_2)} e^{\frac{ik R_1 R_2}{2(R_1 + R_2)} (\frac{\rho^2}{R_1^2} + \frac{r^2}{R_2^2} + \frac{2\rho r}{R_1 R_2} \cos \theta)}$$

The second term denoted  $\beta$  can be reduced to

$$\beta = 2\pi \int_0^{R_0} [q(R) - 1] e^{-\frac{ik}{2} (\frac{1}{R_1} + \frac{1}{R_2}) R^2} J_0(kR\tilde{r}) R dR$$

where the dimensionless quantity  $\tilde{r}$  is defined as

$$\tilde{r} = \sqrt{\frac{\rho^2}{R_1^2} + \frac{r^2}{R_2^2} + \frac{2\rho r}{R_1 R_2} \cos \theta}.$$

## II. IMAGE INTENSITY FOR A GAUSSIAN SOURCE

The intensity at the image plane for an incoherent source with a source intensity distribution  $s(\rho)$  at the source plane is

$$I(r) = \int_0^\infty \int_0^{2\pi} s(\rho) |f(r)|^2 \rho d\rho d\theta.$$

For a Gaussian source with an intensity in the source plane described by

$$s(\rho) = \frac{1}{2\pi\sigma^2} e^{-\frac{\rho^2}{2\sigma^2}},$$

where  $\sigma$  is the length parameter for the source,  $I(r)$  becomes

$$I(r, \sigma) = \frac{1}{2\pi\sigma^2} \left[ \frac{1}{(R_1 + R_2)} \right]^2 \int_0^\infty \int_0^{2\pi} \rho e^{-\rho^2/2\sigma^2} \left| \hat{\alpha} + \hat{\beta} \right|^2 d\rho d\theta, \quad (4)$$

where the dimensionless quantities  $\hat{\alpha}$  and  $\hat{\beta}$  are defined as

$$\hat{\alpha} = e^{\frac{ik R_1 R_2}{2(R_1 + R_2)} (\frac{\rho^2}{R_1^2} + \frac{r^2}{R_2^2} + \frac{2\rho r}{R_1 R_2} \cos \theta)}$$

and

$$\hat{\beta} = \frac{ik(R_1 + R_2)}{R_1 R_2} \int_0^{R_0} [q(R) - 1] e^{-\frac{ik}{2}(\frac{1}{R_1} + \frac{1}{R_2})R^2} J_0(kR\tilde{r}) R dR.$$

Equation 4 can be written as the sum of three terms,

$$I(r, \sigma) = \frac{1}{2\pi\sigma^2} \left[ \frac{1}{(R_1 + R_2)} \right]^2 [I_{\alpha\alpha^*} + 2 \operatorname{Re} I_{\alpha\beta^*} + I_{\beta\beta^*}], \quad (5)$$

where

$$\begin{aligned} I_{\alpha\alpha^*} &= \int_0^\infty \int_0^{2\pi} \rho e^{-\rho^2/2\sigma^2} d\rho d\theta = 2\pi\sigma^2, \\ I_{\alpha\beta^*} &= \frac{-ik(R_1 + R_2)}{R_1 R_2} \int_0^\infty \int_0^{2\pi} e^{-\rho^2/2\sigma^2} e^{\frac{ikR_1 R_2}{2(R_1 + R_2)}(\frac{\rho^2}{R_1^2} + \frac{r^2}{R_2^2} + \frac{2\rho r}{R_1 R_2} \cos \theta)} \rho d\rho d\theta \\ &\quad \times \int_0^{R_0} R [q(R) - 1]^* e^{\frac{ik}{2}(\frac{1}{R_1} + \frac{1}{R_2})R^2} J_0(kR\tilde{r}) dR, \end{aligned}$$

and

$$\begin{aligned} I_{\beta\beta^*} &= \left[ \frac{k(R_1 + R_2)}{R_1 R_2} \right]^2 \int_0^\infty \int_0^{2\pi} d\rho d\theta \rho e^{-\rho^2/2\sigma^2} \times \\ &\quad \int_0^{R_0} [q(R) - 1] e^{-\frac{ik}{2}(\frac{1}{R_1} + \frac{1}{R_2})R^2} J_0(kR\tilde{r}) R dR \int_0^{R_0} [q(R') - 1]^* e^{\frac{ik}{2}(\frac{1}{R_1} + \frac{1}{R_2})R'^2} J_0(kR'\tilde{r}) R' dR'. \end{aligned}$$

From the theory of Bessel functions[14]  $J_0(kR\tilde{r})$  can be expanded as[15]

$$J_0(kR\tilde{r}) = \sum_m \varepsilon_m J_m(-kR\frac{\rho}{R_1}) J_m(kR\frac{r}{R_2}) \cos m\theta, \quad (6)$$

where  $\varepsilon_m$  is defined as  $\varepsilon_m = 2$  for  $m > 0$ , and  $\varepsilon_m = 1$  for  $m = 0$ . Through use of Eq. 6 and the orthogonality property of the cosine functions,

$$\int_0^{2\pi} \cos m\theta \cos n\theta d\theta = \begin{cases} 2\pi & \text{if } m = n = 0 \\ \pi\delta_{m,n} & \text{otherwise} \end{cases},$$

Eq. 5 becomes

$$\begin{aligned} I_{\alpha\beta^*} &= \frac{(-i)^{m+1} 2\pi k(R_1 + R_2)\sigma^2}{\gamma R_1 R_2} e^{\frac{ikR_1 R_2}{2(R_1 + R_2)}\frac{r^2}{R_2^2}} \sum \varepsilon_m \int_0^{R_0} dR R [q(R) - 1]^* e^{\frac{ik}{2}(\frac{1}{R_1} + \frac{1}{R_2})R^2} \\ &\quad \times J_m(\frac{kr}{R_2} R) I_m \left( \frac{\sigma^2 k^2 r R}{\gamma R_1 (R_1 + R_2)} \right) e^{-\frac{k^2 \sigma^2}{2\gamma} \left[ \frac{r^2}{(R_1 + R_2)^2} + \frac{R^2}{R_1^2} \right]}, \end{aligned}$$

where  $I_m$  is a modified Bessel function and

$$I_{\beta\beta^*} = \left[ \frac{k(R_1 + R_2)}{R_1 R_2} \right]^2 \pi \sigma^2 \sum g_m \varepsilon_m^2 \int_0^{R_0} dR R [q(R) - 1] e^{-\frac{ik}{2}(\frac{1}{R_1} + \frac{1}{R_2})R^2} J_m(kR \frac{r}{R_2}) \times \\ \int_0^{R_0} dR' R' [q(R') - 1]^* e^{\frac{ik}{2}(\frac{1}{R_1} + \frac{1}{R_2})R'^2} J_m(kR' \frac{r}{R_2}) I_m \left( \frac{k^2 \sigma^2 R R'}{R_1^2} \right) e^{-\frac{k^2 \sigma^2 (R^2 + R'^2)}{2R_1^2}}$$

where

$$g_m = \begin{cases} 2 & \text{if } m = 0 \\ 1 & \text{if } m > 0 \end{cases}.$$

and the parameter  $\gamma$  is given by

$$\gamma = 1 - i \frac{k(R_2/R_1)\sigma^2}{2(R_1 + R_2)}.$$

Through straightforward algebraic manipulation, it is possible to write  $I(r, \sigma)$  as a sum over dimensionless quantities as

$$I(r, \sigma) = \left( \frac{1}{R_1 + R_2} \right)^2 \left[ 1 + 2 \operatorname{Re} \sum_{m=0}^{\infty} (-i)^{m+1} \varepsilon_m \hat{I}_{\alpha\beta^*}^{(m)}(r) + \sum_{m=0}^{\infty} g_m \varepsilon_m^2 \hat{I}_{\beta\beta^*}^{(m)}(r) \right] \quad (7)$$

where

$$\hat{I}_{\alpha\beta^*}^{(m)}(r) = \frac{k(R_1 + R_2)}{\gamma R_1 R_2} e^{\frac{ikR_1 R_2}{2(R_1 + R_2)} \frac{r^2}{R_2^2}} \int_0^{R_0} [q(R) - 1]^* e^{\frac{ik}{2}(\frac{1}{R_1} + \frac{1}{R_2})R^2} \\ \times J_m\left(\frac{kr}{R_2} R\right) I_m \left( \frac{\sigma^2 k^2 r R}{\gamma R_1 (R_1 + R_2)} \right) e^{-\frac{k^2 \sigma^2}{2\gamma} \left[ \frac{r^2}{(R_1 + R_2)^2} + \frac{R^2}{R_1^2} \right]} R dR \\ \hat{I}_{\beta\beta^*}^{(m)}(r) = \frac{1}{2} \left[ \frac{k(R_1 + R_2)}{R_1 R_2} \right]^2 \int_0^{R_0} [q(R) - 1] e^{-\frac{ik}{2}(\frac{1}{R_1} + \frac{1}{R_2})R^2} J_m(kR \frac{r}{R_2}) R dR \\ \times \int_0^{R_0} [q(R') - 1]^* e^{\frac{ik}{2}(\frac{1}{R_1} + \frac{1}{R_2})R'^2} J_m(kR' \frac{r}{R_2}) I_m \left( \frac{k^2 \sigma^2 R R'}{R_1^2} \right) e^{-\frac{k^2 \sigma^2 (R^2 + R'^2)}{2R_1^2}} R' dR'.$$

### III. IMAGE INTENSITY FOR POINT AND PARALLEL BEAM SOURCES

In the limit where the source can be approximated as a point source, *i.e.* where  $\sigma = 0$ , the arguments of  $I_m$  become zero so that,  $I_m = \delta_{m,0}$  and the sums in Eq. 7 reduce to a single term.

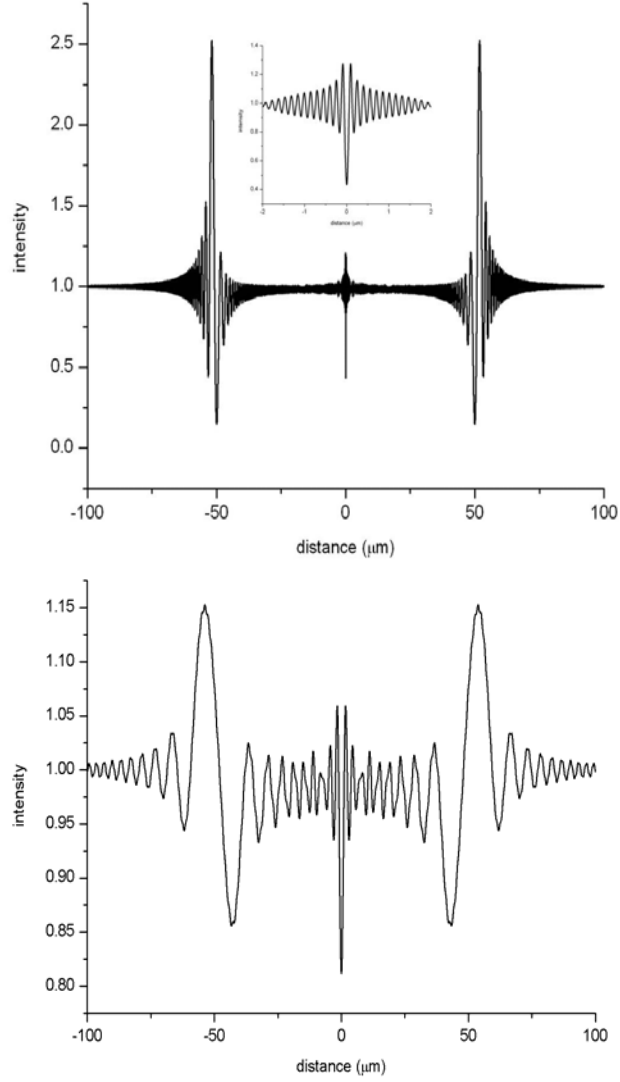


FIG. 2: Intensity versus radial coordinate calculated from Eq. 8 for a  $100\mu\text{m}$  diameter polystyrene sphere, with  $\delta = 10^{-6}$  and  $\mu_0 = 0$ , irradiated by a point source of x-radiation. The x-ray photon energy is (top)  $30\text{ keV}$  and (bottom)  $1.7\text{ keV}$ , corresponding to wavelengths of  $24$  and  $730\text{ pm}$ , respectively. Inset: expanded view of the center of the  $30\text{ keV}$  plot.

The parameter  $\gamma$  also becomes unity; thus the intensity reduces to the relatively simple expression

$$I(r, 0) = \left( \frac{1}{R_1 + R_2} \right)^2 \left| 1 + \frac{ik(R_1 + R_2)}{R_1 R_2} e^{-\frac{ik(R_1/R_2)}{2(R_1 + R_2)} r^2} \right|^2 \quad (8)$$

$$\int_0^{R_0} [q(R) - 1] e^{-\frac{ik}{2} \left( \frac{R_1 + R_2}{R_1 R_2} \right) R^2} J_0(kr \frac{R}{R_2}) R dR \Big|^2. \quad (9)$$

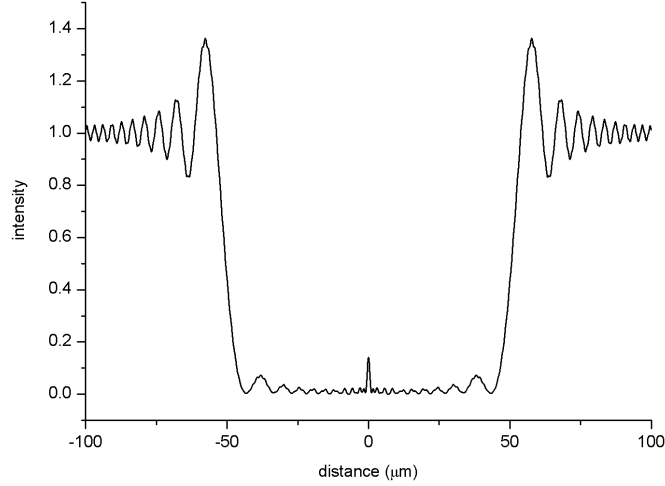


FIG. 3: Intensity in arbitrary units versus radial coordinate calculated from Eq. 8 for a  $100\text{ }\mu\text{m}$  diameter gold sphere, with  $\delta = 3.56 \times 10^{-6}$  and  $\mu_0 = 2.5 \times 10^4\text{ m}^{-1}$ , irradiated by a point source of x-radiation. The x-ray photon energy is  $1.7\text{ keV}$ .

If the source-to-object distance becomes large compared with the object-to-image distance, *i.e.* if  $R_1 \gg R_2$ , Eq. 7 reduces to

$$I(r, 0) = \frac{1}{R_1^2} \left| 1 + \frac{ik}{R_2} e^{-\frac{ik}{2R_2} r^2} \int_0^{R_0} [q(R) - 1] e^{-\frac{ik}{2R_2} R^2} J_0\left(kr \frac{R}{R_2}\right) R dR \right|^2. \quad (10)$$

which could be derived directly from Eq. 2. It is noteworthy that both Eqs. 8 and 10 are integrals over one coordinate and require no summation.

#### IV. EXPERIMENTS AND CALCULATED IMAGES

Plots for the expressions derived above were made by computing intensity versus radius and shown with the radial coordinate extending in two directions to give a simulation of the intensity profile over a center slice of an image. Fig. 2 shows the results of calculations for polystyrene spheres irradiated by a point source of x-radiation for two different x-ray photon energies,  $1.7\text{ keV}$  and  $30\text{ keV}$ . The the source-to-object and object-to-image planes used in all of the calculations



were  $R_1 = 0.2\text{ m}$  and  $R_2 = 2.4\text{ m}$  giving a magnification of 13. The oscillatory features at the

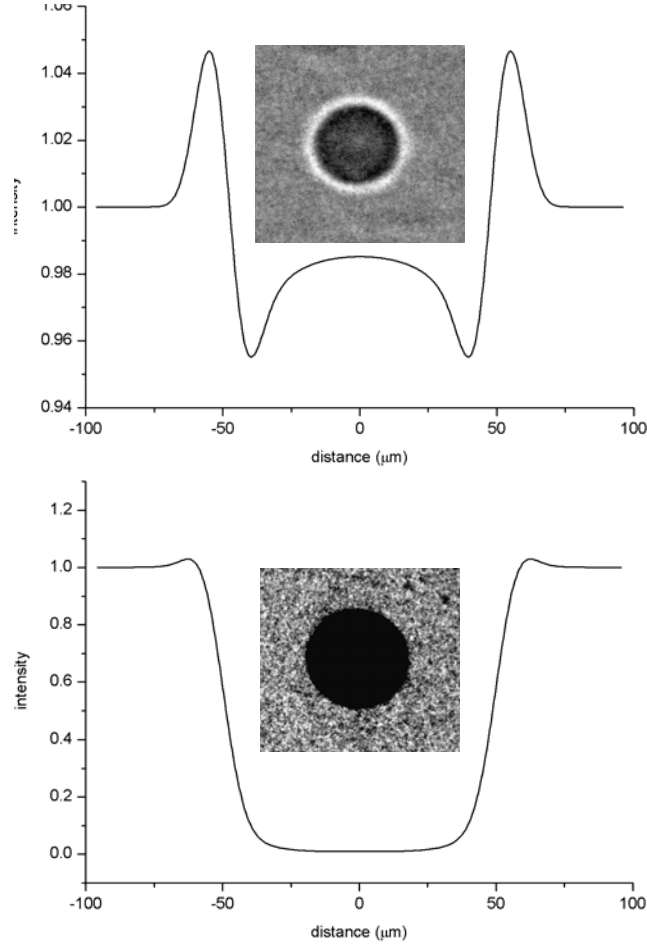


FIG. 4: Intensity versus radial coordinate calculated from Eq. 7 for (top plot) a  $100\text{ }\mu\text{m}$  diameter sphere, with  $\delta = 1 \times 10^{-6}$  and  $\mu_0 = 0$ , and (bottom plot) a  $100\text{ }\mu\text{m}$  diameter gold sphere with  $\delta = 3.56 \times 10^{-6}$  and  $\mu_0 = 2.5 \times 10^4\text{ m}^{-1}$  irradiated by an x-ray source with the source diameter parameter  $\sigma = 6.75\text{ }\mu\text{m}$  and an x-ray photon energy of  $1.7\text{ keV}$ . The insets are images of (top) a  $100\text{ }\mu\text{m}$  diameter polystyrene sphere; and (bottom) a  $220\text{ }\mu\text{m}$  diameter gold sphere. Both images were taken with the x-ray tube operating for 3 min at 90 kV and  $100\text{ }\mu\text{A}$ . The intensity patterns determined from theory were calculated with Mathematica using a large number of significant figures.

perimeters of the spheres are seen to be of lower frequency and of smaller amplitude in the plot calculated with the lower energy x-radiation. Oscillatory features at the centers of the images are present in the plots at both x-ray energies, albeit with a significantly smaller amplitude at  $30\text{ keV}$ .

A similar plot for a  $100\ \mu\text{m}$  diameter gold sphere calculated for a point source are shown in Fig. 3. Strong absorption contrast is seen in central region of the plot. Despite the strong absorption of gold at a photon energy of  $1.7\ \text{keV}$ , oscillations in the intensity near  $r = 0$  arising from interferences are still found.

Calculations for images of nylon and gold spheres for a nonvanishing x-radiation source are shown in Fig. 4. The phase contrast features are virtually all absent in the plot for the gold sphere, but remain as easily visible features for the nylon sphere.

Experiments were carried out using a microfocus x-ray tube (Oxford, Inc. Model UM-M1) with an anode source diameter, as specified by the manufacturer, of  $13.5\ \mu\text{m}$  together with a Peltier effect cooled CCD camera (Princeton Instruments, Model PI-SCX), equipped with a fiber optic bundle that views a phosphor plate to give an input-to-output image size ratio of unity. Further details of the experimental apparatus can be found in Ref. [8].

In order to determine the capability of the microfocus x-ray apparatus for imaging small spherical objects, experiments were carried out with polystyrene spheres of various diameters (purchased from Duke Scientific Co.) As shown in Fig. 5, experiments with several different diameter polystyrene and gold spheres indicate that the visualization of polystyrene spheres larger than  $20\ \mu\text{m}$  is facile owing to the distinctive dark and light outlines of the spheres provided by phase contrast; distinguishing polystyrene objects with features smaller than  $10\ \mu\text{m}$  from the background however is difficult. The nearly spherical gold particles were made by scattering 325 mesh gold powder on a glass cover slide and heating the glass with a torch until fusion of the metal was observed. This procedure produced approximately spherical particles with a random distribution of diameters. Although there is virtually no phase contrast seen in Fig. 5 for the gold spheres, the absorption contrast of gold is sufficiently large that particles larger than  $10\ \mu\text{m}$  could be seen easily against the background.

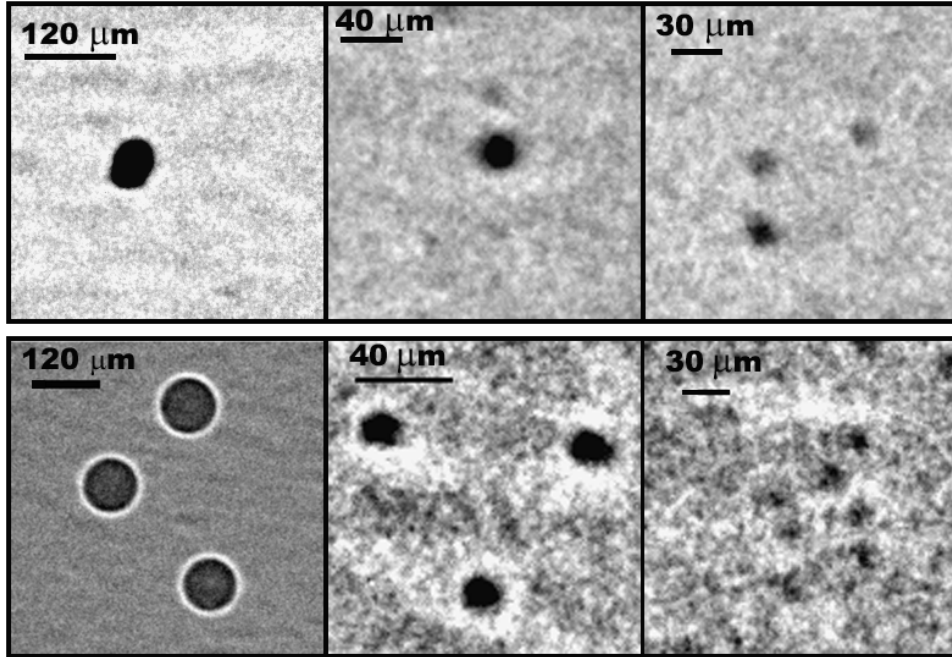


FIG. 5: X-ray images of (top) gold particles and (bottom) polystyrene spheres. The polystyrene spheres are nominally  $100\text{ }\mu\text{m}$ ,  $20\text{ }\mu\text{m}$ , and  $10\text{ }\mu\text{m}$  in diameter. The exposure time was 15 min with the x-ray tube operating at 90 kV and  $100\text{ }\mu\text{A}$

## V. DISCUSSION

A feature of the point source calculations given here that appears to be unique to objects with cylindrical symmetry is the appearance of intensity variations amounting to what would be a "bright spot" at image plane on the symmetry axis of the object, as shown in Figs. 2 and 3. The observation of a bright spot radiation as a result of interposing an opaque circular disk between a visible light source and the image plane dates back almost two centuries to the time when Fresnel submitted his theory of imaging[9] to the French Academy; although the effect is counterintuitive, it is easily demonstrated in the laboratory with visible light, and is a feature that is present over a range of wavelengths. As is shown here, the total number of photons in the central region diminishes greatly as the wavelength of the radiation is made short, so that for

radiation corresponding to an energy of 30 keV, there is little evidence of a bright spot.

The use of nanometer sized particles tagged with site directed antibodies to target specific tissues has become common practice in imaging and drug delivery, and even holds promise for therapy. The high sensitivity of x-ray phase contrast imaging for detecting small objects may have similar application for locating particles such as polystyrene or gold in soft tissue. Although heavy metal objects such as gold particles do not produce phase contrast to the same degree that objects with smaller values of  $\delta$  do under the conditions used in the experiments reported here, the high resolution of the method permits visualization of spheres with diameters on the order of  $20\text{ }\mu\text{m}$ . The results of this study show that for the  $20\text{ }\mu\text{m}$  x-ray source size, polystyrene and gold spheres with diameters on the order the source size can be distinguished reliably from the background. Although a rigorous study has not been carried out, the present results suggest that x-ray sources with smaller source sizes should be capable of distinguishing even smaller particles from a low density background.

## VI. ACKNOWLEDGEMENTS

The authors, GJD, TJH, and GC; and GJD and CRP are grateful for the support of this research by the US Army Medical Research and Materiel Command under grants DAMD17-02-1-0307 and W81XWH-04-1-0481, respectively. CRP acknowledges partial support from the U.S. Department of Energy under Grant DE-FG02-03ER15413. CML was supported by NIH grant T32 DK60415. Opinions, interpretations, conclusions and recommendations are those of the authors and are not necessarily endorsed by the US Army.

- 
- [1] P. Cloetens, R. Barrett, J. Baruchel, J.-P. Guigay, M. Schlenker, *J. Phys. D* **29**, 133 (1996).
  - [2] S. W. Wilkins, T. Gureyev, D. Gao, A. Pogany, A. W. Stevenson, *Nature* **384**, 335 (1996).

- [3] F. Arfelli, *et al.*, *Phys. Med. Biol.* **43**, 2845 (1998).
- [4] P. Cloetens, *et al.*, *Appl. Phys. Lett.* **75**, 2912 (1999).
- [5] S. Zabler, P. Cloetens, J. P. Guigay, J. Baruchel, *Rev. Sci. Instrum* **76**, 073705 (2005).
- [6] C. J. Bailat, T. J. Hamilton, C. Rose-Petruck, G. J. Diebold, *Appl. Phys. Lett.* **85**, 4517 (2004).
- [7] T. J. Hamilton, C. J. Bailat, C. Rose-Petruck, G. J. Diebold, *Phys. med. Biol.* **49**, 4985 (2004).
- [8] G. Cao, T. J. Hamilton, C. Rose-Petruck, G. J. Diebold, *J. Opt. Soc. Am. A* **24**, 1201 (2007).
- [9] M. Born, E. Wolf, *Principles of Optics* (Pergamon, Oxford, 1980).
- [10] J. M. Cowley, *Diffraction Physics* (North-Holland, Amsterdam, 1984).
- [11] M. V. Klein, *Optics* (John Wiley & Sons, Inc., 1970).
- [12] I. S. Gradshteyn, I. M. Ryzhik, *Table of integrals, Series, and Products* (Academic Press, 1965), fourth edn.
- [13] The first of these can be shown to be independent of  $\lambda$ , and to yield the zero'th order Bessel function.  
The second is a combination of two integrals found on p 758 of Ref. [12].
- [14] G. N. Watson, *A Treatise On The Theory of Bessel Functions* (Cambridge University Press, 1996), second edn.
- [15] The identity in the text follows from Neumann's Addition Theorem, Ref.[14] Chapter XI.